Tunable polymer/liquid crystal composite devices

Liu, Yanjun

2007

Liu, Y. (2007). Tunable polymer/liquid crystal composite devices. Doctoral thesis, Nanyang Technological University, Singapore.

https://hdl.handle.net/10356/4752

https://doi.org/10.32657/10356/4752

Nanyang Technological University

Tunable Polymer/Liquid Crystal Composite Devices

Liu Yanjun

School of Electrical & Electronic Engineering

A thesis submitted to the Nanyang Technological University
in fulfillment of the requirement for the degree of
Doctor of Philosophy

2007

Acknowledgements

I would like to take this opportunity to express my sincere gratitude to my supervisor Prof. Sun Xiaowei for his guidance and advices during my PhD training. From the very beginning, he took an active interest in my research and his constant support and encouragement made me enjoyable in my research.

I am also grateful to Prof. Ji Wei in National University of Singapore for allowing me to use the Nd:YAG laser system and the help from Dr. H. I. Elim, Dr. Li Heping, and Mr. Mi Jun with the lasing measurement. My discussions with them were much appreciated.

I would also like to thank Dr. Zhang Xinhai and Miss Yong Anna Marie in Institute of Materials Research and Engineering; Dr. Yin Xijiang and Mr. Goh Kwee Hwang in Nanomaterials and Nanofabrication Lab, Singapore Polytechnic, for their help in carrying out some of the experiments and tests.

I would also like to extend my gratitude to all the staffs and students at Nanoelectronics I, Network Technology Research Center, Nanoscience and Nanotechnology Cluster in Nanyang Technological University (NTU), especially Prof. Yu Siu-Fung, Prof. Sun Changqing, Prof. Shum Ping, Dr. Xu Chunxiang, Dr. Yu Guoqing, Dr. Chen Baijun, Dr. Zhao Zhiwei, Dr. Li Junfeng, Dr. Ji Xiaohong, Dr. Pan Likun, Dr. Wang Jianxiong, Dr. Yan Xingbin, Mr. Tan Swee Tiam, Mr. Wang Qin, Ms. Sze Jia Yin, Ms. Leong Sok Ping Eunice, Ms. Yang Yi, Mr. Yoga Divayana, and Mr. Alagappan Gandhi, for their encouragement, inspirational discussions, and all kinds of assistance they offered. My friends, Mr. Ding Liang, Mr. Sun Yuyang, and Mr. Wu Qiuwei, are also thanked.

Some Professors and friends outside of Singapore are also much appreciated for their help and encouragement. They are Prof. Xu Keshu, Prof. Liu Jianhua, and Dr. Dai Haitao in Fudan University, China, Prof. Zhang Bin in Beijing Jiaotong University, China, Mr. Xie Hang in Hong Kong University of Science and Technology, Hong Kong, Mr. Ling Tao in University of Michigan, USA, and Ms. Liu Wenjuan in Pennsylvania State University, USA.

Finally, special thanks are given to my parents and sisters for their forever and unconditional support.

Abstract

As a unique class of materials, polymer-dispersed liquid crystals (PDLCs) have been studied for twenty years. PDLCs hold promise for many applications ranging from switchable windows to displays. In 1993, Sutherland *et al.* fabricated a PDLC grating by holography. The holographic PDLC (H-PDLC) opens a new stage for PDLC applications in optical communications, information storage, and integrated optics. By now these materials, which are simply a combination of polymers and liquid crystals, have become the focus of extensive research in many fields.

This thesis focused on developing new electro-optical devices based on PDLC or H-PDLC. In particular, we firstly optimized the fabrication conditions for H-PDLC Bragg gratings. Using holography, one-dimensional (1D) H-PDLC Bragg grating was fabricated. The 1D H-PDLC grating itself is a 2×2 optical switch. With optimization of the fabrication parameters, we obtained a polarization insensitive H-PDLC optical switch with high contrast ratio (23.4 dB), high signal-noise ratio (15.1 dB), and fast response time (200 μs).

We have also fabricated several new devices using the photopolymerization induced phase separation (PIPS) method. Using a glass fly's-eye lens as a photomask, a PDLC fly's-eye lens was fabricated. The major advantages of such fly's-eye lens are easy fabrication process, compactness, light weight, and low cost. It is a flat device, indicating a simpler fabrication process than the polymer fly's-eye lens. Moreover, PDLC fly's-eye lens is electrically tunable. PDLC has also potential applications in high capacity storage. A specially designed computer-generated hologram (CGH) was recorded in PDLC. Such kind of phase type CGH showed a good reconstructed image. It is a write-once-read-many mode memory device and electrically switchable.

On the other hand, 1D H-PDLC grating can also be considered as a 1D photonic crystal (PhC). The 1D photonic bandgap structures (either transmission or reflection gratings) fabricated from H-PDLC materials could have the optical properties modified (switched) electrically, thermally, or optically. This system provided significant tunability and the choice of the constituent materials was essential for the application of interest. At the edge of the bandgap of PhC, the photon group velocity approaches zero. If a gain material is present, the large increase in optical path length would enhance the effective gain. In this thesis, we demonstrated an optically pumped and thermally switched distributed-feedback (DFB) laser from a dye-doped H-PDLC transmission grating structure. Two different dyes were investigated to obtain the lasing. We also found that the LC concentration played an important role in obtaining the lasing and selecting the lasing wavelength. By varying LC concentrations, different lasing wavelengths from 580 nm to 630 nm were achieved.

Besides 1D PhCs, 2D and 3D H-PDLC PhCs were also fabricated using different methods. Using a single diffractive element, which is comprised of three diffraction gratings at 120° relative to one another, we obtained 2D PhCs, resulting from 3-beam interference pattern. However, it is difficult to get high resolution (1 or 2 μm) gratings with a large area for the photomask. Presently, we can only get the mask with grating period of 4 μm, which determines the relatively large lattice constant of the H-PDLC PhCs and limits their applications. To obtain smaller lattice constant and simplify the optical setup, specially designed prisms were used to achieve multi-beam interference. Using the specially designed prism, 3D H-PDLC PhCs were successfully fabricated with the lattice constant of about 420 nm. These methods improve the

alignment and stability of the optical setup, making it more robust than the multiple beam setups implemented previously.

Finally this thesis recommends some future works in the optimization of these structures and applications that can be pursued using these structures.

Table of Contents

List of Figures

List of Tables

CHAPTER 1   Introduction

1.1   Motivation

Polymer-dispersed liquid crystals (PDLCs) are a relatively new class of materials that hold promise for many applications ranging from switchable windows to projection displays. These materials, which are simply a combined application of polymers and liquid crystals, are extensively investigated in the display industry.

PDLCs consist of liquid crystal droplets which are dispersed in a solid polymer matrix. The resulting material is a sort of "swiss cheese" polymer with liquid crystal droplets filling in the holes. These tiny droplets (2 - 5 μm for practical applications) are responsible for the unique behavior of the material. By changing the orientation of the liquid crystal molecules with an electric field, it is possible to vary the intensity of transmitted light.

On the other hand, holography has been widely applied in photonics. Based on diffraction, the hologram can affect either the spatial or spectral nature, or both, of a light beam. This can be used to accomplish many useful tasks in many applications.

The marriage of PDLC and holography gives birth to new developments of the material and leads to applications in many fields, especially in optical communications, information storages and flat panel displays. Holographic PDLC (H-PDLC) devices show true Bragg operation, high diffraction efficiency, fast response time, easy fabrication process. Another unique advantage of H-PDLC is that it is electrically controllable. For example, the light diffraction direction of H-PDLC Bragg gratings can be switched from the first order diffraction to the zeroth order diffraction by applying an electric field. Moreover, H-PDLC has a very fast response speed, which makes it promising in many fields, such as optical communications, flat

panel displays, and information storage. Based on these unique properties, a lot of H-PDLC devices can be designed and realized.

1.2 Objectives

This thesis focuses on designing new PDLC/H-PDLC devices and their fabrication based on the photopolymerization induced phase separation (PIPS) method. The diffraction properties, electro-optical characteristics, and response time will be studied in detail with different parameters, such as the exposure intensity and time, the ratio of the constituent materials, and temperature control.

Our first goal is to set up the laser exposure system, electro-optical performance measurement system, and response time measurement system. By measuring the performance of the devices, we experimentally optimize the ratio of the materials and find the optimum fabrication conditions. Based on the optimized material recipe, new PDLC/H-PDLC devices were proposed and fabricated.

Our second goal is to achieve lasing emission from dye-doped PDLC/H-PDLC. Similar to the random lasing obtained from the nanoparticles randomly distributed in a background material, the random distribution of the liquid crystal droplets in PDLC leads to the random lasing as well. On the other hand, with a distributed feedback structure in H-PDLC, where the liquid crystal lamellae and polymer lamellae are periodically distributed, single-mode lasing emission is accordingly anticipated.

Our third goal is to fabricate 2D and 3D H-PDLC photonic crystals and investigate their optical properties. We try to use an easy method to fabricate H-PDLC photonic crystals and accordingly their photonic bandgaps can be easily engineered.

1.3   Major Contributions

1. The formation of the materials was optimized experimentally using the theoretical analysis as a guide. Especially, the effect of the surfactant on the electro-optical properties of H-PDLC was investigated in detail.

2. Based on the H-PDLC Bragg grating with optimization of the fabrication parameters, we obtained a polarization insensitive 2×2 H-PDLC optical switch with high contrast ratio (23.4 dB), high signal-noise ratio (15.1 dB), and fast response time (200 μs).

3. Using a glass fly's-eye lens as a mask, a tunable PDLC fly's-eye lens was fabricated. The major advantages of such fly's-eye lens are easy fabrication process, compactness, light weight and low cost. It is a flat device, indicating a simpler fabrication process than the polymer fly's-eye lens. Moreover, PDLC fly's-eye lens is electrically tunable.

4. PDLC has been proven to have potential applications in information storage. In this thesis, the author firstly showed computer-generated hologram (CGH) recorded in PDLC. Such kind of phase type CGH showed a good reconstructed image. It is a write-once-read-many (WORM) mode memory device and electrically switchable. This method is another alternative and easy way to record the information in PDLC.

5. We further investigated the lasing properties from dye-doped H-PDLC. With conventional PDLC structure, a random lasing was obtained. With 1D transmission grating structure, we achieved a single-mode lasing. By now, our group has obtained the lasing emission with narrowest linewidth. We further investigated the effect of the liquid crystal concentrations on the lasing properties of the dye-doped H-PDLC and found that, to achieve a lasing emission with better

properties from H-PDLC transmission gratings, the LC concentration of around 20 wt% was the best trade-off between sufficient refractive index modulation and optical scattering in the samples.

6. 2D and 3D H-PDLC photonic crystals were successfully fabricated in our group using specially designed photomask and prisms, respectively. The use of the specially designed optical components greatly decreases the complexity of the optical setup and improves the alignment and stability of the optical setup, making it more robust than the multiple beam setups reported previously.

1.4 Organization

This thesis is composed of eight chapters. Chapter 1 describes the motivation, objectives, and major contributions of the research. The organization of the overall thesis is also presented in this chapter.

Chapter 2 introduces the foundamentals of liquid crystal and polymer. The basic phases of the liquid crystal, the general theories of elastic deformation, dielectric anisotropy, free energy, and so on, are described.

Chapter 3 gives a basic introduction of H-PDLC including the material recipe and fabrication. An overview of H-PDLC is presented. Sample characterizations in terms of structural, optical, and electro-optical properties are also described in this chapter.

In Chapter 4, the performance of H-PDLC is theoretically and experimentally optimized. We obtained the H-PDLC Bragg gratings with a high diffraction efficiency (>80%). The effect of surfactant on the electro-optical performance of H-PDLC was investigated in detail. With optimized fabrication conditions, a polarization insensitive 2×2 H-PDLC optical switch with high contrast ratio (23.4 dB), high signal-noise ratio (15.1 dB), and fast response time (200 μs) was achieved.

Chapter 5 reports two different patterned PDLC devices. One is a tunable PDLC fly's-eye lens fabricated using a glass fly's-eye lens as a mask. The other one is PDLC CGH fabricated with a specially designed CGH mask. Both of them are electrically tunable or switchable. The detailed fabrication and properties were described in this chapter.

Chapter 6 gives an investigation on the lasing from dye-doped PDLC and H-PDLC. A random lasing was achieved from dye-doped conventional PDLC structure, where LC droplets randomly distribute in the polymer matrix. In dye-doped H-PDLC transmission Bragg grating where polymer-rich and LC-rich lamellae are periodically arranged by holography, single-mode lasing was obtained. The effect of LC concentration on the lasing properties was investigated in detail.

Chapter 7 describes 2D and 3D photonic crystals (PhCs) based on H-PDLC. Using specially designed photomask and prisms, 2D and 3D H-PDLC PhCs were successfully achieved. The detailed optical properties of PhCs were also explored.

This thesis concludes in Chapter 8 with future work proposed.

CHAPTER 2   Liquid Crystal and Polymer Materials

2.1   Introduction to Liquid Crystal

The history of LC can be dated back to around 150 years ago when Virchow, Mettenheimer and Valentin noticed that a strange behavior occurred when a polarized light was used in observation of a liquid substance formed by a nerve fiber. This is actually the first observation of LC. But at that time the observation did not draw too much attention. Even later in 1877, it was still not realized that a new phase of substance was discovered when Otto Lehmann found that a substance changed from a clear state to a cloudy state when the temperature was decreased to the crystalline transition temperature. The study of LC started in 1888 when Friedrich Reinitzer, an Austrian botanist, performed an experiment where he observed that cholesteryl benzoate changed from a solid state to a cloudy liquid when the temperature was increased and eventually changed to a clear liquid as the temperature was further increased. He was the first person who suggested that this hazy liquid was a new phase of substance and thus he is credited with discovering the LC phase. With over 100 years' history, various LC materials have been studied and synthesized.

LCs have attracted a lot of attention due to the unique electro-optical and thermo-optical properties and have been used in numerous applications, such as liquid crystal displays (LCDs) for televisions, projectors, watches, cell phones, spatial light modulators (SLMs) for adaptive optics in real time optical imaging, optical switches and attenuators for telecommunications, and optical phase arrays (OPAs) for beam steering, etc. The research on LC materials and devices is of importance not only to the quality of our daily life but also to the development of the human society.

2.1.1 Liquid Crystal Phases

Generally speaking, there are three phases of thermotropic LCs, known as the nematic phase, smectic phase, and cholesteric phase. Figure 2.1(a) illustrates the nematic phase in which only long range orientational order of the molecular axes exists. Figure 2.1(b) shows the smectic phase in which one-dimensional translational order as well as orientational order exist. Figure 2.1(c) illustrates the cholesteric phase of a liquid crystal by viewing the distribution of molecules at several planes that are perpendicular to the helical axis. The cholesteric phase is actually a nematic type of liquid crystal except that it is composed of chiral molecules. As a consequence, the structure acquires a spontaneous twist about a helical axis normal to the director. The twist can be right-handed or left-handed depending on the molecular chirality.

(a) Nematic Phase   (b) Smectic Phase

(c) Cholesteric Phase
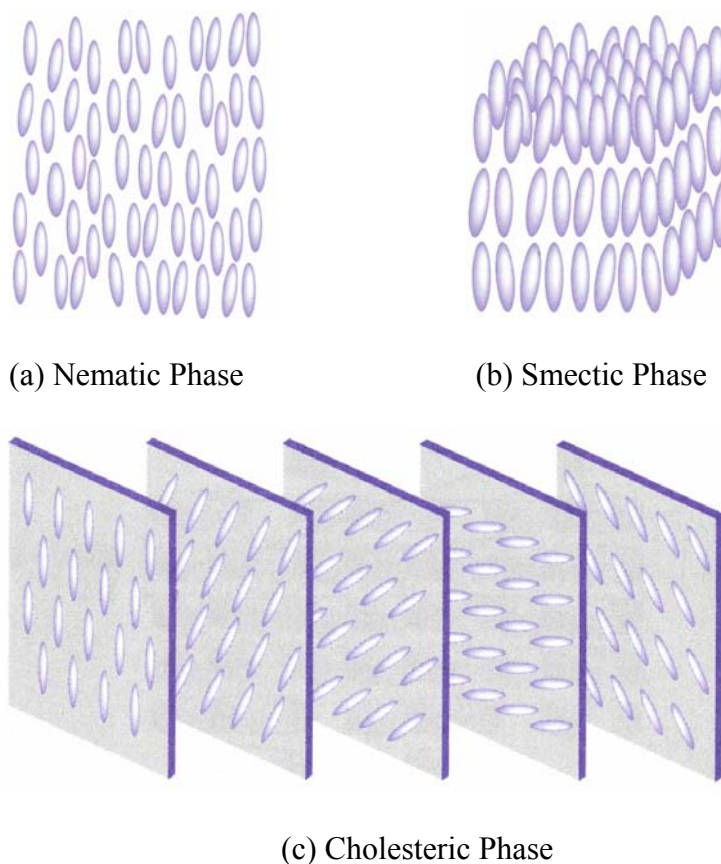
Figure 2.1 Phases of liquid crystals: (a) nematic phase; (b) smectic phase; and (c) cholesteric phase.

2.1.2 Liquid Crystal Order Parameter

In the nematic phase, the liquid crystal molecules are rodlike with their long axes aligned approximately parallel to one another. Thus at any point in the medium, we can define a unit vector, **n**, to represent the preferred orientation in the immediate neighborhood of the point. This vector is known as the director. In a homogeneous nematic LC, the director is constant throughout the medium. In an inhomogeneous nematic LC, the director can change from point to point and is a function of space (*x*, *y*, *z*) in general. If we define a unit vector to represent the long axis of each molecule, then the director, **n**, is the statistical average of the unit vectors over a small volume element around the point.

The order parameter, *S*, of a LC is defined as

$$S = \frac{1}{2}\left\langle 3\cos^2\theta - 1 \right\rangle, \qquad\qquad (2.1)$$

where θ is the angle between the long axis of an individual molecule and the director and the angular brackets denote a statistical average. For perfectly parallel alignment, *S* = 1, while for totally random orientation, *S* = 0. In the nematic phase, the order parameter, *S*, has an intermediate value that is strongly temperature dependent. It changes discontinuously to zero at the clearing point. Typical values of the order parameter *S* are in the range of 0.4 - 0.6.

2.1.3 Dielectric Anisotropy

Because of the orientational ordering of the rodlike molecules, the smectic and nematic liquid crystals are uniaxially symmetric, with the axis of symmetry parallel to the axes of the molecules (director **n**). As a result of the uniaxial symmetry, the dielectric constants differ in value along the preferred axis ($\varepsilon_\parallel$) and perpendicular to this axis ($\varepsilon_\perp$). The dielectric anisotropy is defined as

$$\Delta\varepsilon = \varepsilon_{\parallel} - \varepsilon_{\perp.} \qquad \qquad (2.2)$$

The sign and magnitude of the dielectric anisotropy $\Delta\varepsilon$ are of the utmost importance in the applicability of liquid crystal materials to realize various electro-optic effects.

2.1.4 Refractive Index

Under proper treatment, a slab of nematic LC can be obtained with a uniform alignment of the director. Such a sample exhibits uniaxial optical symmetry with two principal refractive indices n_o and n_e. The ordinary refractive index n_o is for light with electric field polarization perpendicular to the director and the extraordinary refractive index n_e is for light with electric field polarization parallel to the director. The birefringence (or optical anisotropy) is defined as

$$\Delta n = n_e - n_{o.} \qquad \qquad (2.3)$$

If $n_o < n_e$, LC is of positive birefringence, whereas if $n_o > n_e$, it is of negative birefringence. In classical dielectric theory, the macroscopic refractive index is related to the molecular polarizability at optical frequencies. The existence of the optical anisotropy is mainly due to the anisotropic molecular structures. In the optical regime, $\varepsilon_{\parallel} = \varepsilon_0 n_e^2$, and $\varepsilon_{\perp} = \varepsilon_0 n_o^2$, thus $\Delta\varepsilon = \varepsilon_0 (n_e^2 - n_o^2)$. For most LCs, the ordinary refractive index is around 1.5. The optical anisotropy plays an essential role in changing the polarization state of light in liquid crystals.

For light propagating in the liquid crystal with an incident angle θ relative to the optical axis, shown as Figure 2.2, two eigen refractive indices are seen by the light with two modes of propagation. One mode with its polarization direction perpendicular to the plane formed by the wave vector and the optic axis is called ordinary wave, which sees a refractive index of n_o (independent of the incident angle

9

θ). The other one with its polarization direction parallel to the plane formed by the wave vector and the optic axis is called extraordinary wave, which sees an effective refractive index (dependent of the incident angle θ). The effective refractive index seen by the light can be written as

$$n_{eff}(\theta) = \left[\frac{\cos^2 \theta}{n_o^2} + \frac{\sin^2 \theta}{n_e^2} \right]^{-\frac{1}{2}}.$$ (2.4)
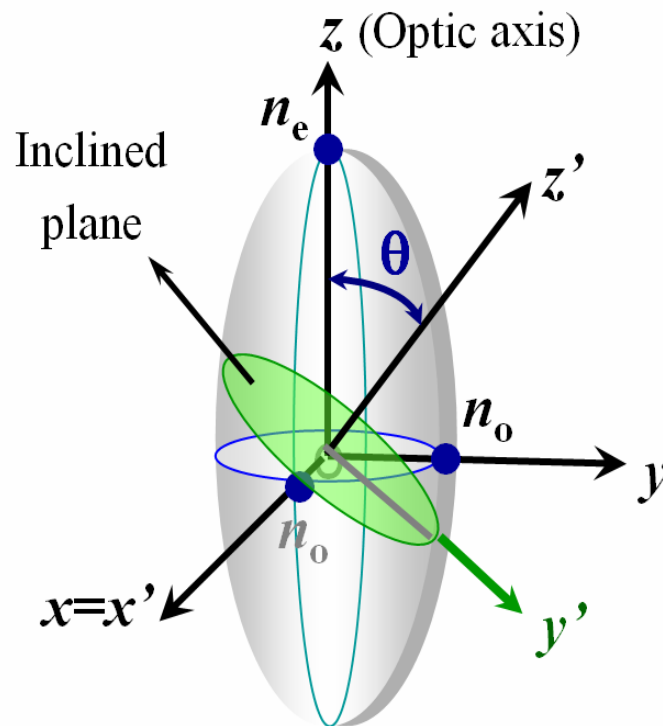
Figure 2.2 Light propagation in uniaxial medium

Similarly, the optical anisotropy is also a function of temperature and approximately linearly proportional to the order parameter *S*. A general trend of the refractive index is plotted in Figure 2.3 as a function of temperature. As we can see, the optical anisotropy decreases as the temperature increases and vanishes in the isotropic phase.
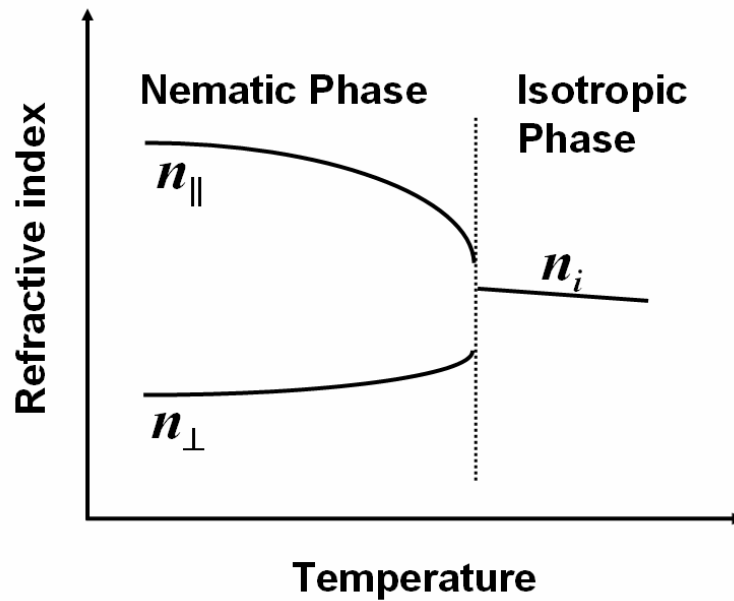
Figure 2.3 A general trend of refractive index as a function of temperature.
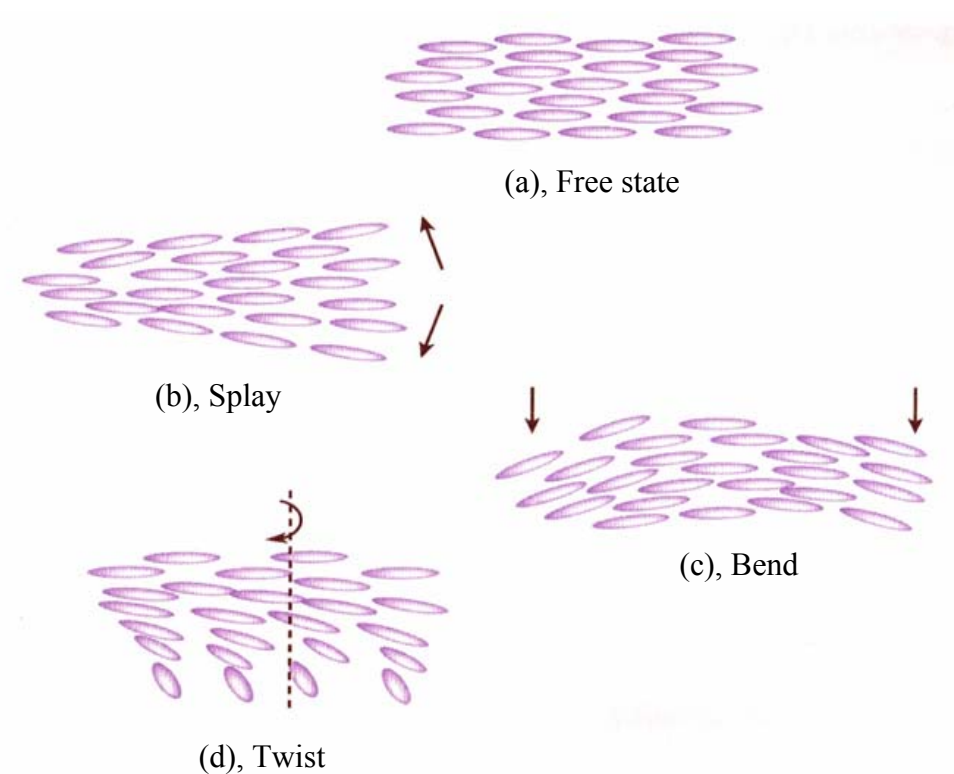
Figure 2.4 Schematic drawing of (a), free state, (b), splay, (c), bend, and (d), twist, in LCs.

2.1.5 Deformations of Liquid Crystal

Like most liquids and solids, LCs exhibit curvature elasticity. The elastic constants of LC determine the restoring torques which arise when the system is perturbed from its equilibrium configuration. These restoring torques are usually very weak compared with those of solids. Any static deformation of LCs can be divided into a combination of three basic deformations. They are splay, twist, and bend deformations, as illustrated in Figure 2.4.

For an isothermal deformation in an incompressible fluid, the elastic energy can be written as a quadratic function of the curvature strain tensor. According to the Oseen-Frank theory, the elastic energy density of a deformed LC can be written as[1,2]

$$F = \frac{1}{2}k_{11}(\nabla \cdot \boldsymbol{n})^2 + \frac{1}{2}k_{22}(\boldsymbol{n} \cdot \nabla \times \boldsymbol{n})^2 + \frac{1}{2}k_{33}(\boldsymbol{n} \times \nabla \times \boldsymbol{n})^2 , \qquad \textbf{(2.5)}$$

where k_{11}, k_{22}, and k_{33} are the splay, twist, and bend elastic constants, respectively.

2.1.6 Liquid Crystal Alignment

Without special treatments of the surfaces, liquid crystal will generally have many domains and many disinclinations, or discontinuities in orientations. These domains and discontinuities can cause a severe scattering of light, leading to a cloudy appearance. To achieve good optical performance, the alignment of LCs is necessary to fabricate practical devices.

There are two common categories of LC alignment on surfaces: homogeneous alignment and homeotropic alignment, as shown in Figure 2.5. Homogeneous alignment occurs when the LC director is parallel to the surface while homeotropic alignment occurs when the LC director is perpendicular to the surface. Both can be achieved by mechanical, chemical, or optical treatments of the surface.
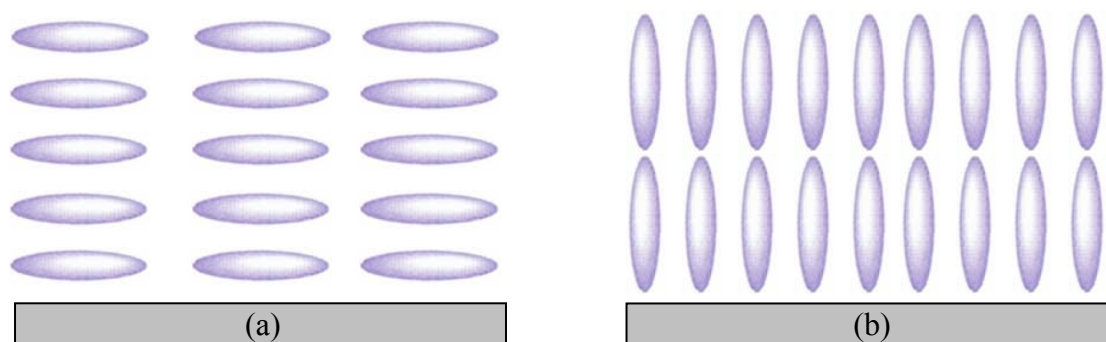
Figure 2.5 Homogeneous alignment (a) and homeotropic alignment (b).

Homeotropic alignments can be obtained by depositing molecules known as silane coupling agents onto a substrate. These molecules can promote the adhesion of LC molecules onto the surface in a vertical manner. The most common way to achieve homogeneous alignment is the surface rubbing, which is widely used in modern LCD technologies. To avoid introducing contaminating impurities or electrostatic charges during rubbing process, noncontact methods, i.e. optical alignment, were also developed. The alignment of liquid crystals by the surface treatment of a substrate has been one of the least understood aspects of the liquid crystal behavior. It depends on both the nature of the liquid crystals and the surface. The most important factors include dipolar interaction, chemical and hydrogen bonding, van der Waals interactions, steric factors, surface topography, and the elasticity of the liquid crystal molecules.

Besides the above listed two kinds of alignment, there is another one, called twisted alignment. For a LC cell with two homogeneously rubbed glass substrates arranged orthogonally, a 90° twisted nematic (TN) cell is formed. Figure 2.6 shows an example of a 90° TN cell operating in the normally white mode. With no polarity and no chirality, both right-handed and left-handed twist of 90° are possible to match the boundary conditions imposed by the rubbing. When a small pretilt angle exists, only one twist is possible in the cell.
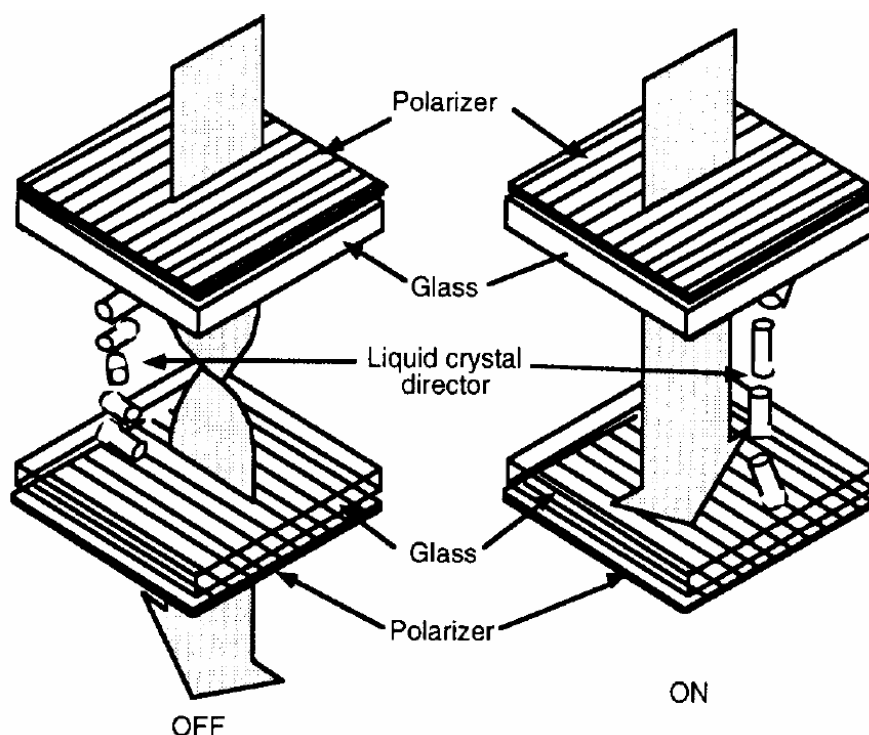
Figure 2.6 Principle of operation of a twisted nematic display in the normally white mode. The local optic axis undergoes a continuous 90° twist in the unactivated state (left), whereas it is predominantly parallel to the electric field in the activated state (right).

2.2 Introduction to Polymer and Photopolymerization

The discovery of polymers has much contributed to the change of day-to-day life. In fact, the use of polymers in human history dates back as early as Egyptian mummies. Before the mummies were wrapped, the cloth was soaked in a solution of oil lavender. When the cloth was dried by exposure to the sunlight, the oil was converted into a protective polymer. This was a typical application of photopolymerization. Polymers are involved in almost all aspects of our lives. Some examples include their use in textile, automotive and electronic industries and as building and packing materials.

(a)   (b)   (c)
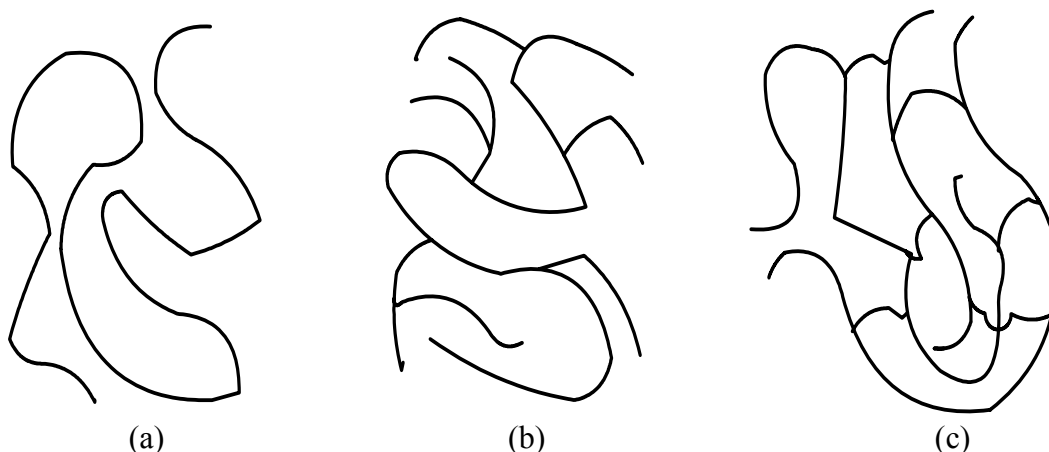
Figure 2.7 Different polymer structures. A linear polymer chain, (a), a branched chain, (b), and a crosslinked network, (c).

Monomers are the building blocks or structural units of the polymers. For the polymer formation, the monomer must be able to link two or more other monomers, i.e., the functionality of the monomer is not less than 2. Depending on the functionalities of the monomer, different morphologies of polymer networks can be formed.[3] If the polymer is constructed from di-functional monomers, it is a linear chain [Figure 2.7(a)]. If higher functional monomers are used, a branched polymer will be formed [Figure 2.7(b)]. The presence of the branches limits the motion of chains, thus strengthening the polymer. If the functionality is even higher, the branches start to connect to one another in three dimensions. The polymer becomes a crosslinked network [Figure 2.7(c)]. This crosslinked network enables the polymer to be much stronger, but also much more brittle.

The most widely used and simple method of polymer formation is radical-chain addition polymerization. Polymerization involves initiation, propagation, transfer and termination steps. Initiation is the step where initiating radicals are formed by external stimulation such as light, heat, gamma-radiation and redox processes. Light induced photopolymerization has several advantages over the other

methods. The fabrication temperature is low, usually room temperature, and controllability can be realized by selecting different irradiation wavelengths and light intensities. Moreover, light can be focused onto a particular site, thus polymer can be formed where it is desired.

Photopolymerization is a very flexible process and can be used in various technological applications such as photo-resists in modern electronics. In this process, a film of monomer mixture is placed on the surface of a silicon wafer and light illumination is focused on the areas in which a polymer covering is desired. After polymerization, the unpolymerized material can be washed away, leaving the photopolymer intact. The polymer-covered areas on the silicon wafer are then used to resist chemical etching, resulting in integrated circuit formation or printed circuit board construction. This technology has allowed billions of transistors to be placed on a single integrated circuit.

2.3 Liquid Crystal and Polymer Composites

Liquid crystal/polymer composites can appear in the form of network or droplet depending on what polymer and concentration are used. Generally speaking, liquid crystal/polymer composites can be divided into two subsystems: polymer-stabilized liquid crystals and polymer-dispersed liquid crystals. Both attract considerable interest, not only for their unique physical properties, but also for their potential applications.

2.3.1 Polymer-Stabilized Liquid Crystals

Polymer-stabilized liquid crystal (PSLC)[4,5] refers to the material system where the polymer concentration (typically 5 wt%) is much lower than that of liquid crystals.

In PSLC, the LC material represents the continuous matrix, while the crosslinked polymer is dispersed in the anisotropic fluid.

The general idea of PSLCs is the stabilization of alignment of the LC by elastic interaction between the dispersed polymer network and LC. After being sandwiched between two pieces of surface-treated glass, the solution was photopolymerized under a UV light source. Then, polymer phase separation and network formation take place. Generally, complete polymerization of a low concentration of monomer takes a very long time. Depending on the order of LC and monomer properties, the polymer network can be isotropic or anisotropic.

Compared to PDLCs, PSLCs can be electrically operated under lower voltage because only a small amount of polymer is dispersed in the LC host. However, the response time is still slow.

2.3.2 Polymer-Dispersed Liquid Crystals

PDLCs consist of liquid crystal droplets that are randomly distributed in a solid polymer matrix. In PDLC, the concentration of polymer is generally more than 20 wt%. The resulting material is a sort of "swiss cheese" polymer with liquid crystal droplets filling in the holes. These tiny droplets (a few microns across for practical applications) are responsible for the unique behavior of the material. By changing the orientation of the liquid crystal molecules with an electric field, it is possible to vary the intensity of transmitted light.

PDLCs can be usually prepared in two ways: encapsulation and phase separation. The first one was introduced by Fergason[6] and Drzaic[7], who dried a polymer solution (polyvinyl alcohol) with emulsified LC droplets. The latter one was reported by Doane *et al*. in 1986.[8] It involved initiating phase separation by thermally polymerizing the polymer precursor. Other phase separation methods such as

evaporation of a solvent from a polymer-LC mixture, temperature-induced phase separation of a LC/polymer mixture on cooling can also be employed. Today the most popular technique is accomplished through the photopolymerization process of a monomer/LC mixture.[9] Usually the monomer is sensitized to the radiation by adding a small amount of suitable photoinitiator. The size of the LC droplets can be well controlled by temperature, exposure intensity, concentration of photoinitiator and properties of reactive components.[10-12]
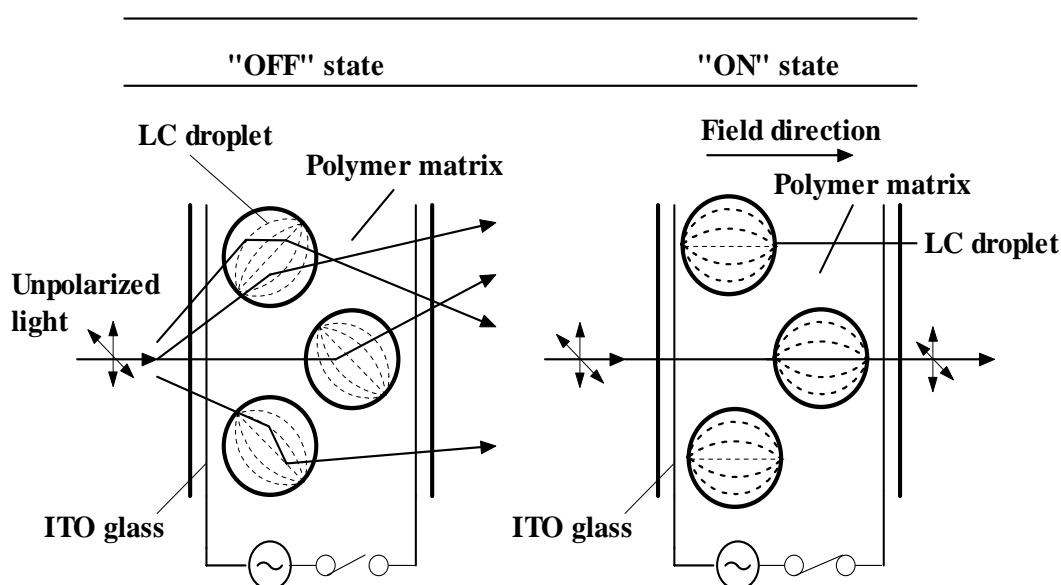
Figure 2.8 Illustration of the principle behind the operation of a PDLC display. The material has a white translucent appearance in the "OFF" state. Application of a voltage to the transparent conducting electrodes reorients the symmetry axis of the bipolar droplets parallel to the electric field direction ("ON" state) and the material becomes transparent if the ordinary refractive index of the liquid crystal matches that of the polymer matrix.

A typical example of PDLCs is the light valve configuration presented in Figure 2.8. The PDLC light valve is fabricated by sandwiching PDLC material between transparent conducting electrodes with a 10-25 μm spacer. In the "OFF" state, the liquid crystal droplets with positive dielectric anisotropy are randomly oriented in the film and the size of the droplets is comparable to or larger than an optical wavelength, usually 2-5 μm. In the translucent state, the film has a white opaque appearance due to the scattering properties of the film. Once an electric field is applied, the liquid crystal molecules in each droplet will align in the direction parallel to the field direction as shown in Figure 2.8 ("ON" state). If the ordinary refractive index, n_o, (perpendicular to the nematic director) approximately matches the refractive index, n_p, of the surrounding polymer matrix, the film will be transparent. Upon removal of the field, the droplets will return to their random orientation and the film reverts back to its opaque state.

This type of display has several advantages over existing liquid crystal technologies. No polarizers are required in PDLC displays. Therefore, PDLC displays are intrinsically brighter than those existing liquid crystal displays that utilize polarizers. Moreover, unlike the conventional liquid crystal displays, a PDLC display does not require alignment layers, therefore simplifying fabrication. On the other hand, a response time approaching about 1 ms is possible with PDLC materials, which is faster than twisted nematic liquid crystal displays. However, the PDLC displays also show obvious disadvantages, such as low contrast ratio and high driving voltage.

The PDLC structure formation through photopolymerization is a complicated process including physical changes and chemical reactions. Usually, the droplets of a nearly uniform size are formed during the phase separation. The average droplet size

varies from the submicron up to several tens of microns depending on the conditions during the formation process. The nematic structure inside a droplet is the result of the interplay between elastic, surface, and external field interactions. The minimization of the phenomenological free energy is usually used to determine the stable structure of a chosen system at constant temperature and volume. It is convenient to divide the free energy density into elastic f_e, interfacial f_s, and field f_f parts.

The nematic free energy density f_e can be expressed as,

$$f_e = \frac{1}{2}[k_{11}(\nabla \cdot \boldsymbol{n})^2 + k_{22}(\boldsymbol{n} \cdot \nabla \times \boldsymbol{n})^2 + k_{33}(\boldsymbol{n} \times \nabla \times \boldsymbol{n})^2 - k_{24}\nabla \cdot (\boldsymbol{n}(\nabla \cdot \boldsymbol{n}) + \boldsymbol{n} \times \nabla \times \boldsymbol{n})].$$ (2.6)

The interaction of the liquid crystal with the surrounding medium is described by a simple contact interaction

$$f_s = (1 - (\boldsymbol{n} \cdot \boldsymbol{e_r})^2)\frac{W_0}{2}\delta(\boldsymbol{r} - \boldsymbol{R}),$$ (2.7)

characterized by $\boldsymbol{e}_r$, the preferred anchoring direction on the droplet surface and the anchoring strength W_0. The vector $\boldsymbol{R}$ in Eq. (2.7) defines points on the droplet surface.

The interaction with an external magnetic field $\boldsymbol{B}$ is described by

$$f_f = -\frac{\mu_0}{2}\Delta\chi(\boldsymbol{B} \cdot \boldsymbol{n})^2,$$ (2.8)

where $\Delta\chi$ is the difference between the principal values of the susceptibility tensor corresponding to the directions parallel and perpendicular to $\boldsymbol{n}$.

The minimization of the total free energy

$$\boldsymbol{F} = \int(f_e + f_s + f_f)d^3\boldsymbol{r},$$ (2.9)

is achieved by solving the Euler-Lagrange differential equations, which lead to the prediction of equilibrium structures. With very few exceptions, the solutions are obtained numerically using relaxation methods.[13,14]
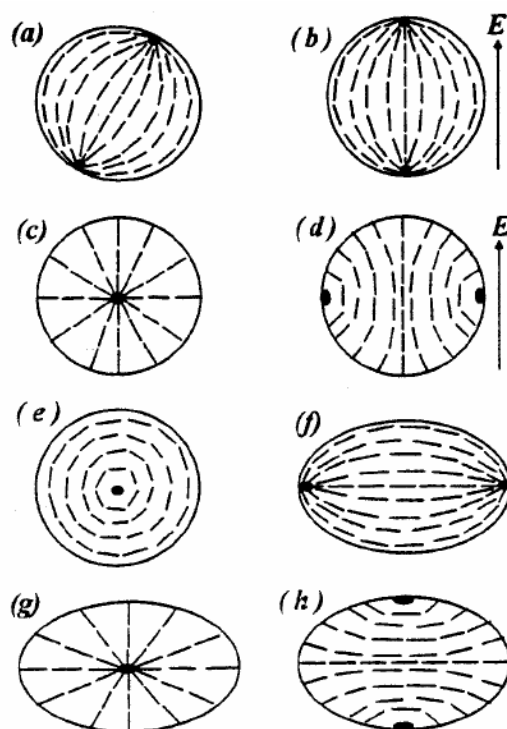
Figure 2.9 Schematic illustration of nematic director configurations in spherical cavities: the bipolar configuration (a), the bipolar configuration aligned by an electric field (b), the radial configuration (c), the axial configuration in an applied field (d), and the toroidal configuration (e). The corresponding bipolar (f), radial (g), and axial (h) configurations in elongated droplets.

The director field configurations of some equilibrium structures are schematically illustrated in Figure 2.9 for spherical and ellipsoid shaped cavities. Figure 2.9(a) and (c) are two of the most commonly observed nematic director configurations that result from parallel and perpendicular boundary conditions, respectively. The effect of an electrid field on the bipolar configuration is to align the symmetry axis parallel to the field with little distortion of the director configuration within the droplet, as shown in Figure 2.9(b). The effect of the electric field on the radial configuration is to induce a configuration transition to the axial configuration

shown in Figure 2.9(d). Particularly in large droplets, metastable structures are relatively diverse. Figure 2.9(e) - (h) have also been reported in some special cases.[15,16] The nematic director configurations in the liquid crystal droplets in PDLCs help to understand the similar things in holographic PDLCs (H-PDLCs), although the droplets in H-PDLCs are usually much smaller (less than 100 nm) than those in PDLCs.

2.4   Summary

The basic properties of liquid crystals and polymers were briefly introduced. Using the basic principles of LC and polymer physics, the properties of LC/polymer composite materials were discussed. In PDLCs, LC droplets were randomly distributed in the polymer matrices. The emphasis of this thesis is to study structured LC/polymer devices. Therefore, a brief review of the structured LC/polymer, i.e. H-PDLC, will be given in the next chapter.

CHAPTER 3   Holographic Polymer-Dispersed Liquid Crystals (H-PDLCs)

3.1   Holography and H-PDLC

Holography is the process of recording the complete information of the electric field in both amplitude and relative phase, and consequently a real three-dimensional image can be reconstructed.[17,18] Since most of recording materials are only sensitive to the intensity of the light, interference is a very convenient way to convert the phase information to the amplitude information. Transmission and reflection holograms are two common types whose images can be reconstructed by appropriate use of optics, such as prisms, lenses, and mirrors. The most attractive and unique property of a hologram is the wavelength and angle sensitivity and the ability to manipulate the light that is either reflected or diffracted. To date, holographic optical elements (HOEs) have found numerous important roles in photonics.

Photopolymers are one of the holographic materials that have been widely used in the fabrication of HOEs. Thin volume gratings can be obtained by holographic interference patterning and subsequent modulation of the refractive index in photopolymer materials. They can be classified into two categories, active and passive devices, depending on their optical function. An element that can change its refractive index dynamically with applied external stimulus, such as electric field, optical strength, forces, is called an active optical element, while an element with a fixed modulation of the refractive index is call a passive optical element.

The marriage of holography and PDLC materials[19] has produced a number of photonic applications in information and display systems, electro-optic filters, free space optical switches, and wavelength division multiplexers. For a typical PDLC, the

LCs are randomly distributed in the polymer matrix and the droplets are randomly orientated, while in H-PDLC system, the interference of two beams generates periodic dark and bright fringes in the photopolymer film. In the photopolymer system, the polymerization rate is higher in the bright region and lower in the dark region. During the holographic recording process, the monomer diffuses into the bright region to form polymer and at the same time LCs diffuse into dark regions. The main advantage of this technique is the fast, single step ability to fabricate large area grating structures.

3.1.1 Transmission and Reflection Gratings

(a)   (b)
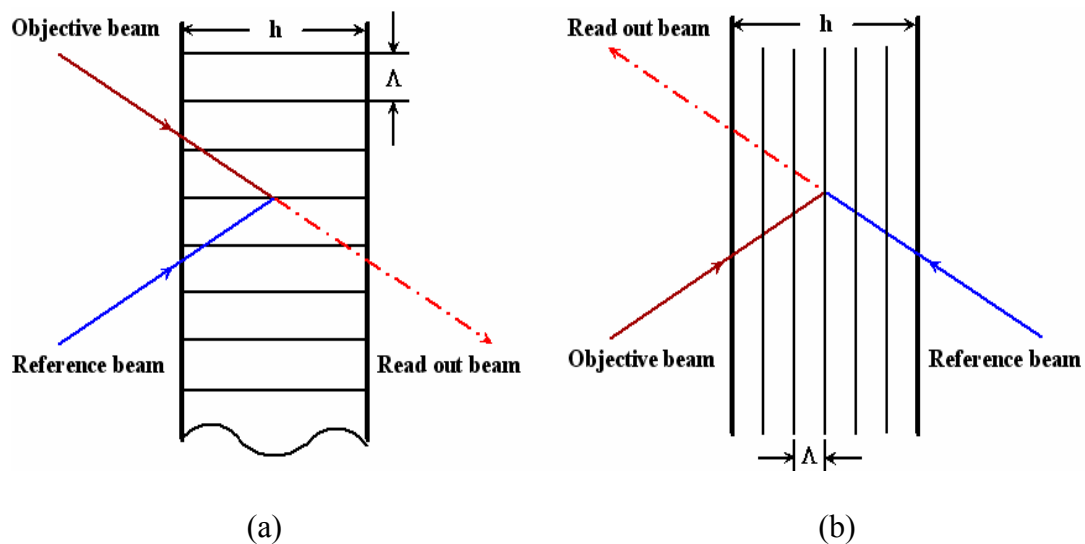
Figure 3.1 Schematic holographic recording for (a) transmission and (b) reflection gratings, respectively.

Depending on the writing geometries, H-PDLC can be divided into two different modes according to the holography recording configuration, transmission and reflection. For transmission H-PDLC, the two recording beams are on the same side of the medium, as shown in Figure 3.1(a). In transmission H-PDLC, the recorded fringes are perpendicular to the substrates. This type of H-PDLC is very sensitive to the incident angle of light beam. On the contrary, for reflection H-PDLC, the

24

recording light beams are on two sides of the recording medium, indicated as Figure 3.1(b). In reflection H-PDLC, the recorded fringes are parallel to the substrates. This type of H-PDLC is very sensitive to the wavelength. Therefore, we can design the grating pitch to reflect red, green, or blue light, which makes it potentially useful in displays. Here, for both reflection and transmission H-PDLCs, the recording light beams are all symmetrical, and therefore the fringes are parallel or perpendicular to the substrates. If the recording beams are not symmetrical, slant fringes will be obtained in H-PDLC.

3.1.2 Raman-Nath and Bragg Gratings

Generally, two types of diffraction are distinguished by defining a dimensionless Cook-Klein parameter Q:

$$Q = \frac{2\pi\lambda d}{n\Lambda^2},\tag{3.1}$$

where d is the thickness of the grating, Λ is the grating period, n is the spatially averaged refractive index of the recording medium, and λ is the incident wavelength.

A "thick" or volume grating ($Q \geq 10$) corresponds to Bragg diffraction and produces diffraction when the incident angle satisfies the phase matching conditions. Such structures exhibit only two diffraction orders (zeroth- and first-order) and a strong dependency of the diffraction efficiency on the angle and wavelength of the incident light. The diffraction efficiency of the transmission volume phase grating in the Bragg condition is described by:

$$\eta_{vol} = \sin^2(\Delta\delta_{vol}/2) = \sin^2(\pi n_1 d / \lambda \cos\theta_0),\tag{3.2}$$

where n_1 is the amplitude of refractive index modulation of the material, and θ_0 is the Bragg angle of the incident light within the material.

On the other hand, "thin" gratings ($Q \leq 1$) correspond to the Raman-Nath regime of optical diffraction. In this regime, many orders of the diffraction can be observed. The efficiency of the first-order Raman-Nath diffraction for the grating with a sinusoidal modulation of refractive index is given by:

$$\eta_{surf} = J_1^2(\Delta\delta_{surf}/2) = J_1^2(2\pi h(n_I - n_{II})/\lambda), \tag{3.3}$$

where $J_1^2(\Delta\delta_{surf}/2)$ is the first-order Bessel function of the first kind, h is the depth of the gratings grooves, and n_I, n_{II} are the refractive indices of the adjacent areas of the grating. It is worth mentioning that for both Bragg and Raman-Nath gratings, the diffraction efficiency is defined as the ratio of diffracted intensity to incident intensity.

3.2 H-PDLC Material Systems

One of the foundamental aspects of research on H-PDLCs is to develop new formulations of materials. All formulations have two underlying components: monomer and liquid crystal. In addition, to improve the performance of H-PDLCs, some other components may be added into the material set, such as photoinitiator dye, cointiator, surfactant, and so on. Both the ratios of these components and the components themselves determine the performance of H-PDLC.

3.2.1 Ultraviolet (UV) Curing

The general material formulation for a UV-curing prepolymer mixture consists of the thiol-ene photopolymers, NOA series (Norland Inc.), and photoinitiator, Irgacure 1173, which is developed by Natarajan and his co-workers, specially for the wavelength of 363 nm from an Ar^+ laser.[20] NOA 65 is the most common one in the series, which is widely used in photonics for adhesion of optical components.

Although the commercial NOA 65 has a proprietary UV initiator, the addition of Irgacure 1173 UV initiator greatly enhances the diffraction efficiency.

The advantages of this kind of material system compared with the acrylate system are smaller shrinkage, more stable electro-optical properties, and long-term stability. The droplets of LC are bigger than those in acrylate systems, leading to a decreased driving voltage. However, the response time is relatively long, on the order of milliseconds.

3.2.2 Visible (Blue and Green) Curing

The above NOA series materials can also be polymerized under visible light exposure if another kind of photoinitiator is doped into these materials. The reflection mode H-PDLC grating was made using NOA 81 doped with Rose Bengal under a 532 nm laser exposure by Wu and Fuh.[21] However, generally, for such kind of materials, it needs high exposure intensity to ensure a good structure grating formation.

In the visible range, the acrylate material system is the most common one used to date, which cures at 488/514.5 nm produced by an Ar^+ laser or 532 nm produced by a frequency-doubled Nd:YAG laser. Sutherland *et al.* first fabricated the Bragg grating using acrylate materials.[19] In this thesis, the materials used are of such kind.

The recipe of the H-PDLC for the visible curing generally contains a multifunctional monomer, chain extender N-vinyl pyrrolidinone (NVP), photoinitiator rose bengal (RB), coinitiator N-phenylglycine (NPG), surfactant, and nematic liquid crystal. The chemical structures of RB, NPG, and NVP are shown in Figure 3.2. The advantages of the photoinitiator (RB) chosen are that it has a broad absorption spectrum in the region of 470-550 nm (as indicated in Figure 3.3) and it is very suitable for excitation with Argon ion laser wavelengths as well as a frequency-doubled Nd-YAG (532 nm).[22]
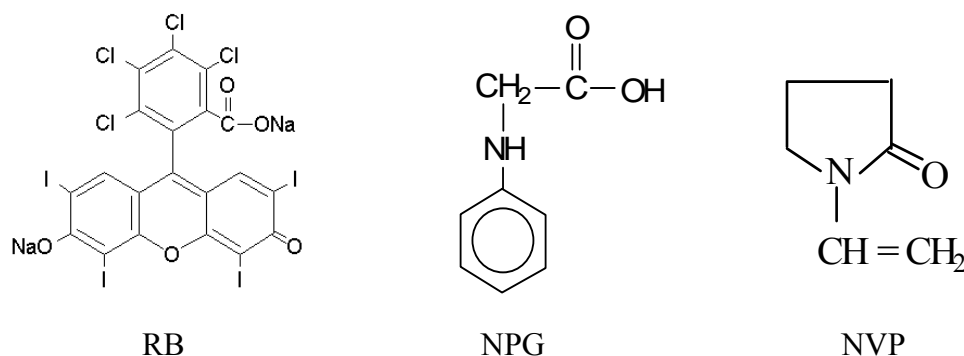
Figure 3.2 Chemical structures of H-PDLC components.
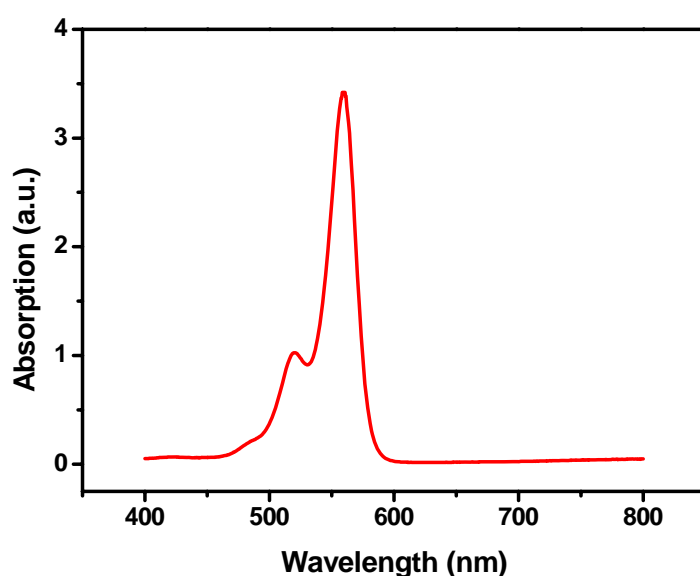
Figure 3.3 Absorption spectrum of the photoinitiator dye RB.

3.2.3 Visible (Red) Curing

Given the abundance and low cost of He-Ne lasers and red diode lasers, the feasibility investigation of recording a H-PDLC grating by utilizing 633 nm wavelength of a He-Ne laser is hence motivated. Ramsey and Sharma firstly reported H-PDLC grating fabrication using a He-Ne laser.[23, 24] An important goal is to fabricate an H-PDLC using a very small power laser and lower the cost of the fabrication.

The material system for He-Ne laser curing is composed of monofunctional acrylic oligomer, CN135, cross linker, SR295, and initiator (photo-oxidant dye), methylene blue and coinitiator, p-toluenesulfonic acid.

3.2.4 *Near Infrared (NIR) Curing*

The development of H-PDLC material systems for NIR curing also attracts considerable attention. Pilot *et al.* developed the material system under NIR range in 1999. [25] The materials used include monomer, Di-penta-erithrithol-penta-acrylate (DPEPA) doped with 2-ethoxy-ethoxy-ethyl acrylate ester (2EEEA), Cyanine dye, IR-140, initiator, ethyl-di-methyl-amino-benzoate (EDMABzt), and electron donor, CBr4. An 834 or 850 nm laser diode was used to illuminate the material. The material can achieve good resolution (2500 lines/mm) and shows excellent long-term chemical stability. However, as for the acrylate system, the switching voltage is still relatively high.

3.3 *Fabrication*

The prepolymer and LC were mechanically blended according to the appropriate weight ratio and stirred in an ultrasonic cleaner at an appropriate temperature (higher than the clearing point of the liquid crystal) for at least 2 hrs to form a homogeneous mixture in the dark. After that, the mixture was injected in a cell by capillary effect, which was formed by two pieces of indium-tin-oxide (ITO) coated glass, and then subjected to laser exposure. The cell thickness can be controlled by the bead spacers between the two pieces of ITO glass. During exposure, the pattern formed by two interfering beams was recorded in the LC cell. After exposure, the samples were further cured for 15 minutes by mercury lamp to ensure the complete polymerization of prepolymer.

Depending on the writing geometries, transmission and reflection mode gratings can be fabricated. In the case of writing transmission gratings, the writing beams are co-incident on the same side of the sample with an angle between the two writing beams and the resulting grating vector is parallel to the substrates. In reflection gratings, the writing beams are counter-propagating and the resulting grating vector is perpendicular to the substrates. Figure 3.4 shows the specially designed setups to fabricate the transmission and reflection gratings, respectively. The use of single prism in the fabrication setups decreases the complexity of the optics. More importantly, the setups are self-adaptive, i.e. the effect of the external vibration during the fabrication process is minimized. The LC cells filled with propolymer mixture stick onto the hypotenuse of the prism using the index matching liquid.
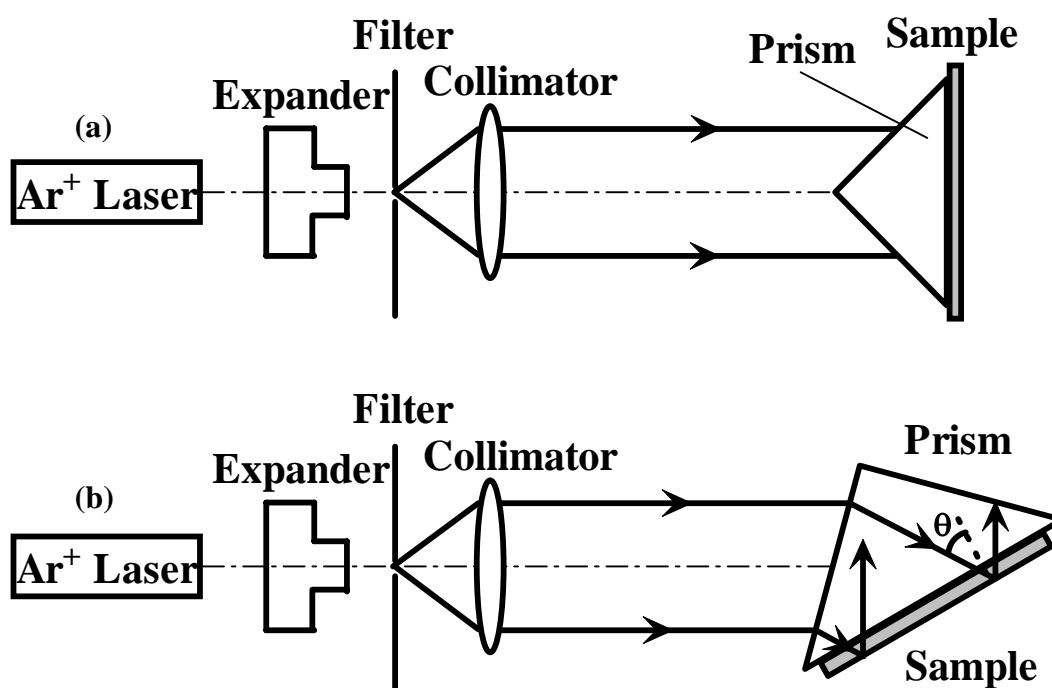
Figure 3.4 Experimental setups of holographic transmission (a) and reflection (b) grating recording, respectively.

30

3.4   H-PDLC Properties

3.4.1 Diffraction Efficiency

For H-PDLC, diffraction efficiency is an important parameter. Because H-PDLC operates in true Bragg regime, the diffraction efficiency can be very high. Theoretically, it can reach 100%. However, in reality, because of scattering and other reasons, it is generally 60%~70%. Applying Kogelnik's scalar coupled-wave theory,[26] the diffraction efficiency can be theoretically calculated. According to the theoretical results, many problems can be explained and also the diffraction efficiency can be optimized. This gave an effective guide in improving the diffraction efficiency. However, although Kogelnik's scalar coupled-wave theory can give a satisfactory explanation to H-PDLC, it is sometimes not completely suitable to H-PDLC. As is well known, liquid crystal is a kind of anisotropic material with a large birefringence. Combining anisotropic coupled-wave theory with an elongated liquid-crystal-droplet switching model and including the effects of a statistical orientational distribution of droplet-symmetry axes, Sutherland developed a modified model to describe the angular and polarization-dependent switching behavior of H-PDLC gratings. [27] Experimentally, the diffraction efficiency was improved according to the material recipe and exposure conditions.[28,29]

3.4.2 Electro-optical Properties

Truly the most intriguing and useful things about H-PDLCs are their electro-optical properties, in particular the electrically controlled switchability. Many of the theoretical studies on PDLCs can be used with H-PDLCs. The nematic liquid crystal ordering, optical scattering, and electrical switching of small LC droplets in PDLCs have been discussed extensively in the literature.[8,30-32] Sutherland *et al.*[33] used the

model proposed by Wu *et al.*[34] to model the properties of H-PDLCs and obtained satisfactory results. For practical applications, the big problem is that the switching voltage is too high compared to conventional PDLC or bulk liquid crystal displays. The switching voltage is generally more than 10 V/μm. Adding a small portion of surfactant [35-38] has been proven to effectively decrease the switching voltage. Natarajan *et al.*[20] studied another material system based on thiol-ene photopolymerization to improve the electro-optical properties. De Sarkar *et al.*[39] studied the influence of monomer fluorination on the electro-optical properties. Morphologies observed by SEM are used to optimize the electro-optical properties.[40-42] The effect of monomer functionalities was also studied in detail.[28,43-45] Different monomers are also used to improve the electro-optical properties.[46-50]

3.4.3 Response Time

The response time for H-PDLC is about 100~200 μs (turn-on + turn-off time), which is very fast compared to conventional PDLCs (tens of milliseconds). This fast response speed can meet a lot of applications which demand high switching speed, such as video displays, optical communications, and so on. The fast response time comes from the nanoscale liquid crystal droplets, which makes the liquid crystal molecules easy to orientate under high electric field. The mechanism was discussed in some of the literature in detail.[33,37]

3.5 H-PDLC Applications

3.5.1 Displays

Many concepts of H-PDLC displays have been proposed.[51-58] For high brightness, all concepts are based on a stack of red (R), green (G), and blue (B) reflective H-PDLCs, as indicated in Figure 3.5. Each layer is pixilated and separately

addressed. The bottom layer is a black absorber. This type of device works in ambient light. When the white light is incident on the stack and all three gratings are fully powered, the stack appears black. With the voltage to all three off, the reflected light appears white, having a good color balance from the spectral reflectance of all three gratings. Other colors can be achieved with the following schemes: (a) red (R-voltage off; G, B-voltage on); (b) green (G-voltage off; R, B-voltage on); (c) blue (B-voltage off; R, G-voltage on); (d) yellow (R, G-voltage off; B-voltage on); (e) magenta (R,B-voltage off; G-voltage on); and (f) cyan (G, B -voltage off; R -voltage on); Diffraction efficiency in reflective H-PDLC gratings is ~70% and in special configurations can exceed 90%, with a bandwidth of ~20 nm. This is sufficient to give high color purity and a wide gamut of color. The on-off dynamic range (i.e. contrast ratio) can exceed 30 dB. With response time and relaxation times of ~25-45 μs, the switching time is fast enough for video rates. By recording a diffuse hologram directly into the LC/polymer film, the diffuse mode H-PDLC exhibits large viewing angles with an order of magnitude larger than the conventional mode.[59]
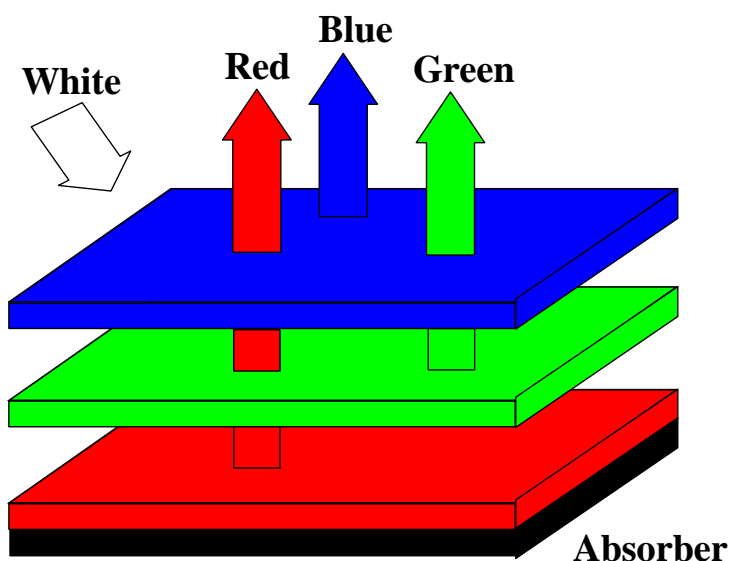
Figure 3.5 Schematic illustration of reflective H-PDLC display

3.5.2 Information Storage

Tondiglia *et al.* first reported that image storage could be holographically recorded in an economical PDLC material by a fast, single-step recording method.[60] Near-IR sensitive material systems for data storage were also studied by Pilot and his co-workers.[25,61,62] There is no wet or dry chemical postprocessing or hologram fixing for such a holographic method. The image can be read out electro-optically with repeatable, reversible erase-and-restore cycles. The recording and reading of holograms are conveniently done at room temperature. Reasonable switching fields of approximately 5-15 V/μm with response times in the 20 - 40 μs range were achieved. It is believed that this holographic material has a potential for large data storage capacity because of the high diffraction efficiency, narrow angular selectivity, and high image quality.

3.5.3 Switchable Lenses

Conventional optical zoom lenses are heavy, bulky, and mechanical. As such they are difficult to handle, produce fatigue, and are subject to wear after repeated use. Electrically controlled dynamic focus lenses with no moving parts are of tremendous interest, particularly if they can be made flat and lightweight. Most approaches to dynamic focus lenses have utilized LCs in some form, such as layers of liquid crystal captured in etched relief structures,[63] or structured electrodes.[64] Non-LC approaches include the use of volume holography to store a set of prerecorded lenses and recall them by random phase addressing.[65] Previously Sutherland *et al.* demonstrated switchable focusing in Polaroid DMP photopolymer infused with LCs.[66] Intriguing possibilities include reading spectacles for which the focus or magnification can be electrically controlled. Another area is that of lightweight

cameras which zoom from wide angle to telescope with no moving parts. [67] Switchable lenses are also of interest for autofocusing systems, tracking in CD pickups, and in-depth optical data storage systems (e.g., DVDs or volume storage media). N switchable lenses combined with one conventional lens yields a system with 2^N finite focal lengths (shown in Figure 3.6), which can be thought of as a digital zoom lens.
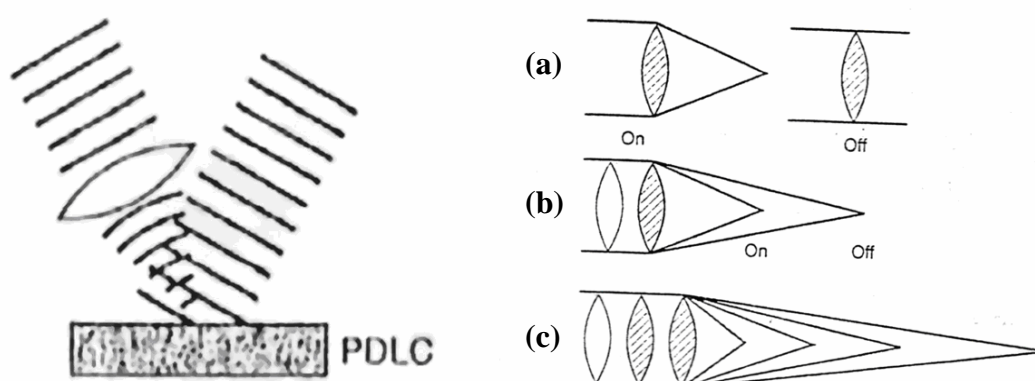
Figure 3.6 Schematic illustration of holographic recording for switchable lens in the left side. The right side shows (a) Switchable diffractive lens, (b) Combined with conventional lens for two finite focal lengths, (c) 2^N foci from N switchable lenses, respectively.

Domash and his coworkers explored several techniques for forming a holographic lens in a transmission H-PDLC system. [68] The best performance was obtained by combining the converging output of a 100 mm aperture doublet, diffraction-limited Fourier lens ($f = 330$ mm) with a collimated beam (at 488 nm) to form a transmission holographic lens. The hologram focused incident 488 nm-light to a spot size of six pixels on a 768×494 -pixel CCD camera. This is equivalent to 8 pixels at 633 nm, the same spot size achieved at this wavelength using the

conventional lens. The diffraction efficiency was 71%. Applying a field of 9.2 V/μm, the lens could be switched off, with a contrast ratio of approximately 100:1. With this type of technology, it is possible to shift optical power between widely separated focal points on a 10-50 μs time scale.

3.5.4 Photonic Applications

- *Beam Steering for Defence*

H-PDLC Bragg gratings [also called electrically switchable Bragg gratings (ESBGs)], whose early development was motivated by military requirements to protect pilots and sensors from harmful battlefield lasers, continues to be evaluated for applications to defense, particularly the rapid steering of laser beams with no moving parts. While other technologies exist for steering of laser beams over small but continuously varied angles. ESBGs appear potentially useful for efficient, switchable deflection into large angles. Figure 3.7 shows a conceptual design for the use of ESBGs to perform steering over wide angles in combination with other technologies for small angle steering.[69] This system will require that H-PDLC materials withstand high laser power fluences in the mid-IR.
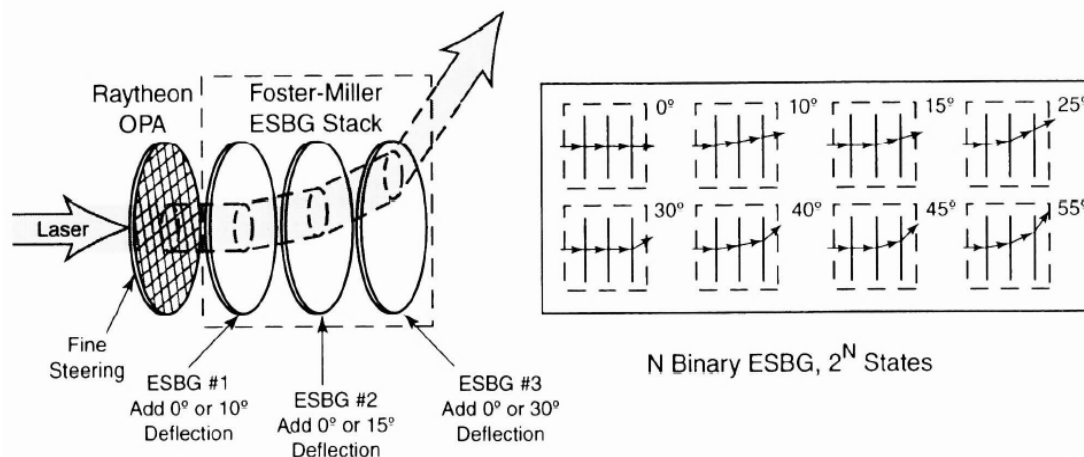
Figure 3.7 The concept of agile beam steering based on ESBG.

- *Add/Drop Multiplexers/Demultiplexers Based on H-PDLC*
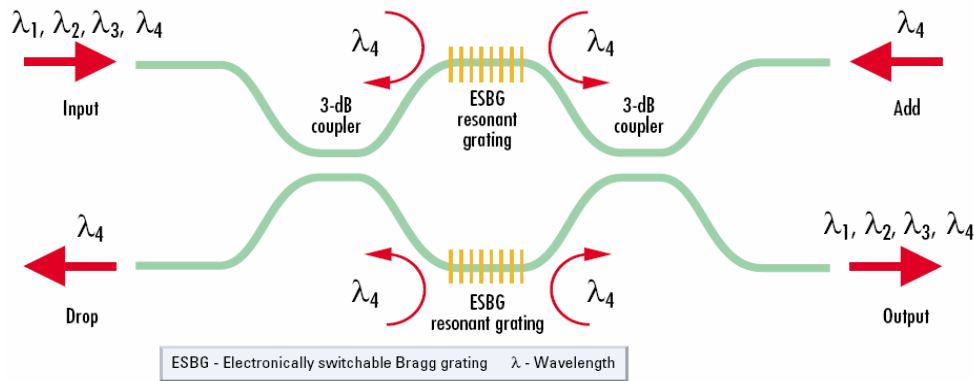
Figure 3.8 ESBGs based grating-assisted planar-waveguide Mach-Zehnder coupled optical add/drop multiplexers/demultiplexers. In this optical add/drop multiplexer, both arms of the Mach-Zehnder interferometer have electronically switchable Bragg gratings at the wavelength of interest, λ_4, which enables the device to drop that channel.

H-PDLC has significant potential in optical communications. Its fast response and electrically switchable ability make it very promising. Digilens (a US based company) [70] has developed an H-PDLC grating based grating-assisted, planar-waveguide Mach-Zehnder coupled optical add/drop multiplexers/demultiplexers, as shown in Figure 3.8. Gu *et al*. also developed a similar structure to realize a 2×2 optical switch.[71] It can be seen from Figure 3.8 that, in this OADM, both arms of a Mach-Zehnder interferometer have ESBGs at the wavelength of interest, λ_4, making it possible to drop that channel. By electrically erasing the gratings, all wavelengths pass through and remain unaltered. The symmetry of the device also provides the corresponding possibility to add as well as drop simultaneously, offering the full OADM functionality. The placing of additional matched pairs of gratings with

different resonant wavelengths would permit the OADM to drop or add several different wavelength channels at once.

For communication systems, channel cross-connection (i.e., routing signals from individual input ports to one or more selected output ports) is a required function. The great advantage of this device is that H-PDLC gratings allow this function to be implemented in the optical rather than electronic domain, eliminating the substantial cost associated with electronic/optical conversion.

3.5.5 New Development of H-PDLCs

In the last several years, new applications have been developed based on H-PDLC, mainly in three aspects: (i) mirrorless lasing from dye-doped H-PDLC, (ii) H-PDLC PhCs, and (iii) sensing applications. It is believed that H-PDLC will have additional applications in photonics.

- *Mirrorless Lasing from Dye-Doped H-PDLC*

The dye-doped H-PDLC grating (regardless of reflection or transmission mode) itself serves as both a resonant cavity and a gain medium, making it promising in electrically tunable lasers with low threshold. In 2003, Jakubiak *et al.* demonstrated distributed feedback (DFB) lasing from dye-doped H-PDLC reflection grating.[72] Lucchetta *et al.* reported lasing emission from a simple wafer structure using an H-PDLC reflection grating as a reflection mirror[73] and later achieved light amplification in a dye-doped H-PDLC reflection grating.[74] Much work has been done in the past two years employing the dye-doped H-PDLC lasing effect.[21,75-77] The lasing emission can also be obtained using the H-PDLC grating only as a distributed feedback element by He and his co-workers.[78] Most of above work regarding the lasing emission are based on H-PDLC reflection gratings. However, in such cases, the overall gain length is limited to the thickness of the film. To increase the lasing efficiency, it is desirable

to increase the film thickness. However, in reflection geometry, an increase of film thickness results in an increase of the required switching electric field. Thus, a tradeoff between cavity length and switching field is necessary. This problem can be overcome if the H-PDLC transmission mode grating is used. Hsiao *et al.* reported the lasing emission from a dye-doped H-PDLC transmission grating.[79] Compared to the reflection mode, the transmission mode grating offers a longer gain length without increasing the film thickness.

- *H-PDLC PhCs*

Recently, much interest was focused on fabricating PhCs based on H-PDLC. As a new class of photonic bandgap material, combining the holography technique and electrically controlled switchability, H-PDLC PhCs showed many advantages over conventional PhCs, including single-step and easy fabrication, field dependent switchability, and fast response. Tondiglia *et al.* first fabricated H-PDLC PhCs in 2002.[80] Many 2D and 3D PhCs have been demonstrated using H-PDLC materials, including orthorhombic,[81] face-centered cubic,[82] transverse square,[83] diamondlike lattices,[84] and Penrose structure.[85] Using three and four coherent beams, five 2D and all fourteen 3D Bravais lattices can be formed using H-PDLC materials, respectively.[86] With five or more beams, the quasi-crystal structures were also investigated.[87,88] Some special applications based on H-PDLC PhCs were explored, including lasing emission.[72,89] However, the low refractive index difference between the liquid crystal and polymer matrix hinders H-PDLC photonic crystal applications.

- *Sensing Applications Based on H-PDLC*

Sensing is another big potential application for H-PDLC gratings, especially for reflection mode. Fontecchio *et al.* developed hydrostatic pressure sensors based on H-PDLC reflection gratings.[90,91] With a special treatment, the reflective H-PDLCs

can contain many air voids without any damage to the grating structures. An easy way to create the voids in H-PDLCs is to simply add a non-reactive solvent, such as acetone or toluene, into the prepolymer mixture prior to holographic exposure. After exposure, the porous acrylate polymer grating structures can be created when the nonreactive solvent evaporates upon exposing the polymerized film to air. This porous H-PDLC reflection grating can be used to detect chemical vapor.[92]

3.6 Challenges of H-PDLC

H-PDLC has many advantages so that it becomes one of the most promising electro-optical materials in some research fields, such as optics, displays, and communications. However, a lot of issues exist in H-PDLC, which intensely influences the practical applications. In detail, these issues are listed as below.

3.6.1 Driving Voltage

In H-PDLC, the LC droplets are so small (usually on the order of nanometers) that the surface area of interaction between the polymer matrix and LC droplets is strongly enlarged, and hence the anchoring energy of the LC droplets is greatly increased. Thus, a high driving voltage is needed to reorientate the directors of the LC molecules. This is the main reason why the driving voltage in H-PDLC gratings is higher than that in conventional PDLC devices. How to reduce the driving voltage is the key for H-PDLC applications. Colegrove *et al.* reported that by adding a high dielectric anisotropy material ($\Delta\varepsilon = 65$), the threshold voltage of HPDLC can be reduced significantly.[93] Partial fluorination of the host polymer matrix is also beneficial to decrease the driving voltage.[39, 94] However, the response time also increases due to the fluorination. In addition, adding a small portion of surfactant to the prepolymer/LC mixture also helps to reduce the threshold voltage.[36,95-97]

3.6.2 Aging (Lifetime)

The lifetime of H-PDLC is also a problem to be solved. Without any sealing, the performance of H-PDLC will decay quickly after two or three months. One possible reason is that the exposure is not long enough. So after exposure, the materials can still continue to react with each other under the ambient light. Another reason is that the materials themselves are not stable. They react with, for example, oxygen in the air. The third reason is that, the materials when operated under high electric field are vulnerable to breakdown. H-PDLC is a switchable device controlled by electric field. However, after repeating many times, the material property may be altered.

3.6.3 Viewing Angle for Displays

For reflective display applications, H-PDLCs have several advantages, such as the potential for bright full color displays[56] with large color gamut. Since a very narrow band of light is reflected, the color purity of the display is excellent. However, because the reflective H-PDLC grating observes Bragg's law, the angle sensitivity (i.e. viewing angle) of reflective H-PDLC is relatively narrow. This is not favorable for displays that demand people see the images from pre-defined angles. The viewing angle can be improved by introducing noise into the hologram during formation with a diffusing element.[59, 98]

3.6.4 Polarization Dependent Loss for Optical Communications

For practical optical communications, polarization-dependent loss (PDL) is a big concern. Generally in H-PDLC, the conversion of the monomer molecules into a polymer network is accompanied with closer packing of molecules, which leads to contraction of the composite known as polymerization shrinkage. When the polymer

shrinks, the LC droplets are compressed, which preferentially aligns the symmetry axis of the rod-shape LC molecules in the droplet along a common direction. This results in polarization sensitive diffraction since the optical axis is on average along the same direction for all droplets, therefore making diffraction efficiency sensitive to the input polarization. How to effectively decrease the PDL is still a challenge to researchers.

3.7   *Characterization Methods*

3.7.1 *Structural Properties*

- *Morphology*

For morphology analysis, samples with one of the ITO glass plates removed are soaked in ethanol for more than 12 hrs in order to completely remove the LC. After drying, the morphologies can be investigated by high resolution optical microscope, atomic force microscopy (AFM), or scanning electron microscope (SEM).

AFM (Dimension 3000 Scanning Probe Microscope, Digital Instruments) is used to measure the surface morphology of the films. The root mean square (RMS) roughness is obtained from the digital image-processing package of the AFM system.

Field emission gun scanning electron microscopy (FEG-SEM) (JEOL JSM 6700F) is used to observe the surface morphology of the films. Since the H-PDLC films are non-conductive polymers, a thin layer of gold or platinum is coated on the H-PDLC surface by a JEOL JFC-1200 Fine Coater in order to eliminate the charging effect.

3.7.2 *Electro-optical Properties*

- *Diffraction Efficiency*

For the switchable volume gratings, diffraction efficiency is a very important parameter. It is defined as the diffracted power in the first order divided by the incident power. All samples were measured using a polarized He-Ne laser ($\lambda = 633$ nm) at room temperature. The diffraction efficiencies for *p*- and *s*-polarized light were measured and compared, respectively.

- *Response Time*
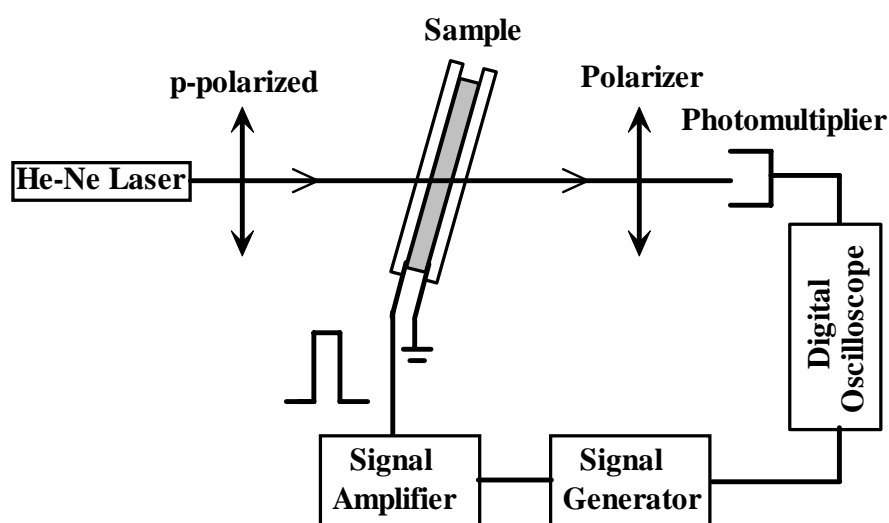
Figure 3.9 Measurement setup of the response time.

Figure 3.9 shows the measurement setup for response time measurements. Polarized light from a He-Ne laser was used for the diffraction/transmittance properties and the response time studies. The laser beam was incident on the sample at the exact Bragg angle, and the diffraction was measured by a photomultiplier. In the measurements, the H-PDLC Bragg grating was driven by an AC signal with various frequencies. In our measurement, a high voltage amplifier/function generator (Trek, Model: 609E-6-FG) is used to generate the AC signal with different waveforms and frequencies. For the response time measurements, the photodetector signal was fed into one input channel of an oscilloscope (Agilent, Model: 54641A). The voltage signal, which was used to trigger the oscilloscope, was fed into another input channel

of the oscilloscope. From the waveforms captured by the oscilloscope, the rise and fall times can be obtained.

3.8 Summary

In this chapter, a review of H-PDLC was presented. The material formulations, fabrications, properties, applications, and drawbacks regarding the H-PDLC gratings were discussed in detail. The characterization of H-PDLC was also described.

CHAPTER 4   Optimization of H-PDLC Performance

For H-PDLC based devices, many factors influence their performance, such as the material recipe, including the chosen materials and the ratio of every component, fabrication conditions, including exposure intensity and time, exposure temperature, etc. To achieve high performance H-PDLC devices, one should optimize both the material recipe and the fabrication parameters. In this chapter, we will first show the chemical reactions in the formation process of H-PDLC and theoretically investigate the factors which affect the performance of the H-PDLC Bragg gratings, concentrating on the diffraction efficiency, using Kogelnik's coupled wave theory. Then, we experimentally optimized the material recipe based on our previous experience and investigated the effect of surfactants on the electro-optical properties. With the optimized material recipe, a polarization insensitive 2×2 optical switch was fabricated and characterized.

4.1   Theoretical Investigation

4.1.1 Formation Kinetics of H-PDLC

The grating formation process is outlined in Figure 4.1. Grating formation ensues when the material is irradiated with a sinusoidal intensity pattern. In the bright regions, absorption by the photoinitiator results in a highly reactive triplet state. The co-intiator undergoes an electron-transfer reaction with this triplet state to create a free radical. Free-radical polymerization is then initiated. The presence of the chain-extender promotes cross-linking of the polymer chains produced. The result is a rapid consumption of monomers and polymer growth in the bright regions of the intensity pattern.

(a) Homogeneous mixture before exposure

(b) The exposure intensity distribution is sinusoidal. In the bright region, the monomer polymerizes first. The liquid crystal diffuses to the dark region.

(c) Finally, alternate polymer-rich and liquid crystal region formed. The refractive index is modulated along *x* axis direction.
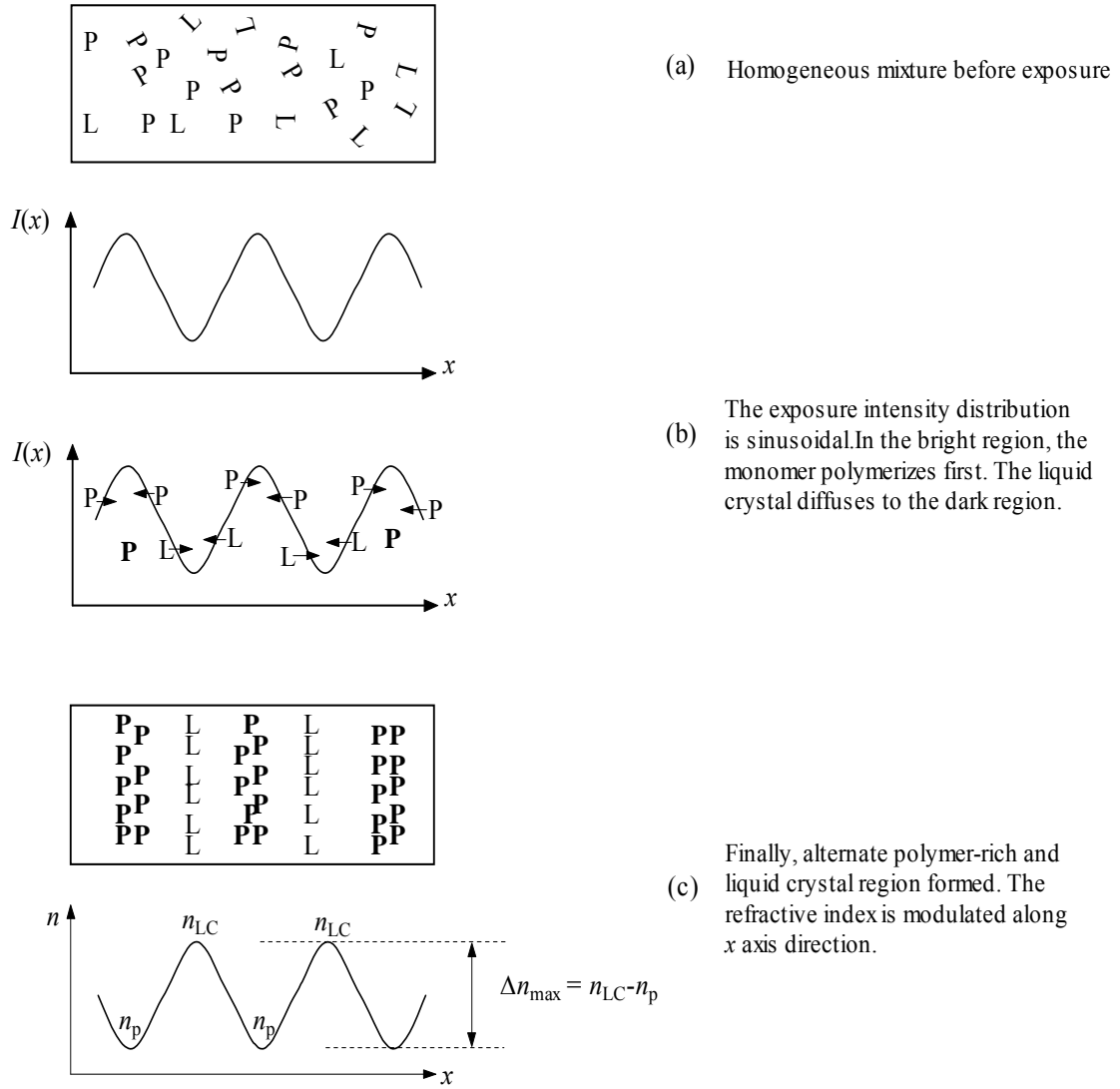
Figure 4.1 Schematic formation process of H-PDLC gratings.

Ignoring interactions between various components, the chemical potential for the *i*-th component of the mixture may be approximated by

$$\mu_i = \mu_i^0 + k_B T \ln\left(\frac{N_i}{\sum_j N_j}\right)$$

(4.1)

where μ_i^0 is the chemical potential of the pure *i*-th component, N_i is the number of molecules of the *i*-th component, k_B is Boltzmann's constant, and T is the absolute temperature. Under thermodynamic equilibrium, the sum of μ_i is a constant. A

gradient in the light intensity preferentially initiates photopolymerization in the high intensity regions. Since the mixture is dominated by monomer and LC components initially, we see that the chemical potential of the monomer decreases while that of the LC increases in the bright regions. In the neighboring dark regions, at least for early times, the chemical potentials are all equal to their initial equilibrium values. Hence, spatial gradients in the chemical potential are established which produces a diffusion of monomers (and other reactants) into the bright regions, and a counter-diffusion of LC into the dark regions. This process continues until a new equilibrium chemical potential is established.

As the growing polymer network propagates outward into the dark regions, gelation of the system ensues. Fluctuations in the free energy of the system result in local minima where a distinct LC phase begins to form. Similar to the discussion of the droplet formation in PDLCs in section 2.3.2, the total droplet energy is minimized at a critical droplet radius, *Rc*, which is proportional to the surface tension of the droplet, σ. A droplet of this size will be stable and can grow if more LC molecules are available for incorporation or if coalescence with a nearby droplet is feasible. Growth will eventually terminate when the surrounding polymer rigidly locks the droplet in place and prevents further LC diffusion.

A big disadvantage of free-radical photopolymerization is its susceptibility to oxygen inhibition. This inhibition is particularly problematic in thin-film and coating applications where oxygen diffusion plays a significant role in increasing cure times, which often results in incomplete conversion.[99,100] When oxygen, which is essentially a biradical in its electronic ground state, reacts with a free-radical, it forms a peroxy radical, which is much less reactive.

As a result, the kinetic reactions of photoinduced free radical polymerization can be summarized by the following four steps:

Initiation:

$$I \xrightarrow{h\nu} R^{\bullet} \tag{4.2}$$

$$R^{\bullet} + M_n \xrightarrow{k_i} M_n^{\bullet} \tag{4.3}$$

Propagation:

$$M_n^{\bullet} + M \xrightarrow{k_p} M_{n+1}^{\bullet} \tag{4.4}$$

Termination:

$$M_n^{\bullet} + M_m^{\bullet} \xrightarrow{k_{tc}} M_{n+m} \tag{4.5}$$

$$M_n^{\bullet} + M_m^{\bullet} \xrightarrow{k_{td}} M_n + M_m \tag{4.6}$$

Inhibition by Oxygen:

$$M^{\bullet} + O_2 \longrightarrow M - O - O^{\bullet} \tag{4.7}$$

$$M - O - O^{\bullet} + M \longrightarrow No\ Reaction \tag{4.8}$$
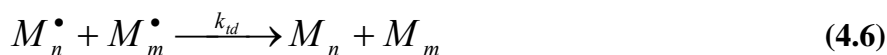
Physically, the formation of the H-PDLC gratings can be well simulated using a 1D diffusion model. Assuming the monomers are free to diffuse in the materials, a 1D diffusion equation can be written for the monomer concentration as follows

$$\frac{d\phi(x,t)}{dt} = -F(x,t)\phi(x,t) + \frac{d}{dx}\left(D(x,t)\frac{d\phi(x,t)}{dx}\right) \tag{4.9}$$

where $\phi(x,t)$ is the monomer concentration, $F(x,t)$ is the polymerization rate, and $D(x,t)$ is the diffusion rate.

When monomers react and bind with the growing polymer radical, free volume is generated since the covalent single carbon bond in the polymer is as much as 50% shorter than the van der Waals bond in the liquid monomer state. The

mechanical response of the medium to reduce this free volume leads to physical shrinkage of the system. A volume shrinkage rate z can be defined by specifying that a unit volume of monomers shrinks to a volume of $1/(1+z)$ of polymer. Therefore, the concentration of the polymer can be written as,

$$\psi\left(x,t\right)=\int_0^t \frac{1}{1+z}F(x,t^{'})\phi(x,t^{'})dt^{'} . \tag{4.10}$$

The concentration of liquid crystal can be written as,

$$\eta(x,t)=\int_0^t[\frac{z}{1+z}F(x,t^{'})\phi(x,t^{'})-\frac{d}{dx}\left(D(x,t^{'})\frac{d\phi(x,t^{'})}{dx}\right)]dt^{'} . \tag{4.11}$$

In the whole system, $\psi(x,t)$, $\phi(x,t)$, and $\eta(x,t)$ satisfy the equation of $\psi + \phi + \eta = 1$. So there are only two independent parameters in this system. Many researchers studied the H-PDLC grating formation using this simple model.[101, 102] Kyu *et al.* gave a 2D simulation using time-dependent Ginzburg-Landau equations (TDGL model C).[103]

4.1.2 Coupled Wave Theory

The basic interaction geometry of the incident light with the holographic film, LC droplets, and applied field is illustrated in Figure 4.2. The grating is described by grating vector **K**, which is perpendicular to the grating planes. Generally, the grating vector makes an angle φ with respect to the film normal. Light is incident on the film at an angle θ, as measured in the medium. For simplicity, we assume that the holographic film is sandwiched between index matching windows. Light polarized perpendicular to the plane of incidence (defined by the incident wave vector and the film normal, which are coplanar) is said to be *s*-polarized. Light polarized in the plane of incidence is said to be *p*-polarized. Each LC droplet is taken to be a uniaxial

domain, with its axis of symmetry along the applied electric field. The applied electric field is normal to the film. Here, we define a vector N as the droplet director. In the absence of an electric field, N preferentially coincides with the droplet-symmetry axis, which is also the major axis of the elongated droplet.
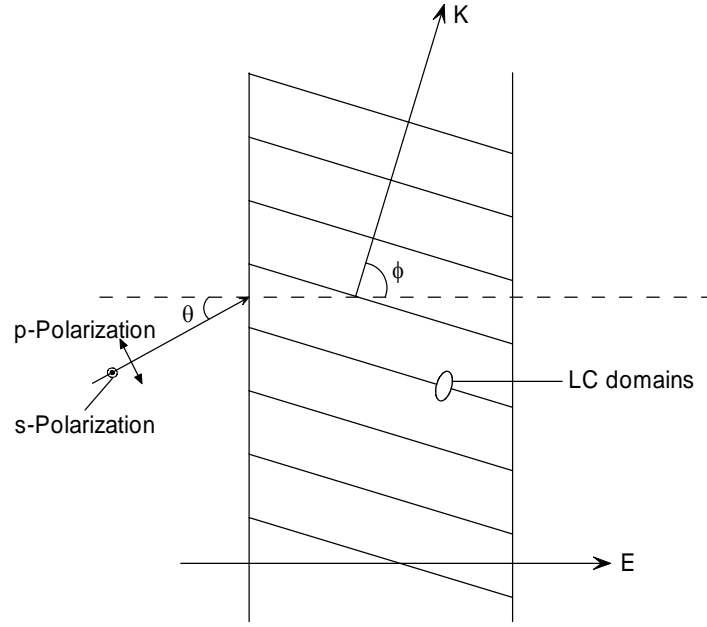
Figure 4.2 Geometry of H-PDLC grating.

According to the coupled wave theory,[26] and considering the scattering loss,[104] the diffraction efficiency can be written as,

$$\eta_j = \tau_{Tj} S_j S_j^*, \tag{4.12}$$

where τ_{Tj} is a scattering transmission factor and

$$S_j = v_j \frac{\sin\sqrt{v_j^2 - \xi_j^2}}{\sqrt{v_j^2 - \xi_j^2}}, \tag{4.13}$$

where v_j is the coupling strength, ξ_j is a complex detuning parameter which is related to scattering loss and dephasing caused by angular and spectral departures from the Bragg condition, and the subscript j ($j=s, p$) signifies the appropriate polarization.

For the case of an unslanted grating, the diffraction efficiency is solved numerically using Mathcad. Figure 4.3 gives four typical examples of diffraction efficiency as a function of the incident angle (also called angle sensitivity plots). We can see that with the increase of the index modulation (the refractive index difference between the LC-rich lamellae and the polymer-rich lamellae), the diffraction efficiency increases. Generally, to achieve a volume Bragg grating with high diffraction efficiency, a relatively large index modulation is needed.
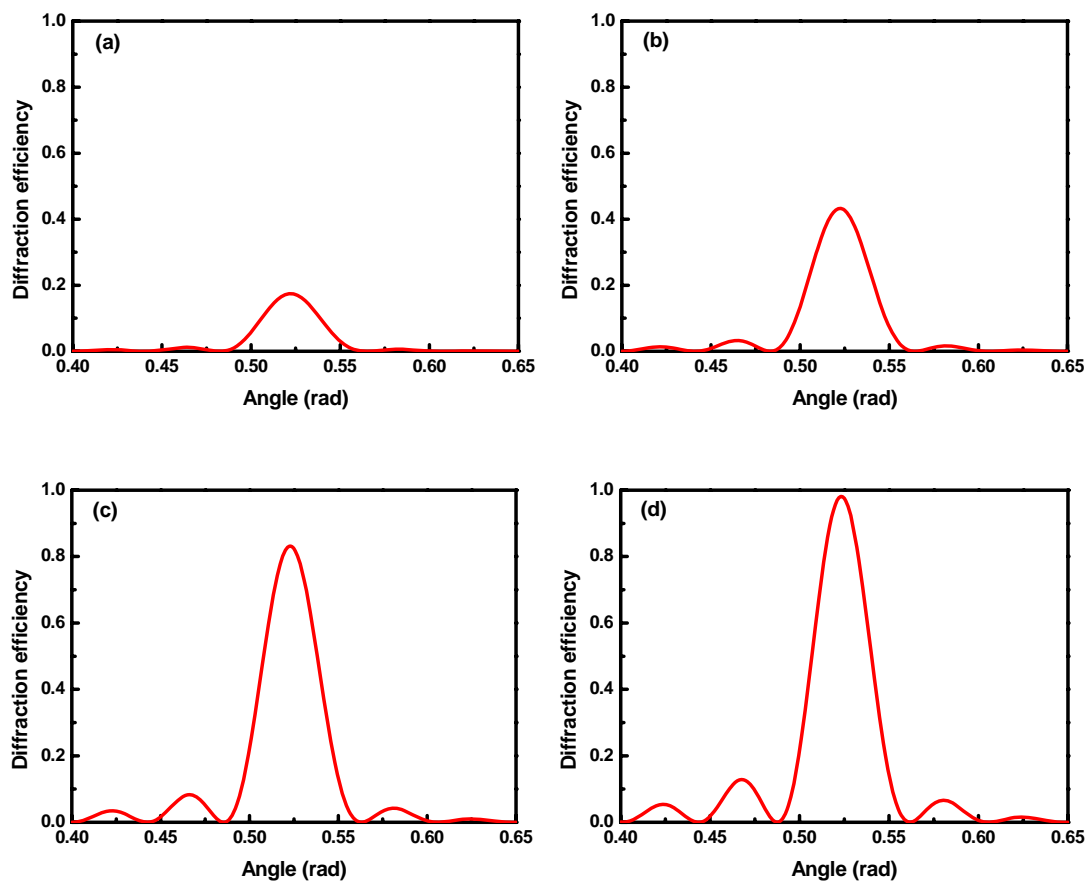
Figure 4.3. Angular dependence of diffraction efficiency for a transmission H-PDLC grating. Key parameters: $\theta_b=\pi/6$ (external), $\varphi=\pi/2$, $L=10$ μm, $\lambda_0=633$ nm, $a=0.020$, (a) $n_1=0.015$; (b) $n_1=0.025$; (c) $n_1=0.040$; (d) $n_1=0.050$.

However, it is worth noting that, for the H-PDLC transmission grating, it may be overmodulated in some cases. That is, the diffraction efficiency first passed through a maximum (generally less than 100%) and then decreased. An obvious feature of overmodulation in the angle sensitivity plot is the relatively large side slobes. Figure 4.4 shows both normal and overmodulated cases. We can see that the largest side lobe of the overmodulated grating is ~23%, whereas for the normal grating, the largest side lobe is ~10%. In addition, the angular bandwidth of overmodulated is slightly narrower than that of normal. This can be easily understood by the conservation of energy.
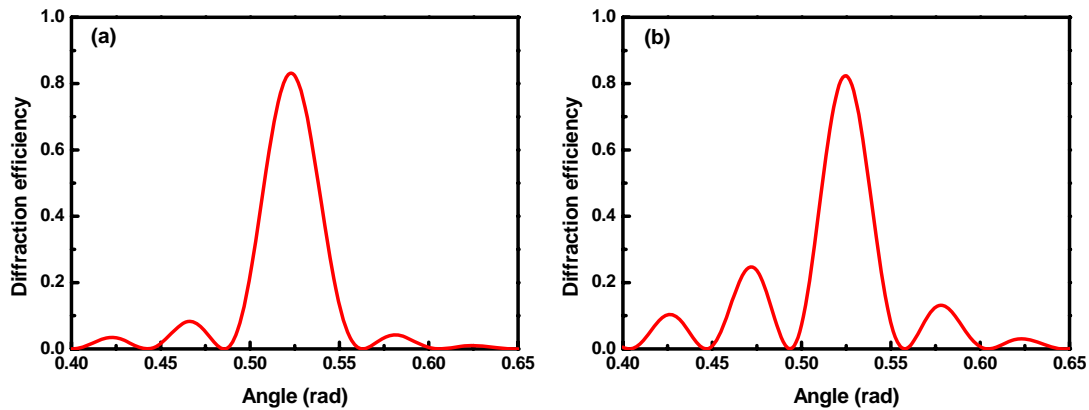
Figure 4.4. Angular dependence of diffraction efficiency for a transmission H-PDLC grating, illustrating (a) normal and (b) overmodulated cases. Key parameters: $\theta_b=\pi/6$ (external), $\varphi=\pi/2$, $L=10$ μm, $\lambda_0=633$ nm, $a=0.020$, (a) $n_1=0.040$; (b) $n_1=0.070$.

For the grating, the film thickness, L, and the index modulation amplitude, n_1, are reciprocal parameters, which determine the angular properties of the H-PDLC gratings. Generally, a small index modulation and a large thickness will produce a narrow angular sensitivity. The series of plots in Figure 4.5 show the predicted trend. Therefore, we can choose the parameters (i.e. film thickness and LC) according to the

application. For examples, for H-PDLC displays which need large view angles, a smaller thickness should be chosen.
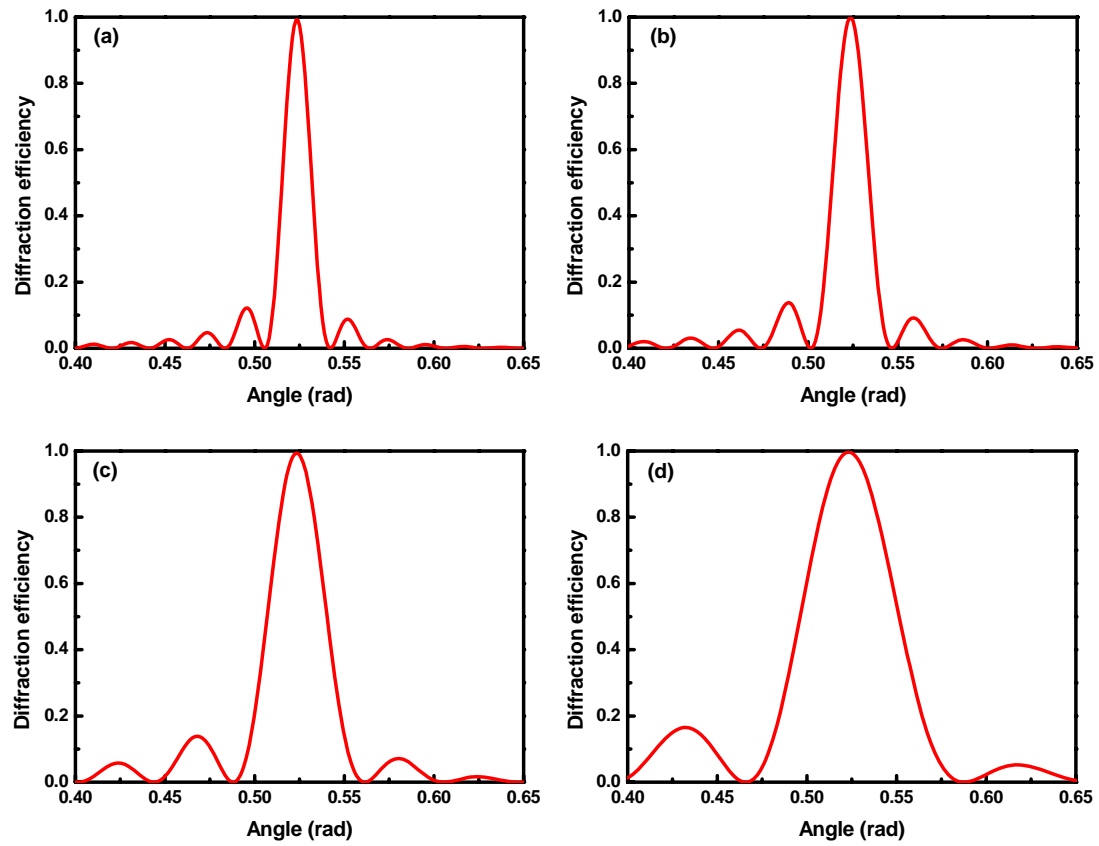
Figure 4.5. Angular dependence of diffraction efficiency for a transmission H-PDLC grating, illustrating angular bandwidth for various L and n_1. Key parameters: $\theta_b=\pi/6$ (external), $\varphi=\pi/2$, $\lambda_0=633$ nm, a=0.020, (a) L=20 μm, n_1=0.026; (b) L=16 μm, n_1=0.034; (c) L=10 μm, n_1=0.052; (d) L=6 μm, n_1=0.088.

Actually, scattering reduces the peak diffraction efficiency, preventing it from reaching its theoretical maximum of 100%. However, the droplet sizes in H-PDLC samples are ~20 nm on average, which are very small compared to the visible wavelength. So the scattering loss is relatively small, as indicated in Figure 4.6. In fact, larger scattering losses result from not only the phase-separated LC droplets but
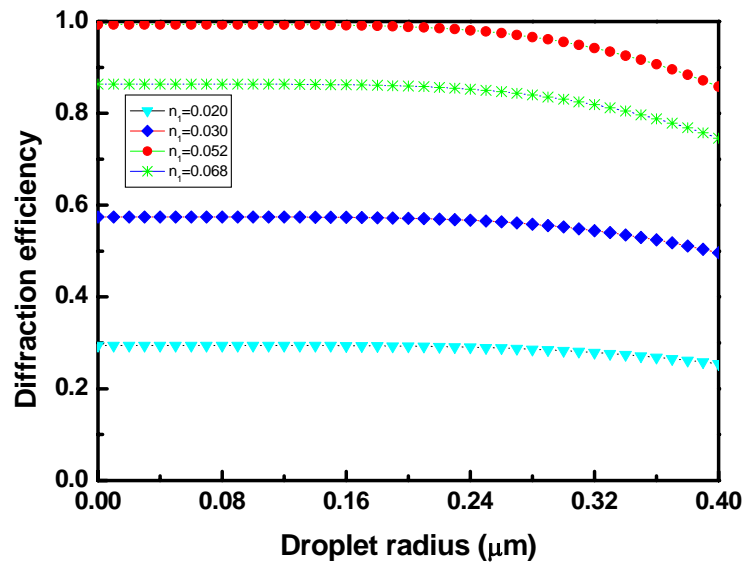
Figure 4.6 Peak diffraction efficiency of a transmission H-PDLC grating as a function of droplet radius a, illustrating the effects of scattering. Key parameters: $\theta_b=\pi/6$ (external), $\varphi=\pi/2$, L=10 μm, $\lambda_0=633$ nm.
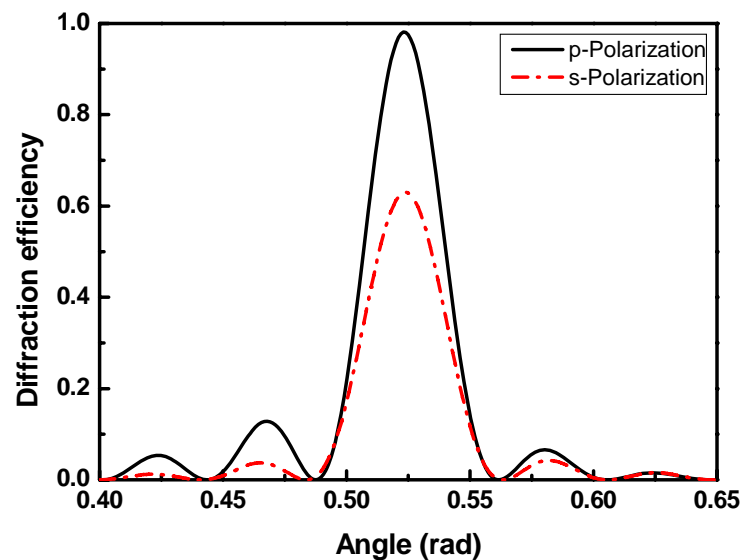
Figure 4.7 Angular dependence of a transmission H-PDLC grating, illustrating the dependence on polarization. Key parameters: $\theta_b=\pi/6$ (external), $\varphi=\pi/2$, L=10 μm, $\lambda_0=633$ nm, a=0.020, $n_1=0.050$ (p-polarization), $n_1=0.016$ (s-polarization).

also some other reasons such as the index mismatch at the interfaces and imperfection of the polymer film.

Generally, the diffraction efficiency of H-PDLC gratings has a polarization dependence because of the anisotropy of LC. Figure 4.7 illustrates this effect. In general, the *p*-polarization efficiency is always greater than the *s*-polarization one. In our experiment, we indeed observed this phenomenon. This is not favorable for some applications such as optical switching which needs to be polarization insensitive. It primarily results from the shrinkage of the polymer during the formation of gratings.

4.2 Optimization of H-PDLC Performance

Many researchers have explored different material recipes to achieve high diffraction efficiency, fast response time, and low drive voltage, which are discussed in section 3.2. In our research, we focused on the material recipe for visible (blue & green) curing, which is discussed in all the following parts of this thesis without special explanation. For this kind of material recipe, due to many different components for various purposes, the material recipe was optimized to achieve high performance according to the effect of monomer functionality,[44, 105] NVP concentrations,[106,107] LC concentrations,[40] and laser beam curing intensity.[108,109] In this section, we experimentally optimized the material recipe according to the refractive index match and investigated the effect on the driving voltage of different surfactants.

4.2.1 Selection of the Monomer and LC

In our configuration, the polymer refractive index, n_p, is chosen to be as close as possible to the ordinary refractive index, n_o, of LC. This helps to reduce the diffraction loss in the transparent state. Moreover, the birefringence of LC, Δn, is

chosen to be as large as possible in order to improve the diffraction efficiency. In our experiment, five kinds of acrylate monomers were selected and the values of the refractive index are 1.490 for Dipentaerythritol penta-/hexa-acrylate (No. 1), 1.484 for Pentaerythritol triacrylate (No. 2), 1.474 for Trimethylolpropane triacrylate (No. 3), 1.487 for Pentaerythritol tetraacrylate (No. 4) and 1.450 for Tri(propylene glycol) diacrylate (No. 5), respectively. The chemical structures of these five monomers are shown in Figure 4.8 and their corresponding functionalities are 5 - 6, 3, 3, 4, and 2, respectively. Because the prepolymer mixture includes other chemicals, such as photoinitiator, coinitiator, etc., and moreover, since the refractive index changes during polymerization, in general, the refractive index will be different from the above values for the mixture after polymerization. Two different LCs, E7 and BL038, were chosen to match the refractive index of polymer matrices and their physical properties are listed in Table 4.1.

Table 4.1 Basic physical properties of LC E7 and BL038.

Physical Properties		E7	BL038
Clearing Point (°C)		+58.0	+100.0
Flow Viscosity $(mm^2 s^{-1})$	20°C	39	72
	0°C	145	-
	-20°C	1200	-
	-30°C	6400	-
Optical Anisotropy +20°C, 589.3 nm	Δn	0.2253	0.2720
	n_e	1.7464	1.7990
	n_o	1.5211	1.5270
Dielectric Anisotropy +20°C, 1.0 kHz	$\Delta \varepsilon$	+13.8	+16.9
	$\varepsilon_\perp$	5.2	6.1
	$\varepsilon_\parallel$	19.0	23.0
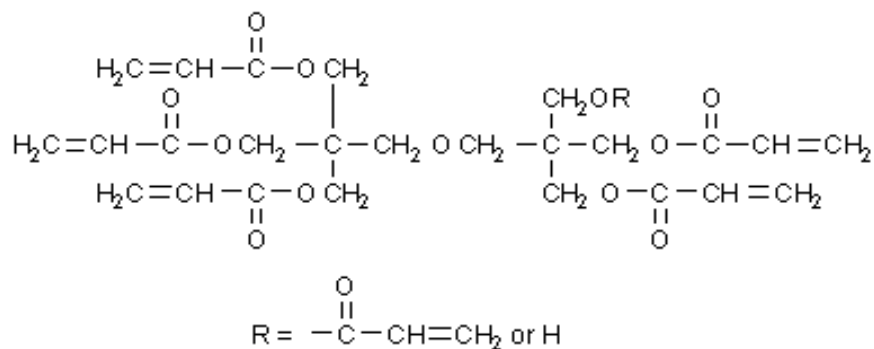
DPPHA (No. 1)
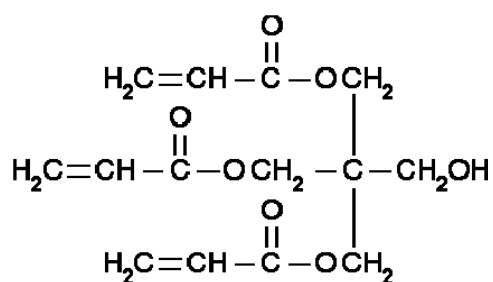
PETA (No. 2)
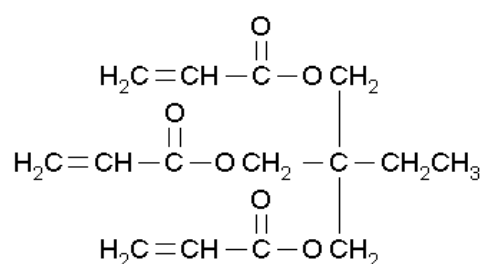
TMPTA (No. 3)
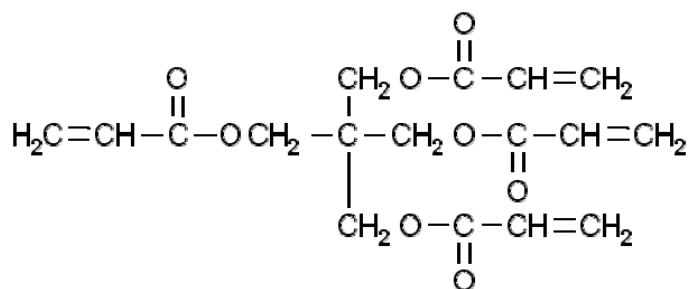
PET(etra)A (No. 4)
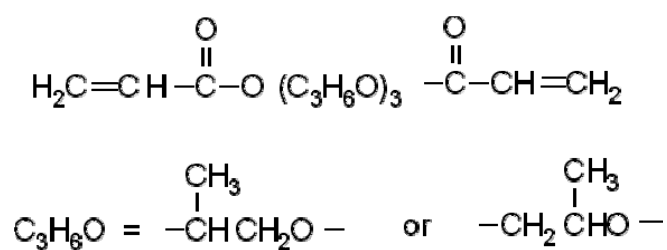
TPGDA (No. 5)

Figure 4.8 Chemical structures of the five momomers.

Table 4.2 Refractive index and corresponding diffraction efficiency (DE)

for various monomers used.

No.	1	2	3	4	5
Monomer	1.490	1.484	1.474	1.487	1.450
Prepolymer mixture	1.501	1.496	1.489	1.498	1.471
Cured film	1.529	1.528	1.522	1.530	1.502
DE for E7	41.2%	56.4%	65.0%	41.6%	32.2%
DE for BL038	61.8%	68.4%	40.2%	51.6%	34.2%
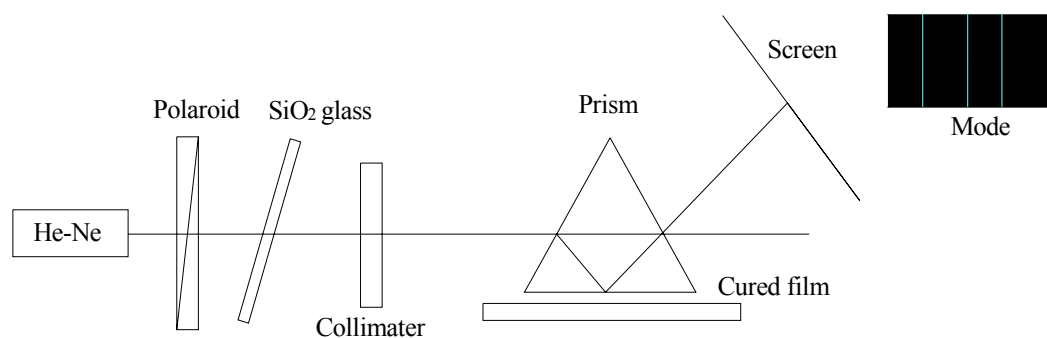
Figure 4.9 Measurement setup of the refractive index n_p.

The refractive indices of the monomers are from Sigma-Aldrich. Because the other chemicals are mixed into the monomer, the refractive index of the prepolymer mixture changes accordingly. The prepolymer mixture refractive indices were measured by an Abbe refracrometer. Then the mixture was cured on a SiO_2 substrate to form a polymer thin film, the refractive index, n_p, of which was measured by the m-line method.[110] Figure 4.9 shows the setup of refractive index measurement using the m-line method. The results are tabulated in Table 4.2. From the table, we can see that

the refractive index n_p of the cured film was larger than that of the corresponding monomer, with an increment of 0.03 - 0.05 on the average. In our experiment, the n_o of LC E7 is 1.521. The No. 3 monomer was the nearest to 1.521 and the experimental results proved that diffraction efficiency was the highest with the No. 3 monomer. Similarly, for BL038, the n_o is 1.527. The No. 2 monomer was the nearest to 1.528 and the experimental result proved that diffraction efficiency was the highest with the No. 2 monomer. According to our selection principle, the No. 3 and No. 2 monomers match with E7 and BL038 liquid crystals, respectively.

It is worth mentioning that because each kind of monomer has a different functionality, the mixture of different monomers with different functionalities can improve the morphology and performance of H-PDLC gratings. De Sarkar *et al.* reported that significant performance improvement could be obtained for prepolymers prepared with UV curable monomer mixtures with an average functionality ranging from 1.3 to 3.5.[44]

4.2.2 Surfactant Concentration Effect

For H-PDLC gratings, the LC droplets are small and the anchoring energy is high, which results in a high driving voltage. According to Mormile *et al.*, the threshold voltage of PDLC can be written as,[111]

$$V_{th} \approx \frac{d}{r}\left[\frac{K\left(\ell^2-1\right)}{\varepsilon_0 \Delta\varepsilon}\right]^{\frac{1}{2}}, \tag{4.14}$$

where d is the H-PDLC film thickness, r is the droplet radius, K is the effective elastic constant, ε_0 is the vacuum dielectric constant, $\Delta\varepsilon$ is the LC dielectric anisotropy, $\ell = a/b$ is the droplet aspect ratio, with a and b the length of the major and minor axis of the ellipsoid-shaped droplet, respectively. Eq. (4.14) was deduced by

balancing the elastic and field torques to the equilibrium orientation at the presence of a voltage applied to a shaped droplet,[34] i. e. $\Gamma_d + \Gamma_e = 0$, where Γ_d is the elastic torque per unit volume and Γ_e is the electric torque on the droplet director per unit volume. This can be regarded as the shape contribution to the threshold voltage of a normal PDLC.

The LC droplets of conventional PDLC are about 1~5 μm in size. However, the size of H-PDLC droplets is about 0.01~0.1 μm. The size effect on the threshold voltage can be understood by the following comparisons. Using our experimental parameters, $d = 20$ μm, $K = 1.71 \times 10^{-11}$ N, $\Delta\varepsilon = 6.49$, and assuming $\ell = 1.1$, for LC droplets with $r = 2$ μm and 0.02 μm, the corresponding threshold voltage V_{th} calculated is 2.5 V and 250 V respectively, which indicates $V_{th} \propto 1/r$. In general, the threshold voltage of nano-PDLC produced by holography is about one or two orders higher than that of normal PDLC.

For practical application of H-PDLC, it is desired to reduce the driving voltage. Colegrove *et al.* reported that by adding a high dielectric anisotropy material ($\Delta\varepsilon = 65$), the threshold voltage of H-PDLC can be reduced significantly.[93] In addition, adding a small portion of surfactant to the prepolymer/LC mixture also helps to reduce the threshold voltage.[95-97] When phase separation occurs in the homogenous mixture, the surfactant will form an intermediate layer between the polymer and the LC. The anchoring energy at the interface of the LC and the surfactant becomes weaker than that at the interface of the LC and polymer without surfactant. This decrease in anchoring strength may effectively lower the driving voltage.

In our experiments, three different kinds of surfactants, Octanoic Acid, #1, S-271 POE sorbitan monooleate, #2, and Tergital Min-Foam 1X, #3 were used for comparison. Figure 4.10 shows the diffraction efficiency as a function of driving electric
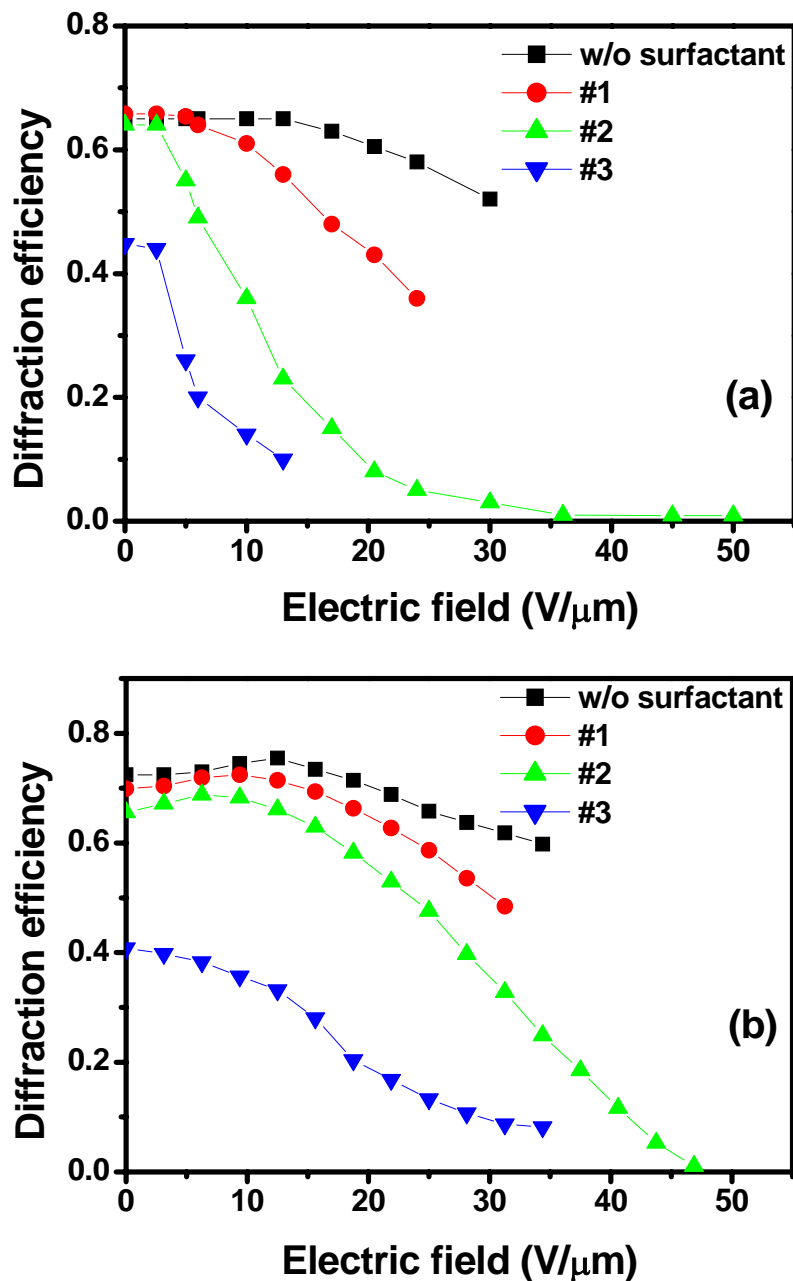
Figure 4.10 Diffraction efficiency versus the electric field curves for Bragg gratings made of E7 (a) and BL038 (b) liquid crystals with three different kinds of surfactants. The diffraction efficiency without surfactant is also shown for comparison. The monomers used are No. 3 and No. 2 (Table 1) for E7 and BL038 respectively.

field for three different surfactants. The H-PDLC without surfactant is also shown for comparison. For all samples in Figure 4.10, the concentration of the surfactants was 8

wt%. It can be seen from Figure 4.10 that, the surfactant is effective in reducing the driving voltage. The conductivity of samples with surfactants #1 and #3 was so high that the voltage could not be increased to the point where they were completely switched. Sample #2 can both keep the high diffraction efficiency and reduce the driving voltage effectively. Comparing these four curves in Figure 4.10, surfactant #2 is the best. It reduces the threshold voltage from 13 V/μm to about 2.5 V/μm. Comparing Figure 4.10(a) and (b), we can see that the samples made of BL038 LC have a higher switching voltage than those made of E7 LC. This was because BL038 has a larger viscosity coefficient than E7; the flow viscosity of BL038 and E7 is 72 mm^2/s and 39 mm^2/s at 20°C, respectively. Thus, the selection of LC should be considered from its physical properties, especially viscosity.
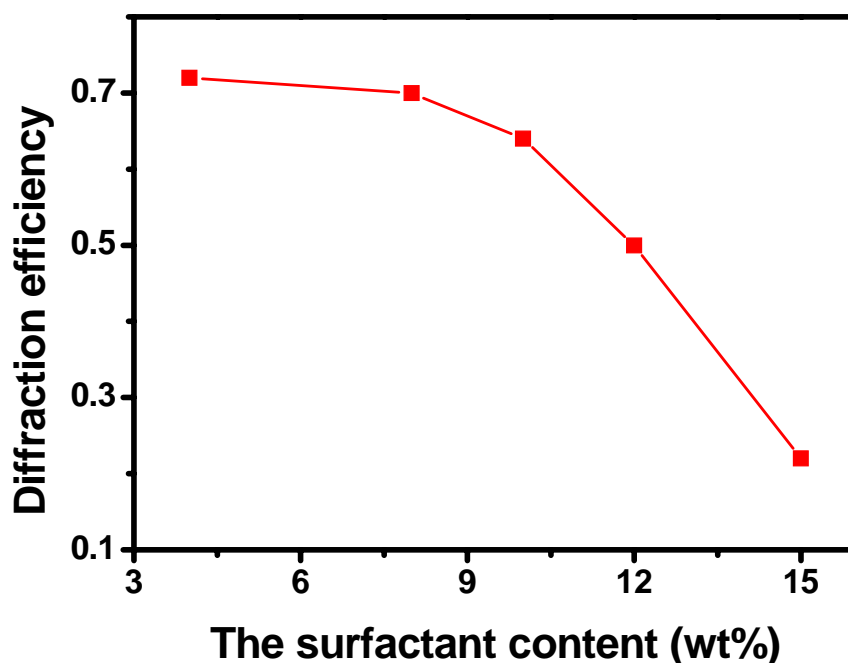
Figure 4.11 Diffraction efficiency as a function of the surfactant content for surfactant #2. The monomer and liquid crystal used are No. 3 (Table 4.2) and E7 respectively.

Figure 4.11 shows the diffraction efficiency as a function of the surfactant content for samples containing #2 surfactant. With an increase in concentration, the diffraction efficiency decreases. Generally, when the surfactant concentration was less than 8 wt%, the H-PDLC Bragg gratings kept their higher diffraction efficiency.
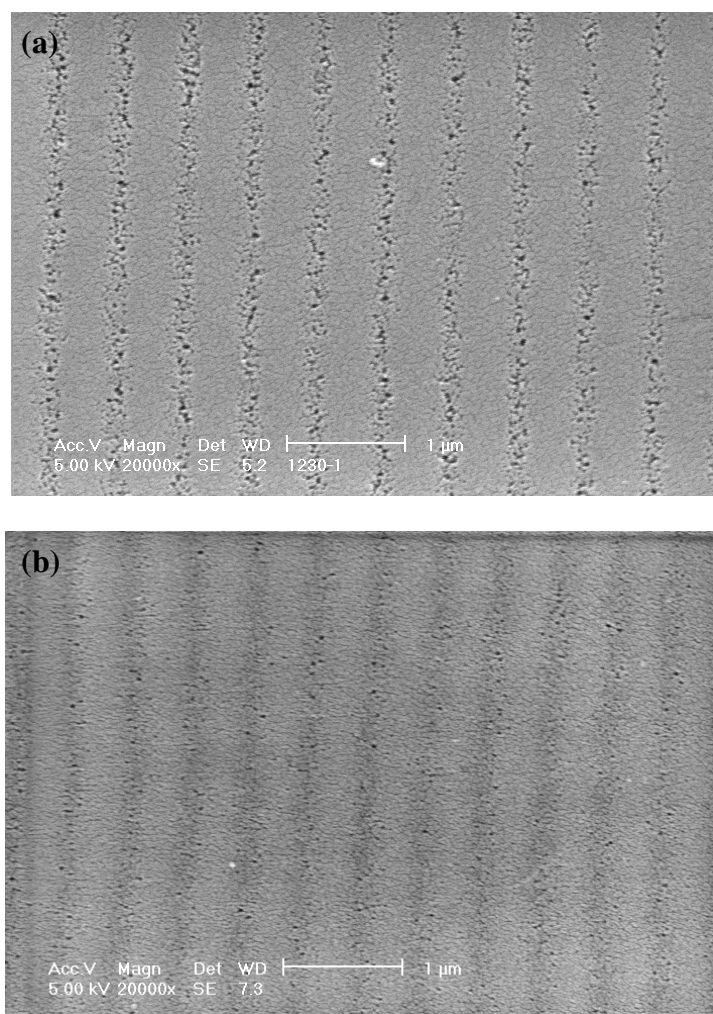
Figure 4.12 SEM images of the H-PDLC Bragg gratings consisting 8 wt% (a) and 15 wt% (b) of surfactant #2. The monomer and liquid crystal used are No. 3 (Table 4.2) and E7 respectively.

Figure 4.12(a) and (b) show the SEM morphologies of the H-PDLC gratings, which contain 8 wt% and 15 wt% of surfactant respectively. From Figure 4.12, it can be seen that the surfactant affects the grating significantly. With more surfactant, the

polymer regions contain more LC droplets, and the grating structures become blur. In addition, the LC droplets become smaller with more surfactant added. Thus the surfactant affects the LC movement during polymerization. Figure 4.12(a) has a clearer grating structure than Figure 4.12(b), which indicates that the grating in Figure 4.12(a) has better diffraction properties. In our experiment, when the surfactant content was around 8 wt%, the H-PDLC Bragg gratings could both keep high diffraction efficiency and have excellent electro-optical properties.

4.3   2×2 Optical Switch

With the optimized material recipe, H-PDLC transmission gratings were fabricated. Such a transmission grating is a 2×2 optical switch. In this section, we measured the performance of the optical switch. The ratio of TMPTA/NVP/S-271/NPG/RB was 62/25/10/2/1 by weight. The liquid crystal used was E7 from Merck. The cell thickness was 18 μm and the grating spacing was 0.56 μm.

4.3.1 Operation Mechanism
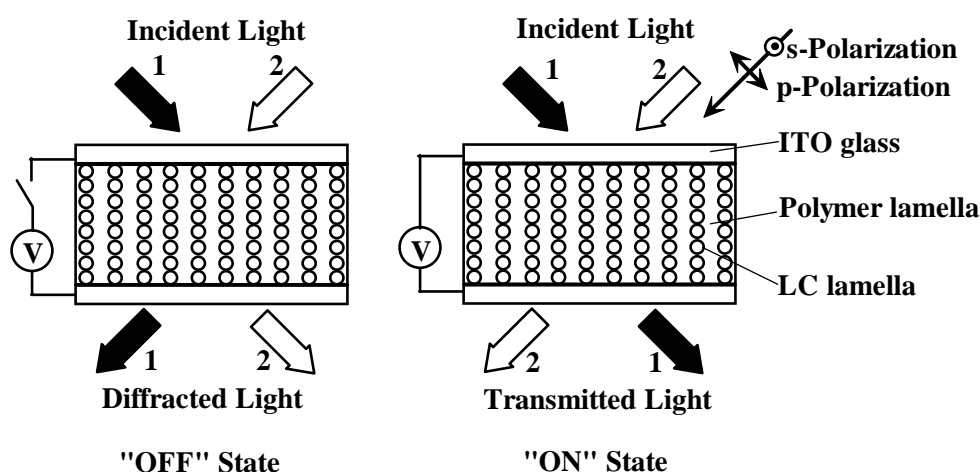
Figure 4.13 Schematic of the LC-polymer composite 2 × 2 optical switch. The p- and s-polarization are also sketched.

64

The structure of the 2×2 optical switch is sketched in Figure 4.13. By applying a proper electric field, the grating can be switched between ON and OFF states. The working principle of such a switch is fairly straightforward. A linearly polarized light beam incident on the switch will see the phase grating formed by the LC-polymer materials with different refractive index, and thus be diffracted. When an electric field is applied, the LC molecular director is reoriented, changing the refractive index seen by the incoming light. If properly designed, with a suitable voltage applied, $n_{LC} = n_{polymer}$ can be achieved, and the Bragg grating disappears. If and when the condition is met, the beam is no more diffracted.

4.3.2 Electro-optical Characteristics

The contrast ratio (*CR*) and signal-noise ratio (*SNR*) of the switch can be defined as

$$CR = 10\,log(\frac{DE_{max}}{DE_{min}}) \text{ or } CR = 10\,log(\frac{TE_{max}}{TE_{min}}) \qquad \textbf{(4.15)}$$

$$SNR = 10\,log(\frac{DE_{max}}{TE_{min}}) \text{ or } SNR = 10\,log(\frac{TE_{max}}{DE_{min}}) \qquad \textbf{(4.16)}$$

where DE_{max} is the highest diffraction efficiency, DE_{min} is the lowest diffraction efficiency, TE_{max} is the highest transmission efficiency, and TE_{min} is the lowest transmission efficiency.

Figure 4.14 shows the diffraction efficiency and transmission efficiency as a function of the applied electric field. With an optimized ratio of various materials, the highest diffraction efficiency achieved was 85.7%. The corresponding CR and SNR were about 23.4 dB and 15.1 dB, respectively. In Figure 4.14, the sum of the diffraction efficiency and transmission efficiency is also plotted. It can be seen that, the sum increases slightly with the electric field, which indicates a decrease in the

random scattering. When the diffraction efficiency is reduced to the minimum, the transmission efficiency reaches the maximum.
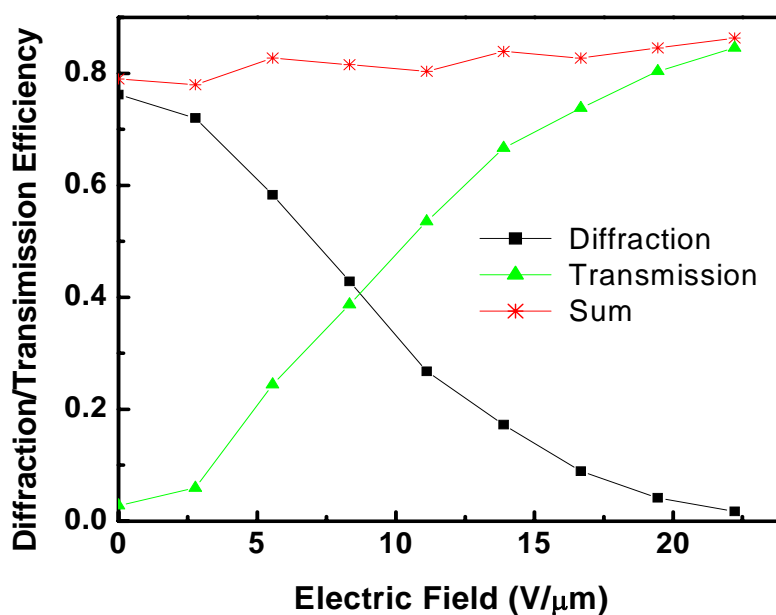
Figure 4.14 Diffraction and transmission efficiency as a function of applied electric field. The sum refers to the sum of diffraction and transmission efficiencies.
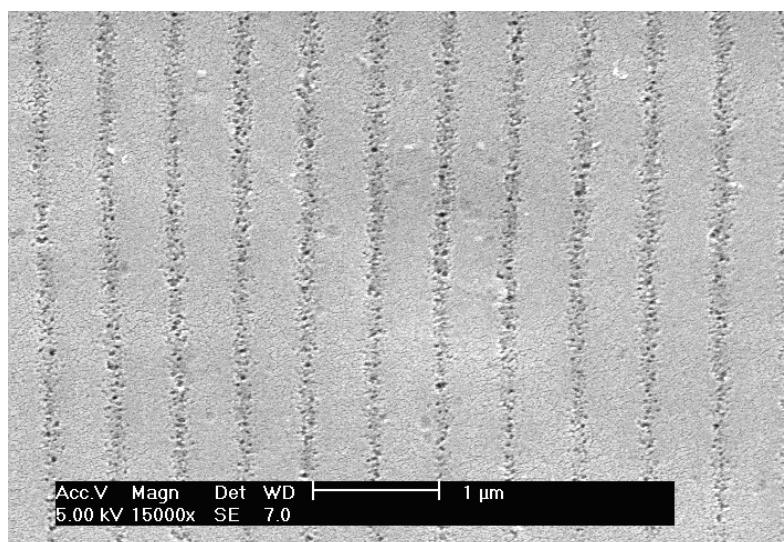
Figure 4.15 SEM image of the grating with LC removed. The dark region is the vacancy of the liquid crystal droplets after the liquid crystal is removed and the bright region is the polymer-rich lamellae.

Figure 4.15 shows SEM image of the grating with the LC cell de-capped and LC removed. It can be seen from Figure 4.15 that, the pitch of the grating is about 0.56 µm. Judging from the small holes (in narrower darker regions separating wider brighter stripes), where the LC droplet resides, the size of most LC droplets is in the range from 10 to 50 nm in diameter.

4.3.3 Response Time
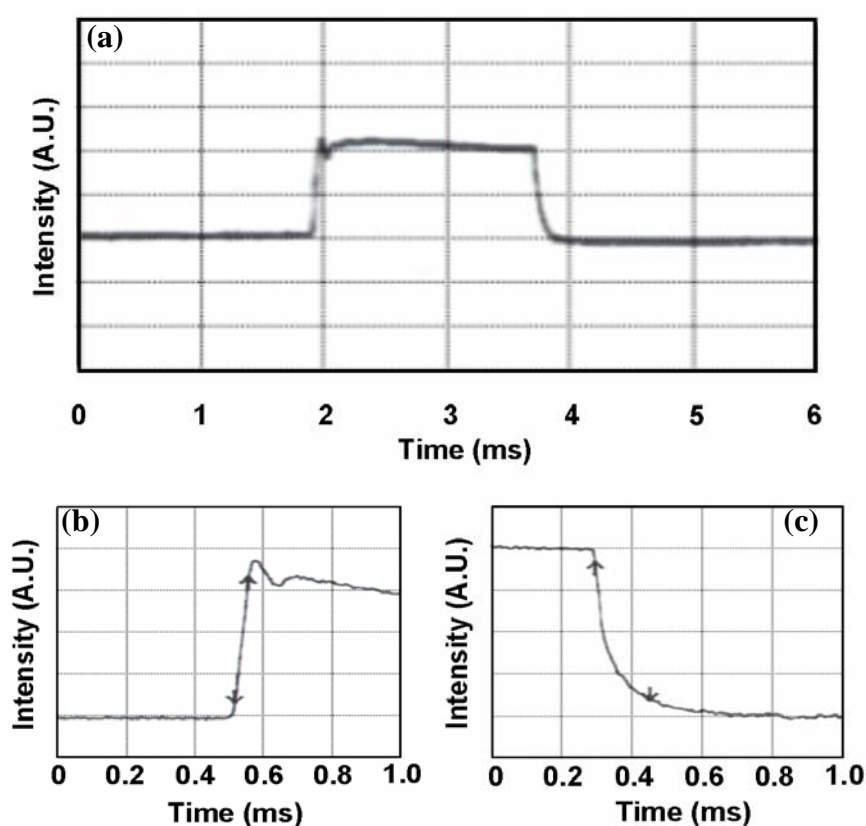
Figure 4.16 Variation of diffracted light intensity corresponding to a square driving voltage (a), and the magnified rising edge (b) and the falling edge (c) of (a).

Driven by square wave signals, the rise and decay times were measured. Figure 4.16(a) shows the diffracted light intensity when the cell was driven by a 1.75 ms voltage pulse. Figure 4.16(b) and (c) show the rising edge and falling edge of the

detected signal respectively. The rise time (10% to 90% intensity change) and the decay time (90% to 10% intensity change), are 36 μs and 160 μs, respectively. The response time is faster than other optical switches, such as thermo-optical switches, whose response time is usually on the order of a millisecond.[112] However, a drawback of the LC-polymer composite optical switch is that, a high driving voltage is generally needed. In our experiment, the threshold electric field for the samples without surfactant was as high as 13 V/μm, which resulted in a threshold voltage of 234 V for an 18 μm cell. To lower the driving voltage, a small portion of surfactant, S-271 POE sorbitan monooleate, was added in the composite. After adding the surfactant, the threshold electric field was significantly reduced to about 2.5V/μm, which was more than four times smaller than that without surfactant. This result agrees with the previous report by Yuan *et al.*.[55] It is worth mentioning that, besides adding surfactant, a high dielectric anisotropy material can also be added into the LC-polymer composite to reduce the driving voltage.[93] Another interesting thing to note is that, in Figure 4.16(b), an optical bounce is clearly observed immediately after the electric field is applied. It is probably due to the backflow effect of liquid crystals.[113,114] Backflow effect is a consequence of flow close to the LC cell walls induced by the rapidly relaxing alignment following the removal of the electric field, which generally exists in the TN cells. This flow essentially creates a shear flow in the center of the cell, which causes a temporary reversal of the relaxation in that region, before the alignment finally relaxes as one anticipates. As a result, an optical bounce in transmission curve is experimentally observed when the light is normally incident on the cell, which is induced by the backflow effect. In our experiments, this phenomenon was only observed at the edge of "ON" state. We speculate the reason as follows. In H-PDLCs, the nematic configurations in most LC droplets are generally

bipolar, as shown in Figure 2.9(a). When an external electric field is applied on H-PDLCs, the nematic director realigns along the electric field direction. At the same time, an internal electric field is induced due to the impurities (mobile ions) in H-PDLCs, which thus decreases the external electric field. Then due to the balance between the elastic torque and the electric torque in the LC droplets, and the delay between the external electric field and the induced ion field, an optical bounce in transmission curve was observed at the edge of "ON" state. After the removal of the external electric field, the nematic director configurations gradually revert to the original status due to the elastic torque, where the optical bounce would be difficult to be observed at the edge of "OFF" state.

4.3.4 Polarization Dependence

For LC-polymer composite optical switchs, polarization-dependent loss (PDL) is a big concern. Generally, the conversion of the monomer molecules into a polymer network is accompanied with a closer packing of molecules, which leads to contraction of the composite known as polymerization shrinkage. When the polymer shrinks, the LC droplets are compressed, which preferentially aligns the symmetry axis of the rod-shape LC molecules in the droplet along a common direction. This results in a polarization sensitive diffraction since the optical axis is on average along the same direction for all droplets, therefore making diffraction efficiency sensitive to the input polarization. However, in our experiment, the shrinkage was only about 2% which is significantly smaller than the reported data, which are usually 5% ~ 10%.[20,115] The smaller polymerization shrinkage reduces the PDL remarkably. The main reason for the lower shrinkage in our experiment is that, smaller exposure intensity and longer exposure time were used to decrease the shearing strength in the polymerization process.
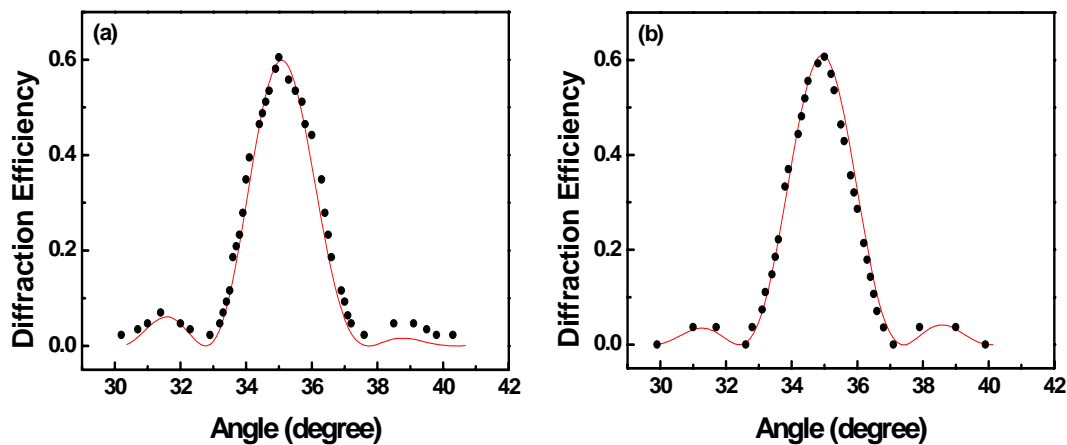
Figure 4.17 Diffraction efficiency as a function of incident angle for p-

(a) and s-polarized (b) light.
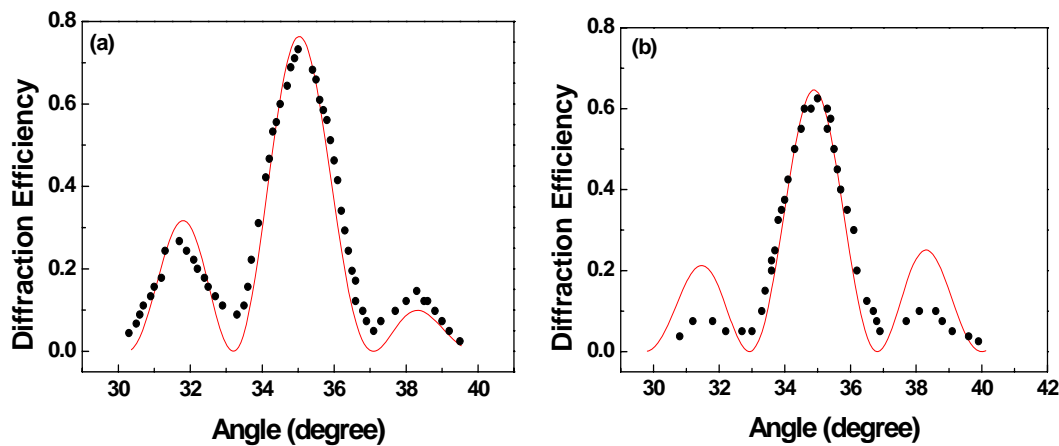
Figure 4.18 Diffraction efficiency as a function of incident angle for p-

(a) and s-polarized (b) light. High side lobes indicate overmodulation.

Figure 4.17(a) and (b) show the diffraction efficiencies measured for *p*- and *s*-polarized light, respectively, with a wavelength of 632.8 nm. Using the diffraction efficiency obtained in Figure 4.17(a) and (b), the PDL was calculated to be 0.03 dB, by comparing the insertion loss difference between *p*- and *s*-polarized light. It is worth mentioning that, Karasawa *et al.* have reported that diffraction efficiency for *p*-polarization is much higher than that for *s*-polarization in acrylate systems,[116] similar to that in Figure 4.18, which is also found in our experiments.Figure 4.18 shows the

diffraction efficiency for the sample fabricated with a larger exposure intensity of 30 mW/cm^2. From Figure 4.18(a), it can be seen that, for the *p*-polarization case, the left side lobe is larger than the right one, which is more than 20%. This is called overmoduation. The main reason for that is the large shrinkage caused by intense exposure which makes the liquid crystal preferably align along one direction. From Figure 4.17 and Figure 4.18, the angular bandwidth (full width at half maximum) is approximately 2°. According to Kogelnik's coupled-wave theory,[26] with increased thickness of LC-polymer composite films, the bandwidth will become narrower.

4.4　Summary

In this chapter, we first theoretically investigated the factors which affect the diffraction efficiency of the H-PDLC Bragg gratings. Then, we experimentally optimized the material recipe basing on our previous experience, and investigated the effect of the surfactants on the electro-optical properties. With the optimized material recipe, a polarization insensitive 2×2 optical switch was fabricated and characterized. Such optical switch shows potential to be used in optical communication systems although it has not characterized in the infrared range.

CHAPTER 5   Patterned PDLC Devices

A unique advantage of PDLC materials is that the PDLC materials can perfectly copy the spatial intensity distribution of light. At the high intensity area, the monomer can be polymerized due to the absorption of the light. Therefore, at the high intensity area, the polymer will dominate, while at the low intensity area, LC will dominate. As a result, different phase differences will be obtained when the light passes through. Making use of this property, we can design and fabricate different phase elements using PDLC materials. In this chapter, two different PDLC devices were designed, fabricated, and tested.

5.1   Tunable Fly's-Eye Lens

5.1.1 Motivation

Irradiance uniformity is a prerequisite in many optical projection systems. Light sources rarely produce the required uniformity themselves for most simple illumination systems. Therefore, some modification of the irradiance pattern produced by the light source is a necessity. The optical systems used to accomplish this goal generally use some type of flux integration scheme. Rod integrators and fly's-eye integrator arrays are typically employed to convert the bulb filament - a point or tiny line - into homogeneous illumination over the liquid crystal display (LCD).[117-121] However, the rod-type integrators are physically long and heavy, and optically slow, which is fundamentally incompatible with today's trend toward smaller, lighter projectors. Fly's-eye integrators are more compatible with this trend. A typical characteristic of such high throughput integrators is that they can produce a discontinuous pupil irradiance distribution and a condenser lens is used to make the

72

pupil irradiance optically overlapping at the illumination plane to achieve uniform light from a nonuniform source. Traditionally, fly's-eye integrators have been made from molded glass. Glass is popular because it has good temperature resistance and mechanical properties, and its performance is well understood.

Polymer fly's-eye lens integrators are also available, and have been included in numerous front and rear LCD projector applications.[122] These lenses have been fabricated from acrylic (PMMA), polycarbonate (PC), and various high temperature thermoplastics with a high precision molding process.[123] The potential advantages of a plastic light integrator as compared to glass are its lighter weight, lower cost, and better performance (higher transmissivity and overall uniformity). However, the resistance of plastic to continuous, high operating temperatures and the birefringence in plastic parts are still key concerns. These problems limit their applications to a great extent.

PDLC has been studied for about twenty years since it was first reported by Doane and his co-workers.[8] It holds promise for many applications ranging from switchable windows to optical devices. The combination with holography makes holographic polymer dispersed liquid crystal (H-PDLC) more useful in optical communications, [124, 125] information storage,[60] integrated optics and flat panel displays.[55, 126] The most interesting thing in PDLCs and H-PDLCs is that liquid crystals exist in the form of droplets, and the liquid crystal director can be reorientated by applying a voltage. The refractive index difference between liquid crystal droplets and polymer matrix can change the phase of the incoming light and cause the light being scattered or transmitted in PDLCs and diffracted or transmitted in H-PDLCs. Based on this concept and laser patterning technique, a fly's-eye lens was fabricated with PDLC materials. Its forming process has been simulated based on a patterned

photopolymerization technique in which the spatially modulated photoreaction rate is coupled with the time dependent Ginzburg-Landau (TDGL) equations (model C) by incorporating free energy densities of isotropic mixing, nematic ordering, and network elasticity. The simulated morphologies were very similar to what we obtained experimentally. Its optical properties were examined and the results showed that PDLC fly's-eye lenses could be a potential alternative to conventional glass fly's-eye lenses.

5.1.2 Fabrication

Figure 5.1 shows the experimental setup to fabricate the fly's-eye lens. The key element is a fly's-eye lens mask (LIMO, Germany), which produces a periodic dot array pattern at the focal plane. This pattern is then minimized using a large aperture lens, which has an effective focal length of 150 mm. The minimized pattern is about 0.7 cm^2 at the focal plane of the lens. The LC cell filled with the prepolymer/LC mixture is placed at the focal plane of L_3 to record this pattern. During exposure, in the area with higher exposure intensity, absorption by the photoinitiator results in a highly reactive triplet state. The coinitiator undergoes an electron-transfer reaction with this triplet state to create a free radical. Free-radical polymerization is then initiated. Hence, spatial gradients in the chemical potential are established which produces a diffusion of monomers (and other reactants) into the bright regions, and a counter-diffusion of LC into the dark regions. This process continues until a new equilibrium chemical potential is established. Thus, a phase type fly's-eye lens with periodic gradient refractive index is formed in PDLCs. When a voltage is applied to the cell, the liquid crystal molecules reorientate along the direction of the electric field. If the refractive indices of polymer matrix and liquid crystal are matched, the light beam will pass through directly as if it is a homogeneous film. So the laser beam

can be switched from a uniform to a Gaussian distribution. This may be useful in beam shaping and also potentially useful in many illumination systems that require uniform beam profile.
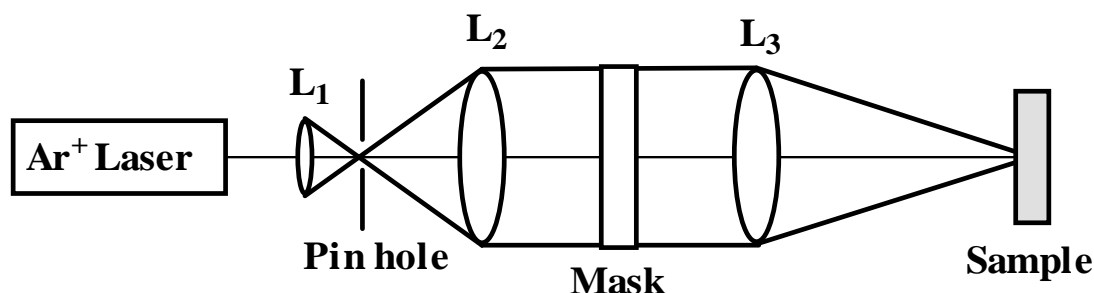
Figure 5.1 Experimental setup to fabricate fly's-eye lens. L_1, L_2 and L_3 are all lenses. L_1 and L_2 are used to generate a collimated laser beam. L_3 is used to minimize the pattern.

In this experiment, the materials used to fabricate the fly's-eye lens were TMPTA, NVP, RB, and NPG. The ratio of TMPTA/NVP/NPG/RB was 62/25/2/1 by weight.[35] The liquid crystal used was E7. The prepolymer and LC were mechanically blended according to the appropriate weight ratio at 65 °C (higher than the clearing point of the LC E7) to form a homogeneous mixture under dark conditions. In this prepolymer/LC mixture, the liquid crystal concentration was about 35 wt%. A droplet of the mixture was sandwiched between two pieces of ITO coated glass. The cell gap was about 30 μm. The curing intensity before the photomask was 12 mW/cm^2 and the exposure time was 120 s. After exposure, the samples were further cured for 5 mins using a UV lamp to ensure the complete polymerization of the prepolymer. All samples were measured with a 543 nm He-Ne laser at room temperature. For morphology analysis under an optical microscope, the test samples were broken with the ITO glass on one side removed, soaked in ethanol for more than 12 hrs to remove LC, and finally dried.

5.1.3 Simulation

The photopatterning process of the PDLC fly's-eye lens may be modeled by mimicking spatiotemporal growth of concentration and orientation order parameters of the LC in which a photoreaction rate equation is coupled with the TDGL model C, as described below:[127-130]

$$\frac{\partial \phi_M}{\partial t} = \nabla \bullet \left[\Lambda \nabla \frac{\partial G}{\partial \phi_M} \right] + \eta_{\phi_M} \text{ or}$$

$$\frac{\partial \phi_P}{\partial t} = \nabla \bullet \left[\Lambda \nabla \frac{\partial G}{\partial \phi_P} \right] + \eta_{\phi_P}$$

(5.1)

$$\frac{\partial \phi_L}{\partial t} = \nabla \bullet \left[\Lambda \nabla \frac{\partial G}{\partial \phi_L} \right] + \eta_{\phi_L}$$

(5.2)

$$\frac{\partial S}{\partial t} = \nabla \bullet \left[\Lambda \nabla \frac{\partial G}{\partial S} \right] + \eta_{\phi_S},$$

(5.3)

where $\phi_L(r,t)$ is the conserved concentration (volume fraction) order parameter of LC at position r and time t, and where $S(r,t)$ is the nonconserved orientational order parameter. The noise terms, $\eta_{\phi_P}(r,t)$ and $\eta_{\phi_L}(r,t)$, represent the concentration fluctuations of polymer and LC, respectively, and $\eta_{\phi_S}(r,t)$ signifies the orientation fluctuations of the LC directors that satisfy the fluctuation dissipation theorem.

Furthermore, the monomer, $\phi_M(r,t)$, and polymer, $\phi_P(r,t)$, concentration are related to $\phi_L(r,t)$ via the fractional conversion, α, viz. $\phi_M = (1 - \alpha)(1 - \phi_L)$ and $\phi_P = \alpha (1 - \phi_L)$, respectively. Since the photopolymerization rate, $d\alpha/dt$, is proportional to the square root of the exposure intensity, I_0, it may be represented in the periodic form:

$$\frac{d\alpha}{dt} = k_0 I_0^{1/2} \left[\cos\left(\frac{N_x \pi}{L} x \right) + \cos\left(\frac{N_y \pi}{L} y \right) \right] (1 - \alpha),$$

(5.4)

where k_0 is the reaction rate constant. N_x and N_y represent the number of layers,

76

related to the interference angles or periodicity in the horizontal and vertical directions, respectively. *L* is the size of an assumed square grid.

G is the total free energy of the system, which may be written as

$$G = \int_V [g(\phi_L, \phi_M, \phi_P, S) + \kappa_\phi |\nabla \phi_L|^2 + \kappa_S |\nabla S|^2] dV ,\qquad (5.5)$$

where $g(\phi_L, \phi_M, \phi_P, S)$ or g for brevity is the local free energy density of the system. The terms $\kappa_\phi |\nabla \phi_L|^2$ and $\kappa_S |\nabla S|^2$ are nonlocal terms associated with the gradients of the LC concentration and orientation fluctuations, respectively. κ_ϕ and κ_S are the corresponding interface gradient coefficients.

The local free energy density, *g*, can be expressed as the sum of the isotropic mixing (g^i), nematic ordering (g^n), and elastic (g^e) free energy densities.

$$g^i = \phi_L \ln \phi_L + \phi_M \ln \phi_M + \chi(\phi_L \phi_M + \phi_L \phi_P) ,\qquad (5.6)$$

where χ is an interaction parameter for LC and monomer, and LC and polymer, which are assumed to be equal.

$$g^n = \frac{1}{r_L}(-\phi_L \ln z + \frac{1}{2}v\phi_L^2 S^2)\qquad (5.7)$$

$$z = \int_0^1 \exp\left[\frac{v\varphi_L S}{2}(3x^2 - 1)\right] dx\qquad (5.8)$$

$$S = \frac{3}{2z}\left\{\int_0^1 x^2 \exp\left[\frac{v\varphi_L S}{2}(3x^2 - 1)\right] dx - \frac{1}{2}\right\},\qquad (5.9)$$

where *z* is the normalized partition function, *S* is the orientational order parameter, *x* = $\cos\theta$ and θ is the angle between the LC directors and the *z* axis, v is the Maier-Saupe interaction parameter, which is related to the nematic-isotropic transition temperature, T_{NI}.

$$g^e = \frac{3\alpha_e}{2r_c} \Phi_0^{2/3} (\phi_P^{1/3} - \phi_P) + \frac{\beta_e}{r_c} \phi_P \ln \phi_P \qquad \textbf{(5.10)}$$

$$r_c = \frac{\alpha}{2 - \alpha - 2\sqrt{1-\alpha}} \qquad \textbf{(5.11)}$$

where r_c is the segment length between cross-linked points, and α_e and β_e are network model constants.
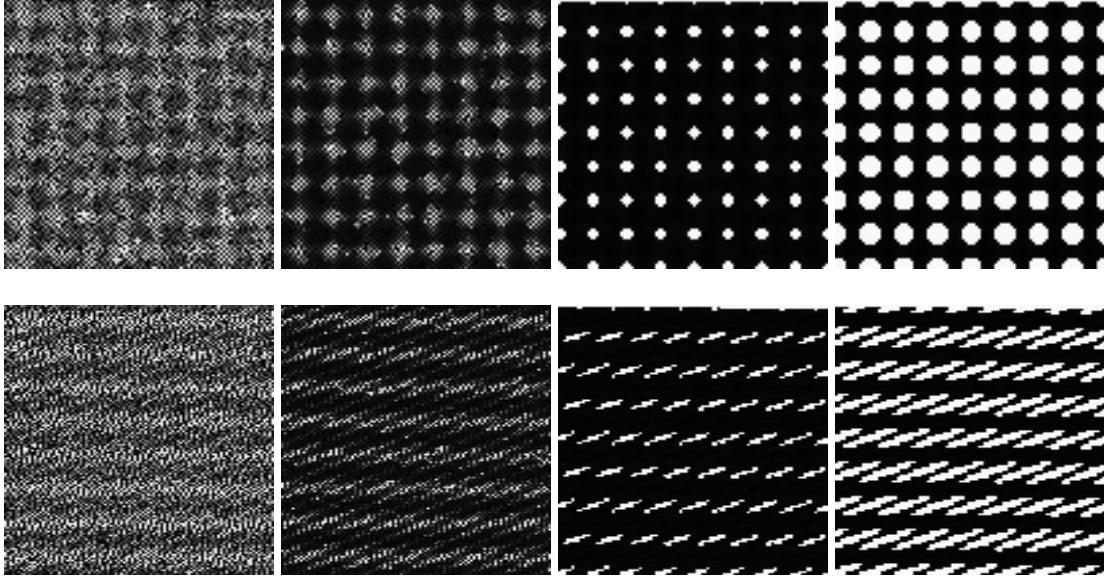
Figure 5.2 Evolution of a hypothetical patterned PDLC fly's-eye lens showing the array patterns. Parameters used were: $\phi_L = 0.75$, $T = 30°C$, $k_0 = 10^{-4}$, $I_0 = 1.0$. The upper row shows the case when $N_x = N_y = 100$, while the lower row represents those when $N_x = 100$ and $N_y = 150$.

It can be anticipated that polymerization occurs preferentially in the high-intensity regions due to the fast photoreaction rate that makes LC molecules diffuse into the low-intensity regions and form droplets. Figure 5.2 demonstrates the time sequence of the spatiotemporal development of microlens arrays calculated using the parameters: $\phi_L = 0.75$, $T = 30°C$, $k_0 = 10^{-4}$, $I_0 = 1.0$. The upper row shows the

78

emerging patterns in the compositional order parameter field when $N_x = N_y = 100$, while the lower row represents those when $N_x = 100$, and $N_y = 150$. In the simulation, one can envisage the emergence of microlenses with varying shapes, viz., spherical or elliptical as depicted in Figure 5.2. As seen in the upper row figure, the light pattern gives rise to the array of spherical microlens when $N_x = N_y$. However, when $N_x \neq N_y$, the elliptical microlens arrays (lower row) may be obtained. Therefore, microlenses with different shapes was obtained by controlling the light pattern, i.e. Eq. (5.4).
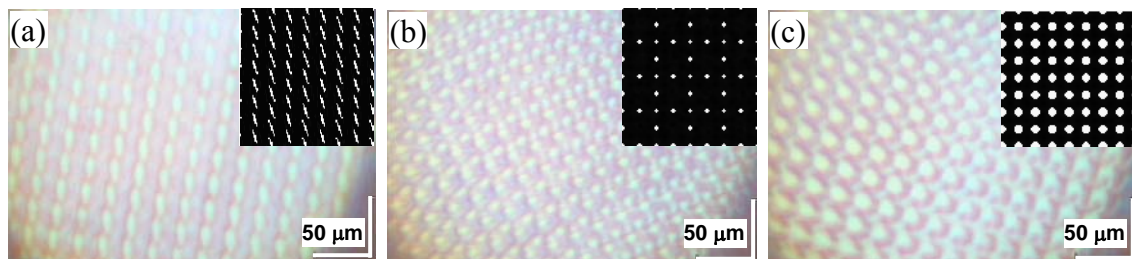
Figure 5.3 Micrographs (a), (b), and (c) are obtained under the optical microscope. The insets are the theoretical simulations which show the similar morphologies.

The surface morphologies of the samples were observed under the optical microscope. Figure 5.3(a), (b), and (c) show the micrographs of the fly's-eye lens at different microregions. The bright and dark regions are polymer-rich region and LC-rich region, respectively. It can be seen from Figure 5.3 that, the morphologies are very similar to the theoretical simulations. However, because of the aberration of the lens and the interference among the minimized light beams, the morphologies of the fly's-eye lens in different microregions are very different. Here, we only show three typical morphologies obtained. Judging from the experimental results in the following part, this morphological difference doesn't influence the performance of the fly's-eye lens very much.

5.1.4 Results and Discussion

Figure 5.4(a) shows the overall morphologies of the fly's-eye lens. By doing the Fourier transform of the micrograph, we obtained the far field pattern as shown in Figure 5.4(b). It can be seen that when a collimated light beam is incident on the fly's-eye lens, many bright spots can be obtained at the far field. The recorded pattern divides the incoming light into many beams and then these beams can interfere with each other. As a result, when a laser beam was incident on the fly's-eye lens, it can be expanded into a beam with uniform intensity. In our experiment, the incoming laser beam was about 0.8 mm in diameter with Gaussian distribution in intensity. After passing through the fly's-eye lens, the expanded beam was about 4 mm in diameter with uniform distribution in intensity at the distance of about 10 mm from the fly's-eye lens.
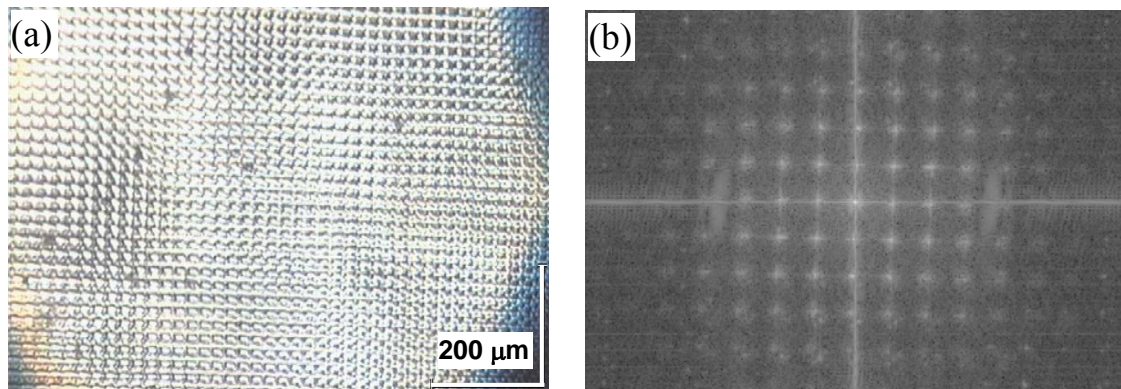
Figure 5.4 Overall micrograph of the patterned PDLC fly's-eye lens (a) and its Fourier transform pattern (b).

Figure 5.5(a) and (b) show the near and far field patterns of the PDLC fly's-eye lens, respectively. Figure 5.5(a) was obtained using a CCD 10 mm away from the fly's-eye lens when the He-Ne laser beam passed through the sample. It showed even brightness except the saw-like pattern at the circle edge. When the beam propagates

80

further along the optical path, the light beam divides into many light dots, as shown in Figure 5.5(b). This result was in good agreement with the Fourier analysis of the micrograph of the fly's-eye lens, as shown in Figure 5.4(b).
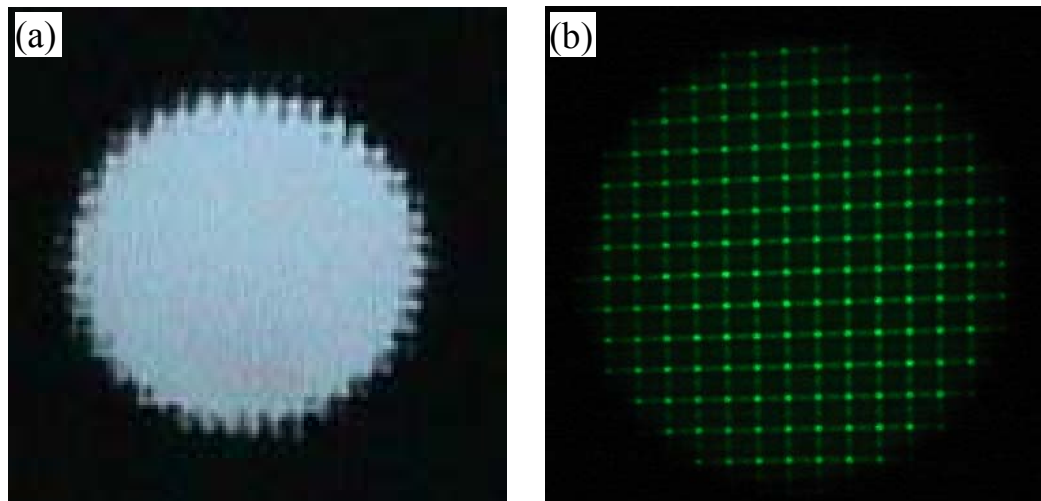
Figure 5.5 Near field (a) and far field (b) patterns of the fly's-eye lens, which are obtained by a CCD 10 mm and 20 cm away from the fly's-eye lens when the laser beam passes through it, respectively.

To check the intensity distribution, the intensities of the incoming and output light were examined using a CCD. Figure 5.6(a), (b), and (c) show the intensity distribution of the incoming light, the output light with no voltage and the output light with voltage applied, respectively. It can be seen from Figure 5.6, the incoming light is a typical Gaussian distribution, as indicted in Figure 5.6(a). With no voltage applied on the cell, the output light was modulated into a beam with an approximately flat intensity distribution, as shown in Figure 5.6(b). With an applied voltage of about 300 V, i.e. 10 V/μm, the light intensity distribution reverted to a Gaussian-like beam, as shown in Figure 5.6(c), although it seemed not perfect. Therefore, a Gaussian laser beam can be modulated into a mesa-like beam by such a PDLC fly's-eye lens. It is worth mentioning that the applied voltage was a square wave and the switching time was about 50 ms.
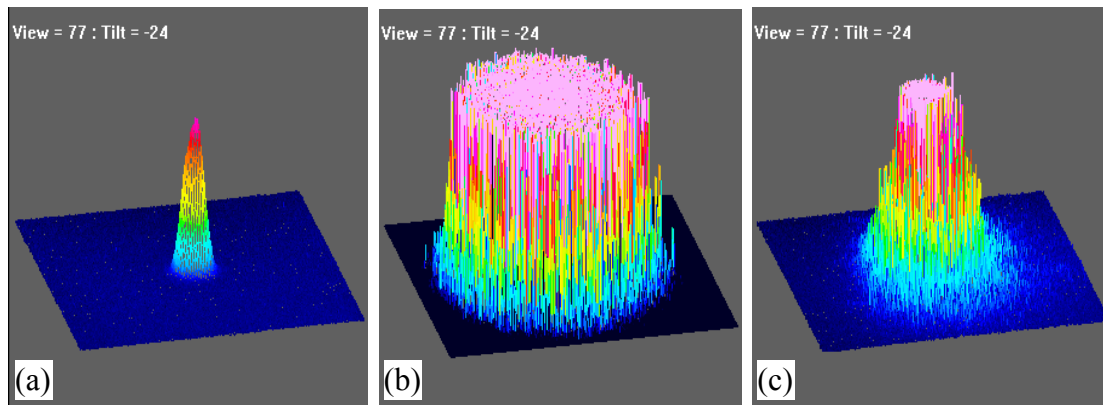
Figure 5.6 Intensity distribution of the incoming light (a), the output light without voltage (b), and with voltage applied (c), respectively.

5.1.5 Summary

In comparison with conventional glass fly's-eye lens, the major advantages of PDLC fly's-eye lens are easy fabrication process, compactness, light weight and low cost. It is a flat device, indicating a simpler fabrication process than the polymer fly's-eye lens. Moreover, PDLC fly's-eye lens is electrically tunable. However, it also shares the same drawbacks with the polymer fly's-eye lens and has poorer temperature resistance because LC can only work in relatively small temperature range. The PDLC fly's-eye lens showed good optical properties. It can modulate a Gaussian laser beam into a mesa-like beam. Our theoretical simulation showed that it could provide a good guide to control the morphologies of the recorded pattern. Such a fly's-eye lens is potentially useful in beam shaping and low intensity optical illumination systems.

5.2 Computer-Generated Hologram in PDLC

5.2.1 Motivation

Computer-generated hologram (CGH) is widely known as a useful tool for wavefront manipulations[131] and optical information processing.[132-136] It enables the

82

creation of very sophisticated optics without any limitation as to what the final diffraction pattern may look like. Many kinds of materials have been used to record CGHs. Previously, CGHs have been successfully recorded in photorefractive materials such as Fe doped LiNbO$_3$ single crystal[137] and BaTiO$_3$ crystal.[138] Guessous *et al.* even used bacteriorhodopsin as the recording material for CGH.[139] In some adaptive applications, electrically tunable holograms or diffractive elements are highly desirable because of easy control and real-time operation. Although real-time CGH can be realized based on liquid crystal spatial light modulators (SLM),[140,141] the response time is generally slow ($\geq$10 ms). By adding a portion of polymer, the response time, which is dependent on the polymer concentration, can be improved.

PDLC material has been extensively investigated for electro-optical applications.[20,32,37,142] A vitally important method used to construct PDLC devices is photo-polymerization induced phase separation (PIPS) by either UV or visible lasers, depending on the materials used. The unique property of polymer/LC composite devices is that they can be electrically tuned or switched, which is useful for adaptive optical devices. PDLC also shows a potential for high capacity data storage. Optical image storage in PDLC was reported using a conventional holography technique.[60,143,144] Here, we fabricated an electrically switchable CGH recorded in a PDLC cell with an improved response time compared to conventional LC SLM.

5.2.2 Design

In the prepolymer, the ratio of TMPTA/NVP/OA/NPG/RB was 62/25/10/2/1 by weight. In the prepolymer/LC mixture, the LC E7 concentration was about 35 wt%. The mixture was injected into a LC cell by capillary action at room temperature. The cell gap was 8 μm.

The phase distribution of the CGH was designed using the conventional iterative Fourier transform algorithm (IFTA).[145] We encoded the letters "NTU" [Figure 5.7(a)] into the CGH, consisting of 128 × 128 binary phase-only pixels. The phase value of each pixel is either 0 or π. Then the CGH was transferred to a transparency mask with an effective area of 6.4 × 6.4 mm^2 and a resolution of 50 μm. The phase distribution of the CGH on the mask is shown in Figure 5.7(b), where the black and white dots represent phase values of 0 and π, respectively. The reconstructed image of the CGH simulated is shown in Figure 5.7(c). Due to the binary phase-only structures, we can see the reconstructed twin images corresponding to the ±1st orders. Then the CGH photomask was clipped onto the LC cell filled with prepolymer/LC mixture, and subjected to a collimated He-Ne laser (543 nm) beam for recording the phase distribution by PIPS. It is worth mentioning that the laser has only about 4 mW power output. The intensity that impinged on the sample after collimation is only around 0.5 mW/cm^2. The optimized exposure time is 10 min judged from the fading of the RB color.
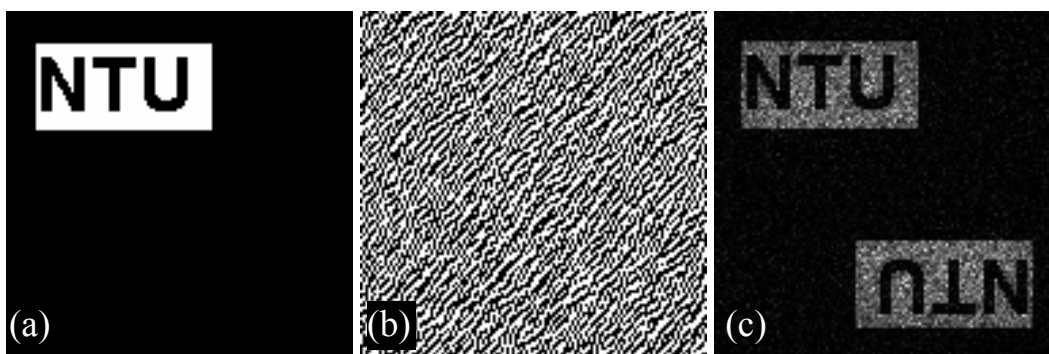
Figure 5.7 The encoded letters "NTU", (a), the phase distributions of the CGH on the transparency, (b), and the reconstructed image of the CGH simulated, (c).

5.2.3 Morphologies and Phase Difference
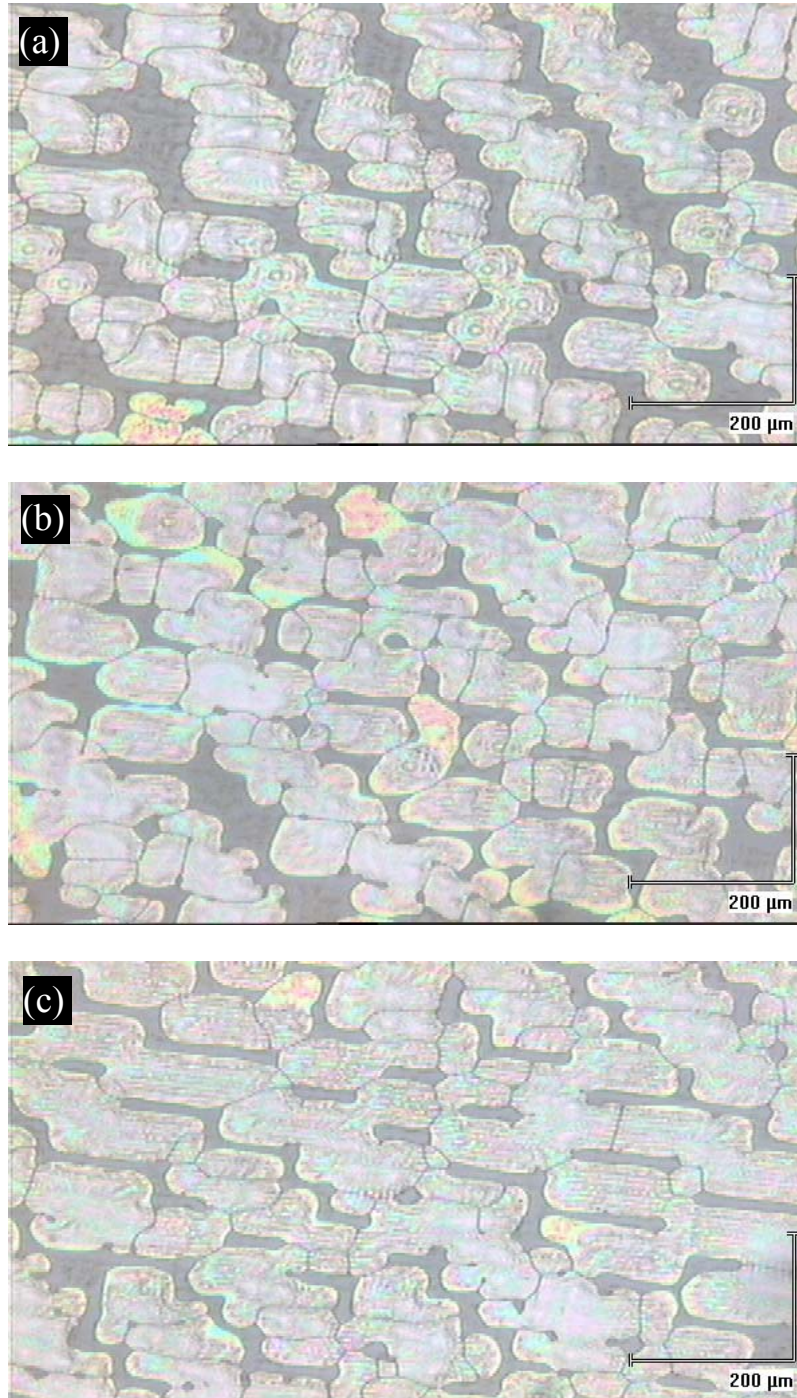
Figure 5.8 (a), (b), and (c) are the typical optical microscopic images at

three microregions of the PDLC with CGH recorded.

Figure 5.8(a), (b), and (c) show the typical morphologies under a microscope

at different microregions after phase separation. It can be seen that a good separation

between the polymer and LC happened inside the cell, where the darker and brighter areas were polymer-rich and LC-rich regions, respectively. In our configuration, the refractive index of the polymer, n_p, is set to be equal to the ordinary refractive index of the LC, n_o. Without a voltage applied, the LC molecules are randomly distributed, and an effective refractive index larger than that of the polymer is present in the bright regions. As a result, there is an index difference between the LC-rich and polymer-rich regions. Upon applying a voltage, the LC director will align along the direction of the electric field. If the indices of LC and polymer are matched, the composite film becomes a homogeneous medium and thus the phase difference disappears.

The relative phase difference ($\Delta\delta$) between the adjacent LC-rich and polymer-rich regions can be written as $\Delta\delta = 2\pi(n_{eff} - n_p)d/\lambda$, where d is the cell gap, λ is the wavelength, n_{eff} and n_p are the LC effective refractive index and polymer refractive index, respectively. The polymer-rich regions can be considered to contain pure polymer without any LC, while the LC-rich regions are filled with polymer and LC. From the optical microscopic images in Figure 5.8, the area ratio (also the volume ratio) of the polymer-rich region is statistically estimated to be 16%. Assuming the volume ratio of polymer is the same as the corresponding weight ratio (65 wt%), with a 5% volume shrinkage for polymer during polymerization, then there is about 44% polymer distributed in the LC-rich region. As a result, the LC-rich regions consist of 56% polymer and 44% LC. The effective index of the LC-rich region can then be calculated by $n_{eff} = fn_p + (1-f)n_{LC}$, where f is the volume fraction of the polymer in the LC-rich region. In our experiment, $n_p = 1.522$,[29] $n_{LC} = (2n_o+n_e)/3 = 1.596$, the estimated effective index of the LC-rich region is around 1.554. Thus, the relative phase difference estimated is around 0.9π, which is close to the desired phase difference of π.

5.2.4 Reconstruction

Figure 5.9 shows the optical setup for image reconstruction from the hologram. Light from a green He-Ne laser is firstly incident on a spatial filter system consisting of an objective lens and a pinhole. The expanded beam is then collimated and falls on the LC cell. A Fourier transform lens is used to produce the Fraunhofer diffraction pattern of the hologram in its focal plane. Because the image is too small to observe, a second objective lens with 20× magnifications is used to magnify the image.
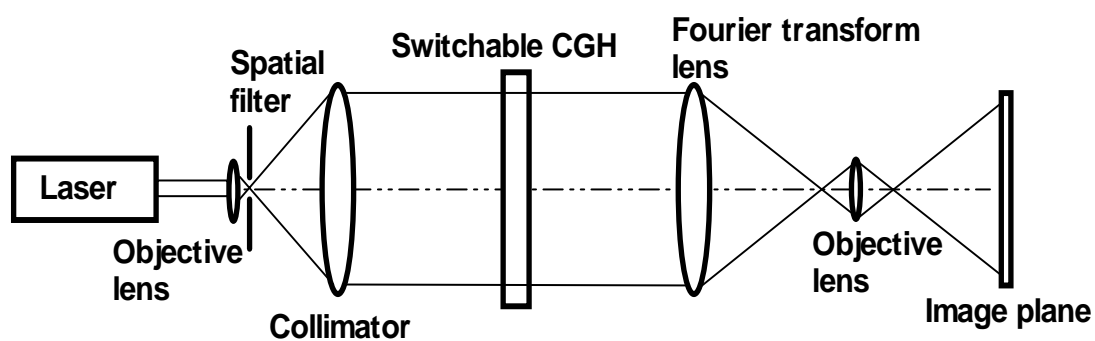
Figure 5.9 Optical setup to reconstruct the image from PDLC CGH.
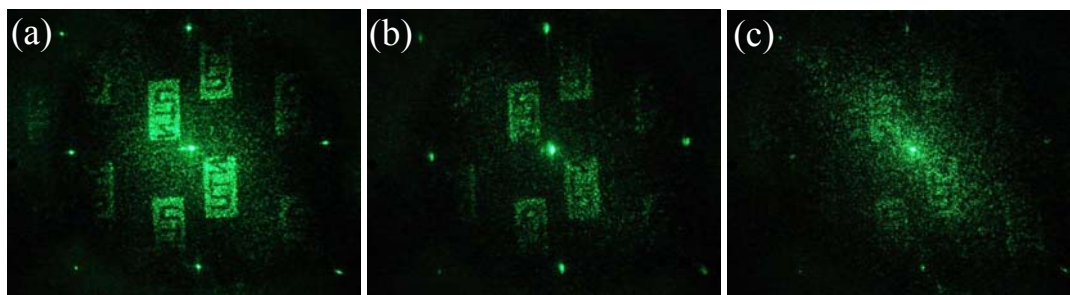
Figure 5.10 Photographs of the reconstructed CGHs at V=0, (a), V=30 V$_{rms}$, (b), and V=70 V$_{rms}$, (c), respectively.

Figure 5.10(a) shows the photograph of the reconstructed CGH without voltage applied. We can see a clear inversed "NTU" image from the photograph because an inverted phase was recorded in the PDLC film. Figure 5.10(b) shows the

reconstructed image with an applied voltage of 30 V_{rms}. It can be seen that the scattering loss reduces compared with Figure 5.10(a), which may be induced by the optical clearing effect originating from LC droplet size distribution. In PDLC, large liquid crystal droplets tend to scatter more light, producing a haze effect. With an electric field applied, these large droplets will align first due to the larger volume to surface area ratio, and the haze will disappear, thus, resulting in decreased scattering initially. When the electric field continues to increase, the smaller droplets start to align, and the index modulation decreases. As a result, the reconstructed image becomes blurred. Figure 5.10(c) shows the case with a higher applied voltage of 70 V_{rms}. We can see from Figure 5.10(c) that, the higher order diffractions become weak and more energy transfers to the 0th order due to the index matching.
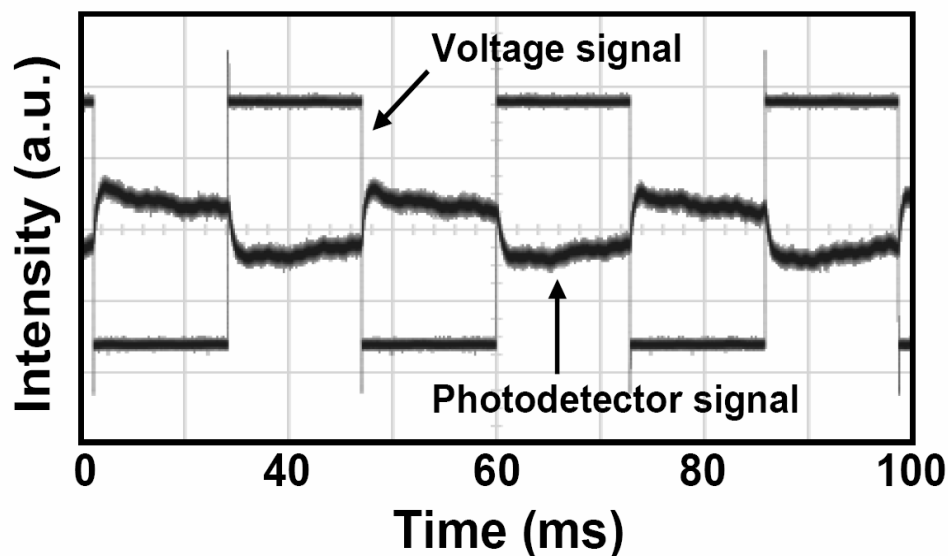
Figure 5.11 Electro-optical response of the PDLC CGH driven by a square wave.

Driven by square wave signals, the electro-optical response of PDLC CGH was captured using the experimental setup shown in Figure 3.9. Figure 5.11 shows the measured electro-optical response driven by a square wave of 50 V_{rms} with the

frequency of 20 Hz. From Figure 5.11, the rise and fall times are about 1.54 and 1.92 ms, respectively. This response time is slightly faster than that of the conventional LC SLM.

5.2.5 Summary

In summary, compared with conventional method such as direct laser writing, the major advantages of our method are an easy fabrication process, compactness, light weight and low cost. Moreover, the PDLC CGH is a write-once-read-many (WORM) mode memory device and it is electrically switchable. However, because of the low resolution of the mask and the diffraction effect in the fabrication, the pattern transfer was not good. Figure 5.12(a) and (b) show the light diffraction effect from a photomask for two different cases, one with a glass substrate and one without a glass substrate. It can be seen from Figure 5.12 that without a substrate (generally ITO glass) inserted between the photomask and PDLC film, the pattern transfer is nearly ideal, while with a substrate inserted, which is much thicker than the PDLC film, the pattern transfer is much deteriorated. As a result, the signal-to-noise ratio was low and the reconstructed image was not good enough. With optimization of the fabrication conditions, the reconstructed image can be improved.
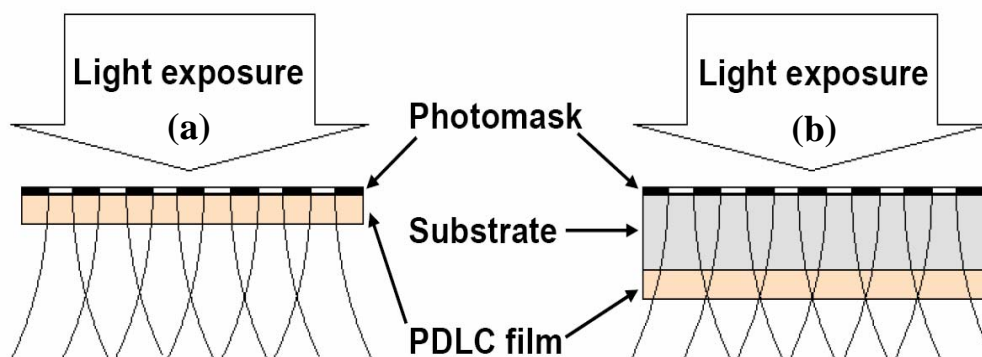
Figure 5.12 Light diffraction effect from a photomask without (a) and with (b) a substrate inserted.

89

The PDLC CGH is a kind of phase type optical element and electrically switchable. With a suitable voltage applied, the reconstructed image can be erased due to the change of the refractive index difference between the polymer-rich and LC-rich regions. The results, though preliminary, show the possibility of recording CGH in polymer/LC composite materials, which may lead to new applications for PDLC in information storage and adaptive optical elements.

CHAPTER 6   Lasing Emission Based on H-PDLC Gratings

In recent years, there has been a growing interest in compact plastic lasers. Starting from the pioneering works of Kogelnik and Shank on distributed feedback (DFB) dye lasers, several different approaches have been used to obtain laser emission in mirrorless organic devices based on the same operational principles. Many of these devices are based on transient gratings, others on permanent high resolution 1D photonic bandgap structures made with a number of different materials. Recently, light amplification phenomena have been first observed in H-PDLC reflection gratings doped with the coumarine dye. The improved fabrication techniques lead to the realization of a "one step" DFB organic laser based on dye-doped H-PDLC reflection gratings. More recently, electrically switchable laser emission has also been achieved from dye-doped H-PDLC transmission gratings with longer gain length compared to the reflection gratings. However, the results obtained are still preliminary for the dye-doped H-PDLC gratings, regardless of reflection or transmission mode. There is still room for improvement in the lasing properties, especially for the transmission mode. In this chapter, we will show significantly improved lasing properties including lower threshold, narrower linewidth, and higher Q factor.

On the other hand, inspired by the idea of a random laser from disordered medium, we investigated the possibility of obtaining random lasing based on conventional PDLC structure. The experimental results showed that with nanoscale LC droplets embedded in the polymer matrices, some discrete sharp lasing peaks (~1 nm wide) were observed on the envelope of the emission spectra.

6.1   PDLC as a Random Medium

To date, the most versatile method to form PDLC structures is photo-initiated polymerization of an initially homogenous mixture containing reactive monomers and liquid crystal molecules. These prepolymer mixtures are typically solvent free and have low viscosity. The LC droplet size ranges from nanometer to micron size by varying the LC concentration, the intensity of the curing radiation, or the photo-polymerization chemistry (free-radical or step-growth). As usual, the refractive index of the polymer, n_p, is set to be equal to the ordinary refractive index of the liquid crystal, n_o. Without a voltage applied, the LC molecules randomly distribute in the droplets. As a result, there is an index difference at the interface between the LC droplets and the polymer matrix that causes light scattering in the PDLCs. Upon applying a voltage, the LC director aligns along the direction of the electric field. If the indices of the LC and polymer are matched, the light scattering will disappear.

On the other hand, random lasing stimulated considerable interest due to a special mechanism. In a random laser, light waves are trapped by multiple light scattering (light diffusion), which takes over the role of the cavity in a conventional laser.[146,147] To obtain a random laser, the passive or active scattering particles such as SiO_2 and ZnO powder were usually doped into the laser media to obtain the light amplification.[148-150] Dye-doped PDLCs can also be a good candidate for the random laser media. However, the reported random lasing from dye-doped PDLC has large LC droplets of micron size,[151,152] which can not offer enough coherent light scattering. Here, we investigated the dye-doped nanoscale PDLCs and obtained better random lasing compared to the micron scale ones. Some discrete sharp lasing peaks (~1 nm wide) were observed on the envelope of the emission spectra in PDLCs.

6.1.1 Material Preparation and Fabrication

In our experiments, the materials used to fabricate the dye-doped PDLC film consisted of 45.41 wt% TMPTA, 7.89 wt% NVP, 0.63 wt% RB, 1.02 wt% NPG, 9.45 wt% OA, and 1.26 wt% lasing dye, 4-(dicyanomethylene)-2-methyl-6-(4-dimethylaminostyryl)-4H-pyran (DCM) (all from Sigma-Aldrich), and 34.33 wt% liquid crystal, E7. The surfactant used here is to decrease the anchoring energy at the interface of polymer and LC. As a result, the LC droplets could be more ideally spherical in shape. All the materials were mechanically blended and stirred in the dark in an ultrasonic cleaner at 65 °C (higher than the clearing point of the LC E7) for at least 2 hrs to form a homogeneous mixture.

The mixture was injected in a cell by capillary effect, and then subjected to a uniform exposure of an Ar^+ laser operating at 514.5 nm. The exposure intensity on the sample was about 20 mW/cm^2 and the exposure time was 2 mins. The laser exposure induces a fast polymerization, which results in the nanoscale LC droplets, and the uniform exposure helps the droplets to distribute in the polymer matrix as evenly as possible. After exposure, the samples were further cured for 5 mins by a mercury lamp to ensure the complete polymerization of prepolymer. The thickness of the samples was 6.5 μm.

6.1.2 Lasing Measurement

The schematic setup of the lasing measurement is shown in Figure 6.1. The pump laser used is a linearly polarized, Q-switched, and frequency doubled 532 nm Nd:YAG pulsed laser (Spectra Physics DCR3) with a pulse duration of 7 ns and repetition rate of 10 Hz. The laser beam was focused onto the surface of the PDLC film by a cylindrical lens, which has a focal length of $f = 40$ cm, to form a narrow

strip gain area on the surface of the sample ~0.5 mm wide and ~10 mm long. The detector was placed on the edge of the sample to collect the lasing signal and connected to a spectrometer that was monitored in real-time by a computer.
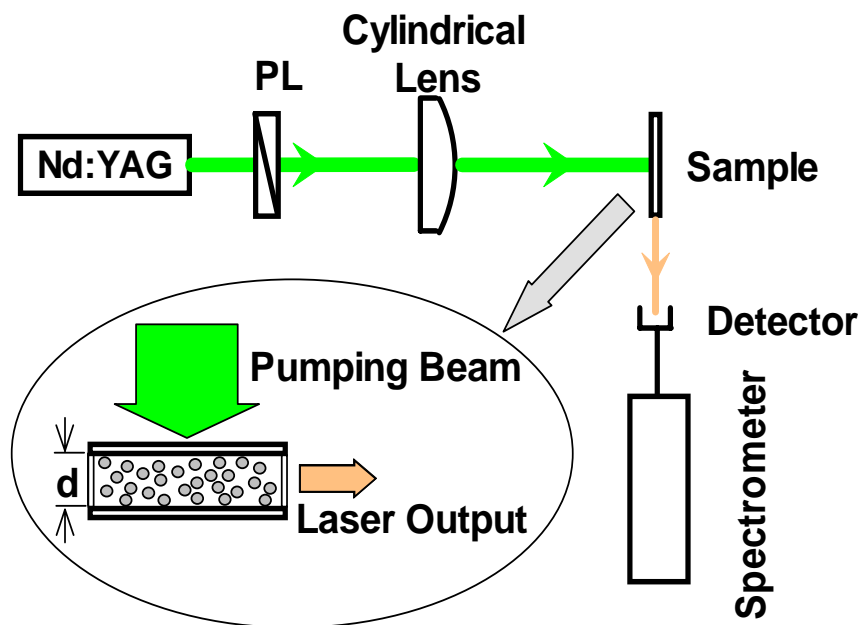
Figure 6.1 Schematic setup of lasing measurement.

6.1.3 Results and Discussion

Figure 6.2 shows the SEM image of the DCM-doped PDLC film. It can be seen from Figure 6.2 that, the LC droplets randomly distribute in the polymer matrix, and the size of most LC droplets ranges from 20 to 80 nm in diameter, judging from the small holes (darker regions) where the LC droplets reside. For the PDLC films in our experiments, the refractive index, n_p, of the polymer matrix is about 1.52~1.53.[29] The effective refractive index, n_{eff}, of the LC droplets is about 1.60, which is obtained by the following formula, $n_{eff} = (2n_o + n_e)/3$. Because $n_{eff} > n_p$, the LC droplets are expected to serve as scatterers in our experiments.
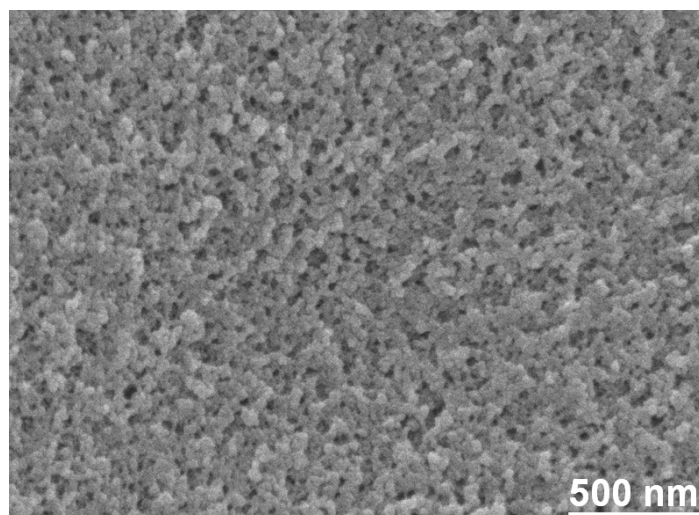
Figure 6.2 SEM image shows the surface morphology of a PDLC with nanoscale LC droplets.
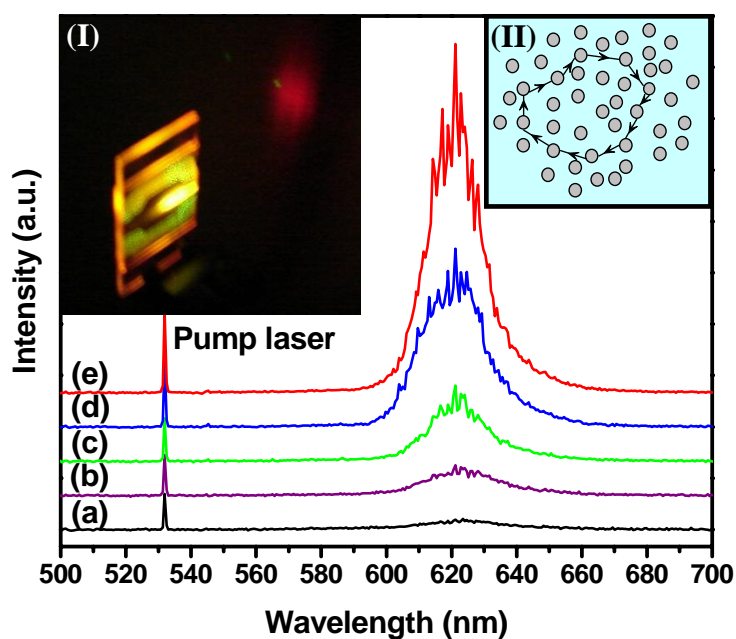
Figure 6.3 Emission spectra with various pumping energies of (a) 20, (b) 25, (c) 28, (d) 35, and (e) 47 µJ/pulse, respectively. The insets I and II are an emission photograph of the dye-doped PDLC excited at 40 µJ/pulse and a schematic diagram showing the formation of a closed loop path of light through recurrent scattering in a PDLC, respectively.

The emission spectra from the dye-doped PDLC with various pumping energies of (a) 20, (b) 25, (c) 28, (d) 35, and (e) 47 μJ/pulse are shown in Figure 6.3. It can be seen from Figure 6.3 that, at a low pumping energy, a broad band is observed, and the linewidth is about 40 nm. When the incident pumping energy exceeds 25 μJ, discrete peaks emerge in the emission spectra. The linewidth of these peaks is about 1 nm, which is more than 40 times narrower than the amplified spontaneous emission (ASE) linewidth below the threshold. It is worth mentioning that the lasing peak was not absolutely accurate because of the low resolution (only about 0.6 nm) of the spectrometer used. When the pump intensity increases further, more sharp peaks appear. These discrete peaks result from recurrent light scattering. As shown schematically in inset II of Figure 6.3, light may return to a scatterer from which it is scattered before, and thereby forming a closed loop path. When the amplification along the closed path exceeds the loss, laser action can occur in the loop which serves as a resonant cavity. The requirement of the phase shift along the closed loop should satisfy,

$$\Delta\varphi = \frac{2\pi}{\lambda}\ell = 2\pi m \, , \qquad\qquad (6.1)$$

where ℓ is the length of the closed loop, $\ell = m\lambda$, m is an integer, and λ is the wavelength of the emission light in the random medium. From Eq. (6.1), the closed loop length determines the oscillation frequencies. Laser emission from these cavities results in discrete narrow peaks in the emission spectrum. Unlike the mobile particles in the solution, where the frequencies of lasing modes changes from pulse to pulse,[149] in our sample, the LC droplets are fixed in the polymer matrix once the prepolymer polymerized. As a result, the originally formed loops do not change and some new loops may be formed with the increase of the pumping energy. Therefore, we can see from Figure 6.3, the original peaks increase strongly and some new peaks appear with

the increase of the pumping energies. Inset I of Figure 6.3 shows the photograph of the emission from the dye-doped PDLC excited by a 40 μJ/pulse.

Figure 6.4 shows the dependence of the emission spectra as a function of the pumping energy. It can be seen from Figure 6.4 that, there is a clear threshold behavior. The threshold of the random lasing is about 25 μJ/pulse. The broad ASE band narrows significantly with the increase of pumping energy, i.e. gain narrowing, at low pumping energy below a threshold. Above the threshold, a fine structure consisting of a number of sharp peaks on the envelope of the ASE spectrum appears and increases abruptly with the increase of pumping energy. The spectral width of these sharp peaks is less than 1 nm. At a pumping energy of about 55 μJ/pulse, the full width at half maximum (FWHM) of the ASE emission spectra is about 13 nm, which keeps almost constant with a further increase of the pumping energy.
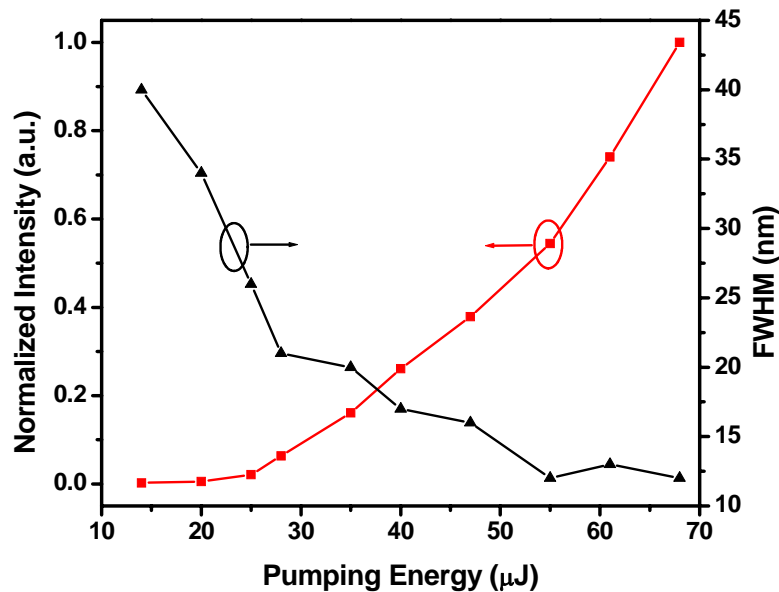
Figure 6.4 The output intensity and FWHM of the ASE spectra from DCM-doped PDLC film as functions of the laser pumping energy.

The lasing modes from the dye-doped PDLC gratings were also investigated. Figure 6.5 shows the transverse magnetic (TM) and transverse electric (TE) lasing

modes from the DCM-doped PDLC film at a pumping energy of 40 µJ/pulse. From Figure 6.5, we can see that, the lasing mode is nearly TE polarized. In our previous report,[142] the TE and TM modes from thick H-PDLC transmission gratings (about 30 µm) had little difference in intensity. However, in this experiment, the LC cell thickness was 6.5 µm. It is obvious that the thickness of the film plays an important role in selecting the lasing modes. In fact, our PDLC sample can be viewed as a planar dielectric waveguide, where the light modes are related to the thickness of the waveguide.[153] Because the average refractive index of PDLC (>1.52) is larger than that of the glass substrates (~1.50), the light can be confined between the two glass plates. On the other hand, the LC droplets are actually anisotropic due to the shrinkage during the polymerization process.[154] As a result, TE and TM modes will have different cutoff thickness in the PDLC film, which contributes to the difference in intensity of TE and TM modes. With the decrease of the cell thickness, the lasing mode can be totally TE polarized.[155]
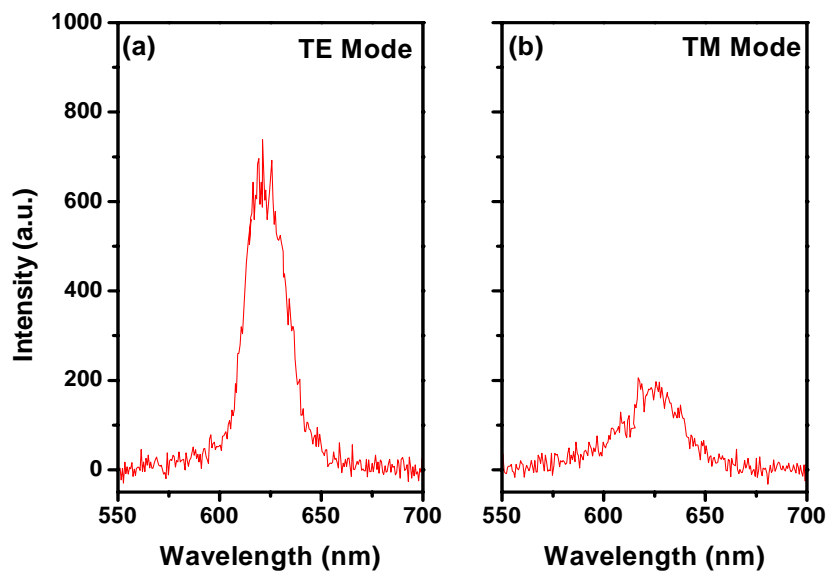
Figure 6.5 (a) TE and (b) TM polarized emission spectra for the DCM-doped PDLC film.

6.2   *Single-Mode Lasing Emission from DFB Structures*

The LC-based photonic bandgap materials have received considerable interest for optoelectronic applications. With the existence of a bandgap, it is possible to achieve lasing with the use of proper dyes and pumping sources. The dye-doped LC-based materials exhibit large optical gain over broad spectra in the visible range. Moreover, LC can be electrically or thermally tuned. These features are well suitable for use as tunable single-mode lasers. The most familiar LC-based lasing medium is the cholesteric LC with its helical structure, a 1D photonic crystal, which has been extensively investigated.[156-161]

More recently, attention has been given to lasing in H-PDLCs. For the lasing emission from the dye-doped H-PDLC gratings, compared to the reflection mode, the transmission mode enjoys a longer gain length, which facilitates low threshold lasing. By now, only Hsiao *et al.* reported the lasing emission from a dye-doped H-PDLC transmission grating.[79] But the results were preliminary. There is still room for improvement of the lasing properties. In this section, we will show significantly improved lasing properties, including lower threshold, narrower linewidth, and higher Q factor.

6.2.1 *Material Recipe and Fabrication*

To investigate the single-mode lasing properties from the dye-doped H-PDLC transmission gratings, we chose two different lasing dyes: 4-(dicyanomethylene)-2-methyl-6-(4-dimethylaminostyryl)-4H-pyran (DCM), 1#, and rhodamine B (RhB), 2#. Their corresponding chemical structures are shown in Figure 6.6. The other materials used were the same as the previous ones for random lasing. The detailed concentrations for each chemical are listed in Table 6.1. Under the same fabrication conditions, we fabricated the DCM and RhB dye-doped H-PDLC transmission

gratings for laser testing. The recorded grating area was about 6×10 mm^2. The thickness of the sample was controlled to be ~30 μm or 6.5 μm.

Table 6.1 Detailed concentrations for each chemical.

No.	TMPTA	NVP	NPG	RB	OA	Dye	E7
1#	41.0	16.0	1.3	0.7	7.0	1.0	34.0
2#	47.0	6.0	1.2	0.8	10.0	1.0	34.0

DCM   RhB
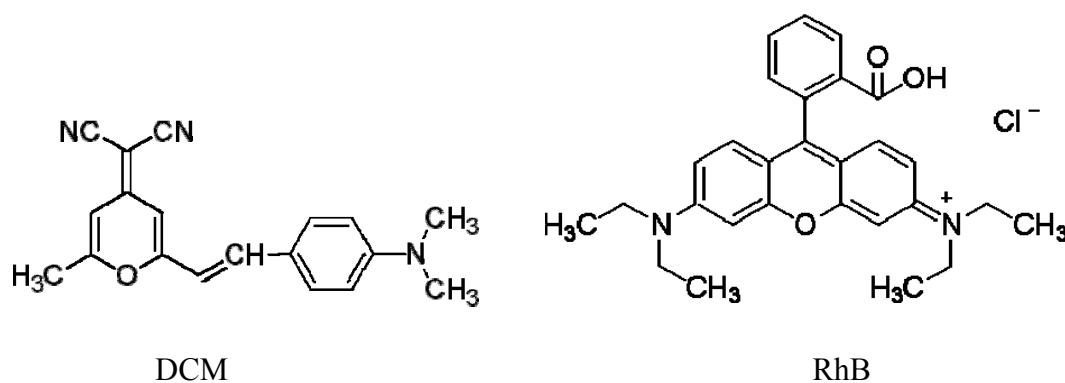
Figure 6.6 Chemical structures of DCM and RhB.

6.2.2 Absorption and Photoluminescence Spectra

The absorption and photoluminescence (PL) spectra of the DCM and RhB doped H-PDLC films are shown in Figure 6.7. It can be seen from Figure 6.7 that, the DCM (RhB)-doped H-PDLC film exhibits a broad fluorescence emission band, 520 - 750 nm (550 - 700 nm), and the absorption band is in the UV range (high absorption, not shown here) and the visible range for wavelengths less than 600 nm. In addition, in the spectral range of 500 - 600 nm, there is an obvious overlap between the absorption band and the PL band. Generally, the lasing action is difficult to achieve in this spectral range due to the re-absorption of the emitted fluorescence signals. However, we even obtained lasing emission centered at around 580 nm. In contrast,

lasing above 600 nm can be expected to occur more easily, where the absorption is negligible and the gain is relatively high. In our experiments, the writing wavelength was 514.5 nm, as indicated in Figure 6.7. At this specific wavelength, the photoinitiator, RB, will absorb more light than the DCM dye, which ensures not only complete polymerization but also as low as possible photodegradation of the dye. Moreover, a low intensity UV light was used to avoid the photodegradation of the dye during the postcure of the gratings.
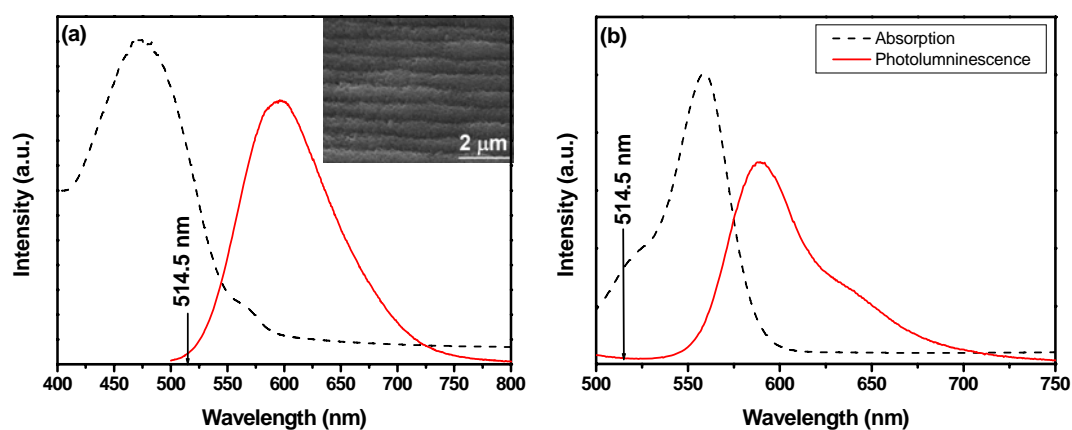
Figure 6.7 Absorption (dashed) and PL (solid) spectra of DCM (a) and RhB (b) doped H-PDLC grating films. The wavelength used to write the gratings, 514.5 nm, is indicated in the figure. The inset is a SEM image showing the surface morphology of the grating.

In our experiments, the wavelength used for writing the grating was 514.5 nm. According to the geometrical structure of exposure, the grating pitch can be calculated using the following formula,

$$\Lambda = \frac{\lambda}{2n\cos[\alpha + \sin^{-1}(n^{-1}\cos\alpha)]}, \qquad (6.2)$$

where λ is the recording wavelength, n is the refractive index of the prism, and α is the incident angle. In our experiments, $\lambda = 514.5$ nm, $n = 1.52$, and $\alpha = 45°$, therefore,

the calculated grating pitch is about 0.57 μm. The inset in Figure 6.7(a) shows the surface morphologies of the DCM-doped H-PDLC grating. It can be seen that, a clear and relatively uniform grating structure is formed and the grating period is about 0.58 μm, which is in good agreement with the theoretical calculation.

6.2.3 Results and Discussion
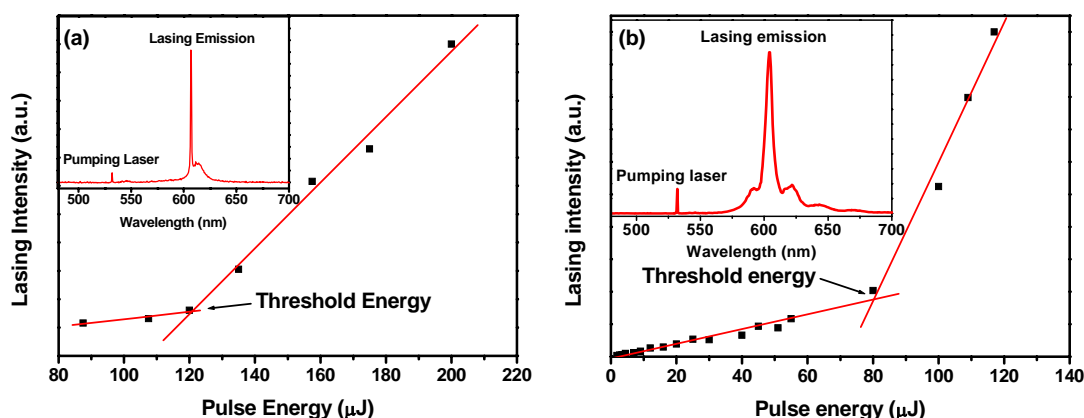
Figure 6.8 Output lasing intensity from (a) DCM- and (b) RhB-doped H-PDLC transmission grating as a function of the laser pumping energy. The insets show the lasing and the pump laser spectra, respectively.

With the same measurement setup as shown in Figure 6.1, the lasing properties were tested. The measured output lasing intensity from the dye-doped H-PDLC as a function of the pumping laser energy is shown in Figure 6.8. It can be seen from Figure 6.8 that, the threshold pumping energies are about 120 and 80 μJ/pulse, respectively, which is considerably lower than previously reported.[79] A possible reason of the low threshold excitation intensity may be the uniform grating, which provides uniform coherent distributed feedback. We found that the uniformity strongly affected the performance of the lasing emission. The higher uniformity of the grating decreases the scattering, increases the coupling of the pumping light, and most

importantly, provides uniform coherent distributed feedback, resulting in lower threshold. Above the threshold, we can see that the emitted laser intensity linearly increases with increasing pumping laser energy. Far above the threshold energy, dye photodegradation was observed, which has been reported previously.[162,163]
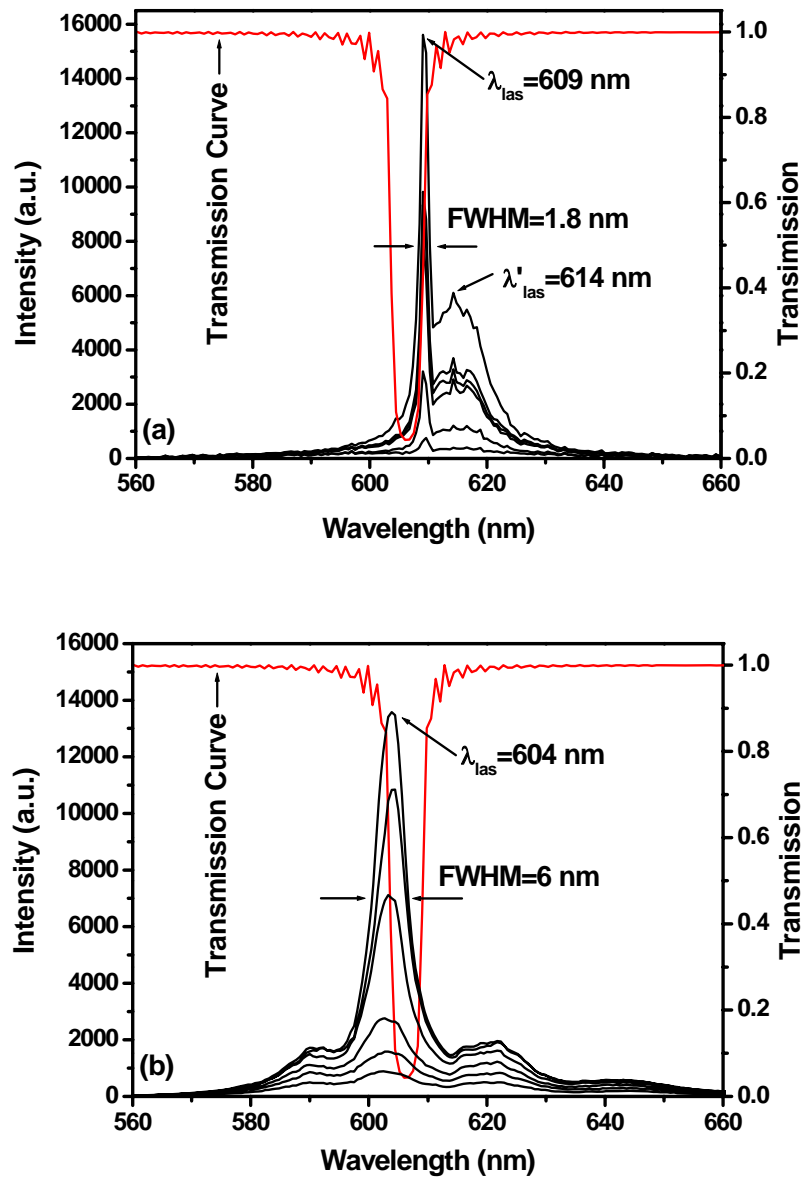
Figure 6.9 The lasing spectra obtained at various pumping intensities for DCM-doped H-PDLC transmission gratings. The simulated transmission spectrum of the grating along the grating vector direction is also shown in the figure.

Figure 6.9 shows the lasing spectrum excited with various pumping laser intensities. The pumping intensities are 87.5, 107.5, 120, 135, 157.5, and 175 μJ/pulse in Figure 6.9(a), and 30, 45, 80, 100, 109, and 117 μJ/pulse in Figure 6.9(b), respectively. It can be seen from Figure 6.9 that, the lasing peaks center at about 609 nm with the FWHM of about 1.8 nm and at about 604 nm with a FWHM of about 6.0 nm. It is worth mentioning that, the lasing peak was not absolutely accurate because of the low resolution (only about 0.6 nm) of the spectrometer used. From the results, the lasing from the RhB-doped H-PDLC gratings shows much broader emission compared to the DCM-doped one. As we fabricated and pumped the samples at the same conditions, the emission width may be dependent on the dye itself. We can also see from Figure 6.9(a) that, with the increase of pumping intensity, a new peak around 614 nm appears. This is because the grating structures cannot provide enough gain suppression for the residual stimulated emission, i.e. amplified spontaneous emission.

As previously reported for dye-doped reflection gratings, lasing was generally generated at the edge of the bandgap of the 1D photonic crystal, because the photon group velocity approaches zero and the gain of the grating is enhanced greatly at the edge of bandgap.[163,164] The HPDLC transmission grating also has a periodic structure with alternating LC-rich layers and polymer-rich layers along the grating vector direction. Light propagates in this structure as through multi layers. The multi layered structure consists of n pairs of two lossless isotropic materials with refractive indices n_1 and n_2, with different thicknesses d_1 and d_2, which actually correspond to the volume ratios V_{LC} and V_p. The transmitted and reflected intensities (t_n, r_n) through n layers are given by

$$\begin{bmatrix} t_n \\ r_n \end{bmatrix} = \cdots (P_2 D_2^{-1} D_1)(P_1 D_1^{-1} D_2)(P_2 D_2^{-1} D_1) P_1 P_1^{-1} \begin{bmatrix} t \\ 0 \end{bmatrix}, \qquad \textbf{(6.3)}$$

where

$$D_{1,2}^{TE} = \begin{bmatrix} 1 & 1 \\ k_{1,2} & -k_{1,2} \end{bmatrix} \qquad\qquad (6.4)$$

$$P_{1,2} = \begin{bmatrix} \exp(jk_{1,2}d) & 0 \\ 0 & \exp(-jk_{1,2}d) \end{bmatrix} \qquad\qquad (6.5)$$

$$k_{1,2} = n_{1,2}\cos\theta_{1,2}, \qquad\qquad (6.6)$$

where P and D mean the propagation and development matrices, respectively, λ is the wavelength of the emission light, θ_1 and θ_2 are the angles of incidence and refraction, respectively. For our transmission H-PDLC grating, we have calculated the bandgap of the grating, assuming the LC droplets are sufficiently small so that the director configuration in the droplet can be neglected. Shown in Figure 6.9 is also the transmission spectrum of our transmission grating, a 1D photonic crystal. The data used in our calculation are as follows: the grating pitch, Λ, is 0.58 μm, the effective refractive indices, n_{LC} and n_p, of liquid crystal-rich and polymer-rich channels are 1.60 and 1.54, respectively, liquid crystal and polymer volume ratios, V_{LC} and V_p, are 0.4 and 0.6, respectively. It is clear from Figure 6.9 that the lasing emission is located at both edges of the reflection band, which is in good agreement with the theoretical calculation. Theoretically, the lasing due to the suppression of group velocity of the light should occur at the lower energy edge of a bandgap. However, the lasing happens at the higher energy edge of the bandgap in Figure 6.9(b). As we can see from Figure 6.7(b), the PL efficiency at 604 nm is higher than that at about 609 nm, which means that at 604 nm the gain is larger. Therefore, during the competition of the two edge emission, the emission at 604 nm becomes dominant and the other one at 609 nm is suppressed.

For lasers, an important parameter is the quality factor, *Q*, which can be described by

$$Q \approx \frac{\lambda_{las}}{\Delta \lambda} \qquad\qquad (6.7)$$

where λ_{las} is the laser wavelength emitted from the grating, and $\Delta\lambda$ is the linewidth. From Figure 6.9(a), with λ_{las} = 609 nm and $\Delta\lambda$ = 1.8 nm, we can obtain the quality factor, *Q*, of about 338, which is comparable to conventional lasers. However, the *Q* factor is lower compared with that of other microlasers,[165] due to the imperfection of the gratings. As known, the Q factor is proportional to the photon dwell time, $\tau = Q/2\pi v_c$, i.e., the higher τ is, the lower the lasing threshold is, therefore, a lower Q factor results in higher lasing threshold. With the improvement of the grating quality and decrease of the grating pitch, a higher *Q* factor and a lower threshold would be obtained.

The lasing modes from the dye-doped H-PDLC gratings were also investigated. Figure 6.10 shows the TM and TE lasing modes from DCM- and RhB-doped H-PDLC structures with the film thickness of ~30 μm. From Figure 6.10, we can see that, both TM and TE modes exist in the H-PDLC structure and the intensity of the TE mode is a little larger than that of the TM mode. The thickness of the H-PDLC film plays an important role in selecting the lasing modes. As known, H-PDLC transmission gratings are anisotropic distributed feedback structures in which the TE and TM mode cutoff thickness is different; therefore, the intensities of the TE and TM modes are different. With careful control of the thickness, the lasing mode can be totally TE polarized.[155]
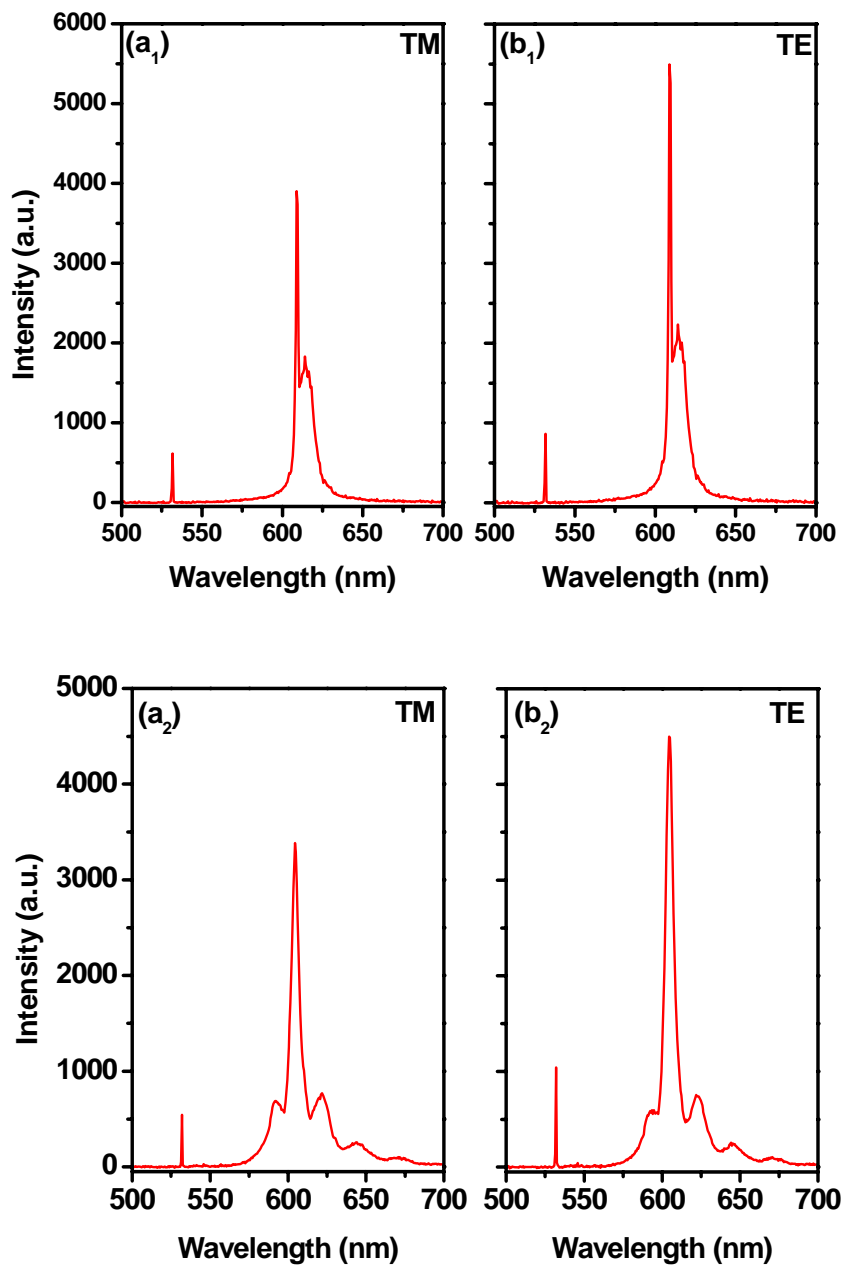
Figure 6.10 TM (a_1), (a_2) and TE (b_1), (b_2) polarized emission spectra for the DCM- and RhB-doped H-PDLC transmission grating, respectively.

6.3 Liquid Crystal Concentration Effect

LC concentration plays an important role in the lasing generation and wavelength selection. In this section, we investigate the effect of LC concentration on

the lasing properties based on the H-PDLC transmission grating. We found that 35% LC concentration was an approximately critical value to obtain single-mode lasing from a dye-doped H-PDLC. With the decrease of the LC concentration, the lasing wavelength was blue-shifted. Typically, a 30 wt% LC concentration was used for H-PDLC transmission gratings to achieve high diffraction efficiency. However, for lasing generation, the LC concentration of around 20 wt% was found to be the best trade-off between sufficient index modulation and optical scattering in the samples.

6.3.1 Material Recipe

We changed the LC and TMPTA concentrations and kept the other material concentrations fixed. The detailed weight percentage of each component used in the material mixture is shown in Table 6.2.

Table 6.2 wt% of each component used in the prepolymer syrup for sample 1-6.

No.	TMPTA	NVP	NPG	RB	OA	DCM	E7
1#	67.1	7.8	0.9	0.6	8.0	1.0	14.6
2#	63.1	5.6	0.7	0.5	9.2	1.2	19.7
3#	57.8	6.0	0.7	0.5	9.5	1.2	24.3
4#	53.6	6.5	0.8	0.5	7.4	1.4	29.8
5#	47.6	7.4	0.9	0.6	8.1	1.2	34.2
6#	34.1	6.3	0.7	0.6	8.4	1.1	48.8

6.3.2 Results and Discussion

Figure 6.11 shows the measured lasing threshold and lasing wavelength for the dye-doped H-PDLC as a function of the LC concentration. It can be seen from Figure

6.11 that, the LC concentration plays an important role in the lasing threshold and the lowest threshold of pumping energy is about 5 µJ/pulse at a LC concentration of 19.7 wt%. From Figure 6.11, we can also see that with the decrease of the LC concentration from 34.2 wt% to 14.6 wt%, the lasing wavelength was blue-shifted from 627 nm to 584 nm.
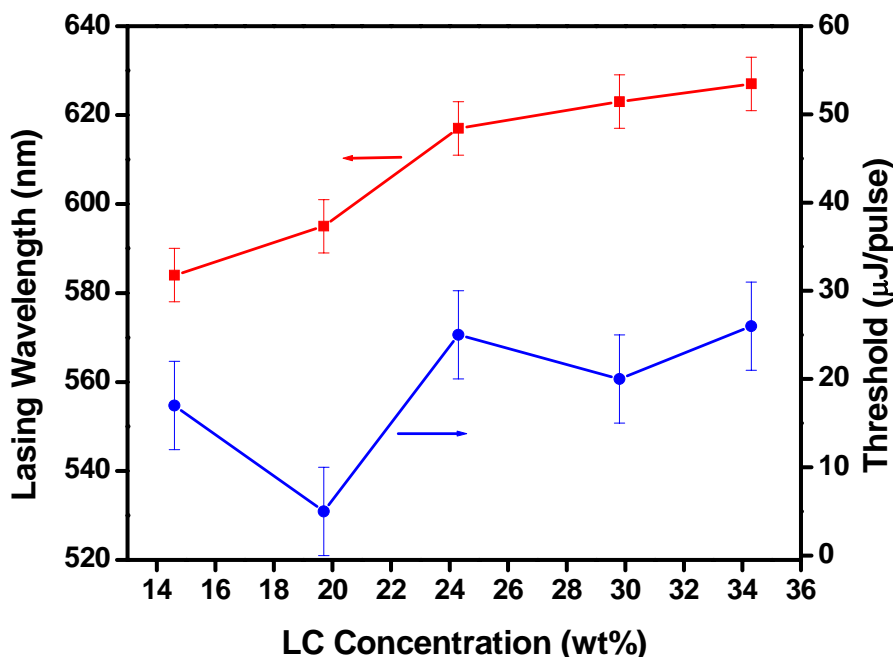
Figure 6.11 Measured lasing threshold and lasing wavelength from the DCM-doped H-PDLC as a function of the LC concentration. The accuracies for the threshold and lasing wavelength are around ±5 µJ/pulse and ±6 nm, respectively.

It is worth mentioning that, different from our previous result (shown in Figure 6.9(a)), at almost the same LC concentration of 34 wt%, the lasing peak wavelength was 627 nm (compared to 609 nm in Figure 6.9(a)). The difference in lasing wavelength is due to the concentration of cross-linking monomer, NVP, which plays an important role in controlling the LC droplet size.[42,106] Figure 6.12 shows obviously different surface morphologies of H-PDLC transmission gratings prepared
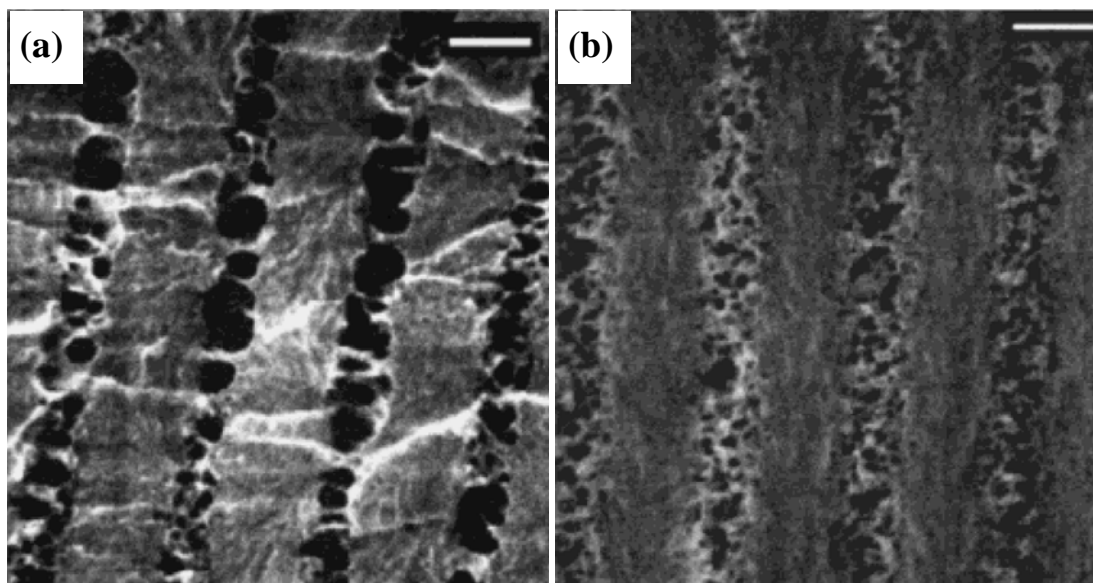
Figure 6.12 SEM images of H-PDLC transmission gratings with (a) 4 wt% and (b) 15 wt% NVP. Scale bars represent 600 nm. (From Ref. 106)
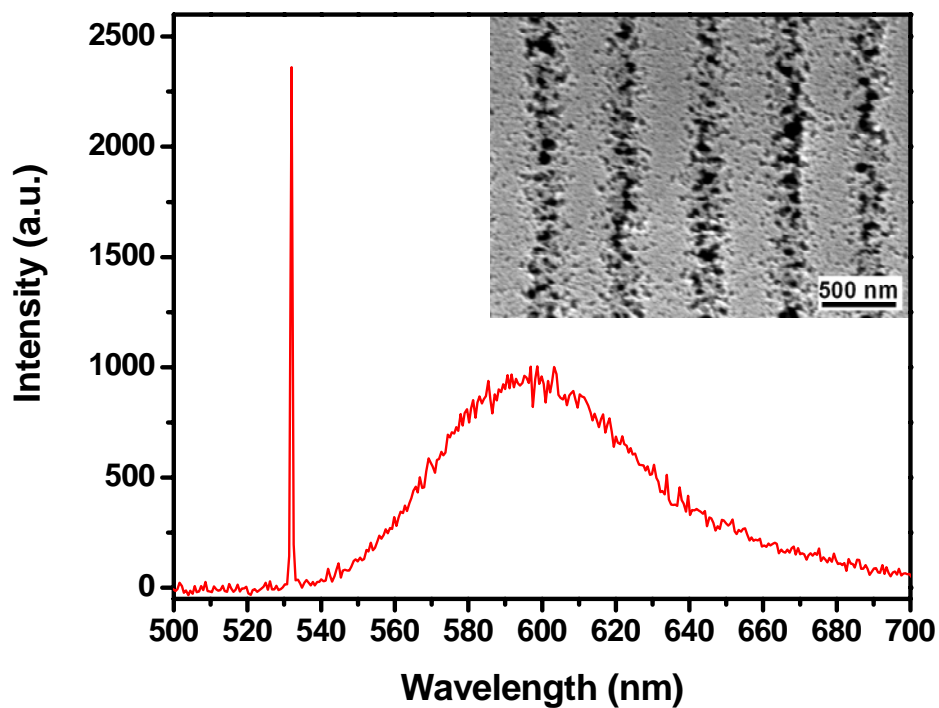
Figure 6.13 The spectra obtained with LC concentration of 48.8 wt% for material recipe 6#. The inset is SEM image corresponding to the LC concentration.

with 4 wt% and 15 wt% NVP, respectively. It can be seen that increasing the amount of NVP leads to smaller droplets and decreases the anisotropy of the LC droplets. For the material recipe 1# in Table 6.1, the concentration of NVP was larger than that reported here. Therefore, the index modulation in H-PDLC was smaller than that reported here, resulting in a blue-shifted lasing wavelength.[166] It is worth mentioning that for the dye-doped H-PDLC transmission grating using material mixture 6# with 48.8 wt% LC, only ASE was obtained regardless of how high the pumping energy was (as shown in Figure 6.13).
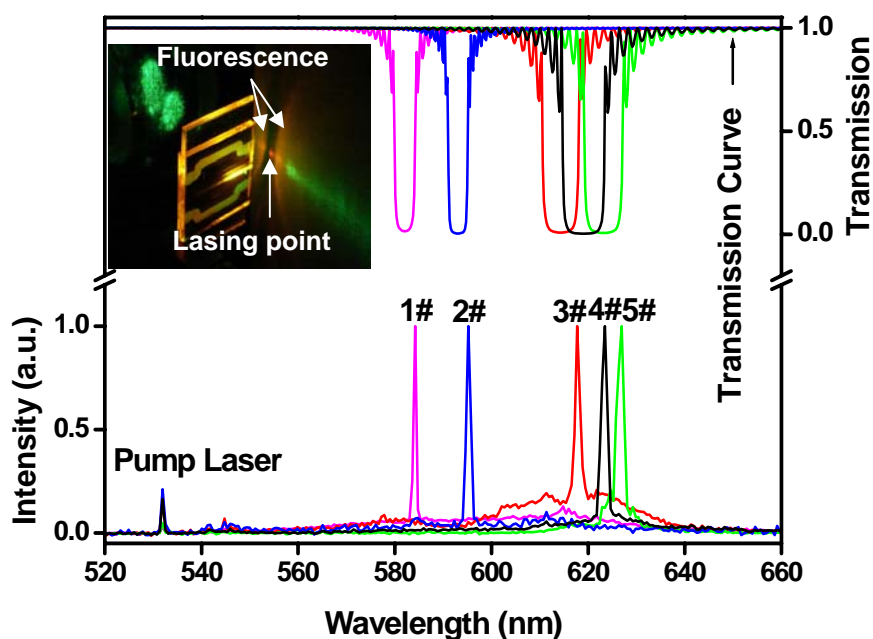
Figure 6.14 Normalized lasing spectra for H-PDLC samples with various LC concentrations excited by about two times the corresponding threshold. The inset shows a typical emission photograph of the dye-doped H-PDLC.

Figure 6.14 shows the normalized lasing spectra for H-PDLC samples with various LC concentrations excited by about two times of the corresponding threshold. It can be seen from Figure 6.14 that, the linewidth of the lasing peak becomes

narrower with a decrease in the LC concentration. The FWHM of the lasing peak centering at 584 nm was less than 0.8 nm. The transmission curves along the grating vector direction are also theoretically calculated, as shown in Figure 6.14. The refractive index of the polymer matrices was assumed to be 1.54. The other data used in our calculations are tabulated in Table 6.3. It is worth mentioning that in our calculations, the wavelength dispersion of the refractive indices of the LC and polymer used are not considered because the refractive index changes of the LC[167] and polymer[168] are small enough to be ignored. It is clear that the lasing action happens at one edge of the reflection band. The inset in Figure 6.14 shows a typical emission photograph of the dye-doped H-PDLC, where a sharp lasing point can be clearly observed. The estimated divergence angle from the far-field pattern was ~15 mrad and ~65 mrad in the directions perpendicular and parallel to the substrates, respectively.

Table 6.3 Data used for the transmission curve calculation. Λ_G is the grating pitch, $V_{LC}:V_p$ is the volume ratio of LC-rich lamellae to polymer-rich lamellae, respectively, Δn_1 is the index modulation.

No.	Λ_G (μm)	$V_{LC}:V_p$	Δn_1
1#	0.564	16:84	0.05
2#	0.572	25:75	0.07
3#	0.583	45:55	0.09
4#	0.584	50:50	0.10
5#	0.584	55:45	0.11

As reported previously,[89] lasing properties of H-PDLC transmission gratings are strongly dependent on the morphology of the grating. In our previous report,[29] the morphology significantly changed in H-PDLC transmission gratings as the LC concentration changed. At a higher concentration, the volume fraction of LC-rich lamella increases and the LC droplets become larger. As a result, a larger scattering loss is induced and the lasing has a larger threshold and wider FWHM. At a lower concentration, the volume fraction of LC-rich lamellae decreases and the LC droplets become smaller. Within the LC-rich lamellae, a large amount of polymer exists and the index modulation is lowered accordingly. As a result, only a higher threshold can sustain enough distributed feedback, and a narrower FWHM is obtained due to the smaller scattering loss. Moreover, lower LC concentration reduces the index modulation, resulting in a blue-shifted bandgap. Therefore, the lasing wavelength is blue-shifted accordingly. In our experiments, we found that the LC concentration of around 35 wt% was close to the critical value to obtain single-mode lasing from a dye-doped H-PDLC transmission grating. At a higher concentration of 48.8 wt%, only ASE was observed. In our experiments, to achieve a lasing emission with better properties from H-PDLC transmission gratings, the LC concentration of around 20 wt% was found to be the best trade-off between sufficient refractive index modulation and optical scattering in the samples.

6.3.3 Thermally Switchable Lasing

For the devices based on H-PDLC, a distinct advantage is that they can be tuned or switched by an external stimulus. Hsiao *et al.* reported the electrically switchable lasing emission from the dye-doped H-PDLC transmission gratings.[79] Besides the electric method, the lasing can be also thermally switched. During the

lasing measurement, a heater is used to control the temperature of the samples. The controllable temperature ranges from 20 to 80°C, with an accuracy of about 3°C.
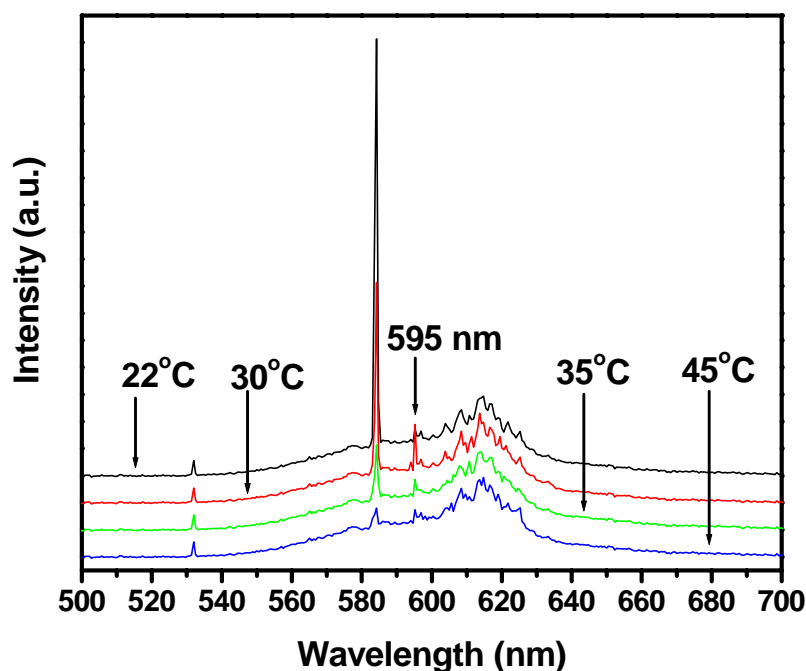
Figure 6.15 The emission spectra from dye-doped H-PDLC gratings at different temperatures.

Figure 6.15 shows the emission spectra from dye-doped H-PDLC gratings using 1# material mixture at various temperatures with a fixed pumping energy of 40 μJ/pulse. From Figure 6.15, we can see that the lasing can be thermally switched. It is interesting to note that at a temperature of 30°C, another lasing peak centered at 595 nm appears in the emission envelope, as shown in Figure 6.15, which means at this temperature a sufficient gain can also be obtained for 595 nm. The switching mechanism of the H-PDLC grating is due to the index modulation of the phase separated LC droplets. Generally, H-PDLC gratings show some anisotropy because there is volume shrinkage during the grating formation,[19,154] which makes the LC droplets anisotropic. With the increase of the temperature, the optical anisotropy lessens and accordingly the effective refractive index of the LC changes and at some

114

temperature, the effective refractive index of the LC matches closely with the refractive index of the polymer matrix. As a result, the lasing emission disappears. Unlike described in Ref. 89 where the lasing wavelength shifted around 5 nm, in our experiments, the effective refractive index changes little and the lasing wavelength has no shift. From Figure 6.15, we can see that, at a temperature of 45°C, both the original and new lasing peaks nearly disappear. After cooling down, the lasing emission appears again.

6.4 Summary

In summary, random lasing and single-mode lasing were demonstrated in dye-doped PDLCs and H-PDLC transmission gratings, respectively. For the random lasing formation in PDLCs, the nanosized LC droplets served as scatterers, which played an important role in closed loop formation. For the dye-doped H-PDLC transmission gratings, the alternating LC-rich lamellae and polymer-rich lamellae formed a DFB structure, which favored single-mode lasing generation. The single-mode lasing action from H-PDLC transmission gratings is the focus of our investigation. Compared to the H-PDLC reflection gratings, the transmission ones have a longer gain length, which helps to lower the pumping threshold. The effect of LC concentration on the lasing properties from H-PDLC transmission gratings was also investigated. With a decrease in LC concentration, the lasing wavelength showed a blue shift, and the FWHM of the lasing peak became narrower.

CHAPTER 7   H-PDLC Photonic Crystals

Photonic crystal (PhCs) are materials with a periodic dielectric distribution that can lead to a range of "forbidden" frequencies that will prevent light of those frequencies from propagating in any direction for any polarization within the material. This range of frequencies, so called photonic bandgap (PBG), is analogous to an electronic bandgap, and indeed arises from a similar mechanism: the presence of a lattice or crystal. In this case, however, the lattice scale is on the order of the wavelength of light (0.1 to 2 μm) rather than on the order of atomic distances. Furthermore, the photonic band structure can be solved exactly through Maxwell's equations.[169]

In many applications, it is very advantageous if some degree of tunability of the PBG can be obtained. The first theoretical consideration of bandgap tuning with electromagnetic fields appeared in 1998, where a 2D lattice was examined in general terms.[170] After one year, Busch and John first explicitly discussed liquid crystals as a potential "active" photonic crystal material.[171]

The existence of PBG, a region in frequency domain where propagating modes are forbidden, in PhCs[172, 173] makes it potentially useful in visible and near infrared (NIR) regions, such as enhancing the brightness of LEDs,[174] fabricating highly integrated waveguides,[175] and filters,[176] etc. Therefore, PhCs hold considerable promise for the emerging generation of nano- and mesoscale optoelectronic components. Different approaches have been used to fabricate PhCs, e.g., electron-beam lithography, [177] self-organization of colloids, [178] layer-by-layer micromachining,[179] and holographic lithography.[180- 184] Generally, a high refractive index contrast is required for a full PBG. However, materials with relatively low

index contrasts, especially for organic materials, can also find utility in applications where the polarization or direction of incident light is limited in some way. Combining numerous desirable characteristics including one-step, fast, large area fabrication, lattice tailoring ability, and easy defect control, holographic photopolymerization offers a highly versatile approach to create organic PBGs.

In this chapter, we used specially designed optical elements to fabricate 2D and 3D H-PDLC PhCs. First, we designed an optical mask with three gratings at 120° relative to one another to fabricate 2D H-PDLC PhCs. In this case, the lattice constant only depends on the grating period. However, large area gratings with small period ($\leq$ 2 μm) are hard to fabricate, which makes the fabrication of PhCs with small lattice constants difficult. Therefore, we then designed a special prism for easy fabrication of H-PDLC PhCs with a smaller lattice constant. These single optical implementation improves the alignment and stability of the optical setup, making it more robust than the multiple beam setups reported previously.

7.1 2D H-PDLC PhCs

In this section, we introduce an easy method to fabricate 2D H-PDLC PhCs using only a single diffraction element and a photomask to create a three-beam interference pattern. The mask is comprised of three diffraction gratings at 120° relative to one another.

7.1.1 Fabrication

The materials used consisted of 48 wt% monomer, TMPTA, 8 wt% cross-linking monomer, NVP, 0.8 wt% photoinitiator, RB, 1.2 wt% coinitiator, NPG, 8 wt% surfactant, OA, and 34 wt% liquid crystal, E7. The detailed material processing for fabrication was reported previously.

117
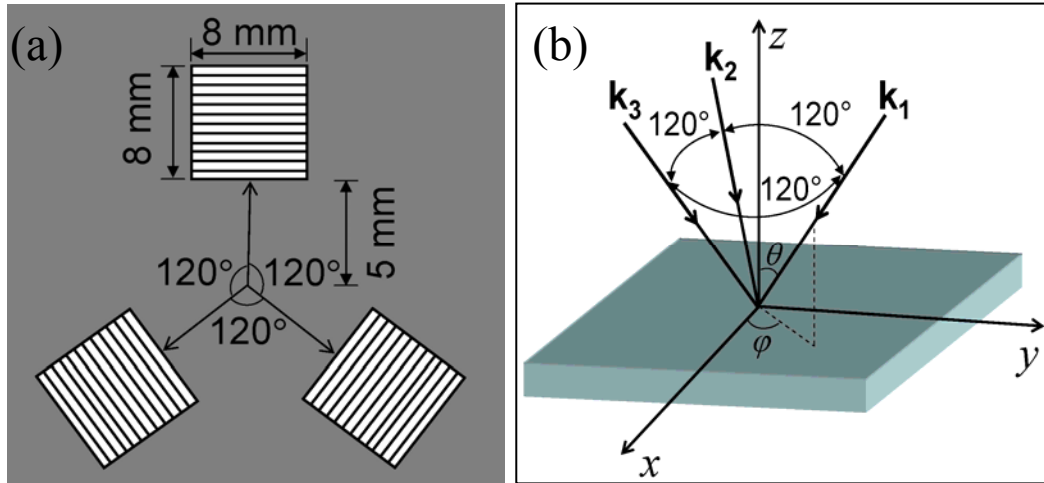
Figure 7.1 Schematic of the mask (a) and three first order diffracted beams (b).

When a collimated Ar^+ laser beam impinges on the mask, which produces three diffracted beams, a diffraction pattern will be produced at their intersection region. In our experiment, each grating on the mask has an area of 8×8 mm^2 and the grating period is 4 μm. Figure 7.1(a) and (b) show the schematic of the mask and three diffracted beams. A cell filled with the LC/prepolymer mixture is exposed to the diffraction pattern. The LC and polymer will redistribute because of the polymerization of the prepolymer induced by the light intensity, thus forming a 2D structure inside the cell.

7.1.2 Simulation

The electrical field distribution of multi-beam interference can be generally described by

$$I(\boldsymbol{r}) = \left[\sum_{j=1}^{n} \boldsymbol{E}_j(\boldsymbol{r}) \exp(i\boldsymbol{k} \cdot \boldsymbol{r} + i\phi_j) \right]\left[\sum_{j=1}^{n} \boldsymbol{E}_j^*(\boldsymbol{r}) \exp(-i\boldsymbol{k} \cdot \boldsymbol{r} + i\phi_j) \right]$$

$$= \sum_{j=1}^{n} \left| \boldsymbol{E}_j \right|^2 + \sum_{i \neq j}^{n} \boldsymbol{E}_i \cdot \boldsymbol{E}_j^* \exp\left[i(\boldsymbol{k}_i - \boldsymbol{k}_j) \cdot \boldsymbol{r} + i\phi_{ij} \right],$$

(7.1)

where E is the amplitude, k is the wave vector, i and j are integers, ϕ_{ij} is the initial phase difference between two incident waves, and r is the position vector. All fourteen Bravais lattices can be fabricated by recording four plane wave interference fringes.[183]

In our experiment, the orientation of the wave vector of the three beams can be defined as:

$$\hat{k}_1 = \sin\theta\cos\varphi_1\hat{e}_x + \sin\theta\sin\varphi_1\hat{e}_y + \cos\theta\hat{e}_z \tag{7.2}$$

$$\hat{k}_2 = \sin\theta\cos\varphi_2\hat{e}_x + \sin\theta\sin\varphi_2\hat{e}_y + \cos\theta\hat{e}_z \tag{7.3}$$

$$\hat{k}_3 = \sin\theta\cos\varphi_3\hat{e}_x + \sin\theta\sin\varphi_3\hat{e}_y + \cos\theta\hat{e}_z , \tag{7.4}$$

where, $\hat{k}$ is unit wave vector, $\hat{e}$ is unit coordinate vector, θ is the angle between the laser beam and z-axis, which equals the first order diffraction angle, and φ is the angle between the projection of the laser beam on the x-y plane and the x-axis (see Figure 7.1). Substituting Eq. (7.2) - (7.4) into (7.1) with $\theta = 7.4°$, $\varphi_1 = 180°$, $\varphi_2 = -60°$, and $\varphi_3 = 60°$, we have

$$\begin{aligned}
I &= (E_1 + E_2 + E_3)\cdot(E_1 + E_2 + E_3)^* \\
&= |E_1|^2 + |E_2|^2 + |E_3|^2 \\
&\quad + 2E_1\cdot E_2\cos(-\frac{3}{2}kx\sin\theta + \frac{\sqrt{3}}{2}ky\sin\theta) \\
&\quad + 2E_1\cdot E_3\cos(-\frac{3}{2}kx\sin\theta - \frac{\sqrt{3}}{2}ky\sin\theta) \\
&\quad + 2E_2\cdot E_3\cos(\sqrt{3}ky\sin\theta)
\end{aligned} \tag{7.5}$$

The simulated 3D interference pattern is shown in Figure 7.2. It is worth mentioning that the period of this triangular lattice is equal to two thirds of the diffraction grating period, i.e. 2.67 μm, which does not depend on the beam wavelength.[185] Therefore, the PBGs can be easily engineered by changing the grating period.
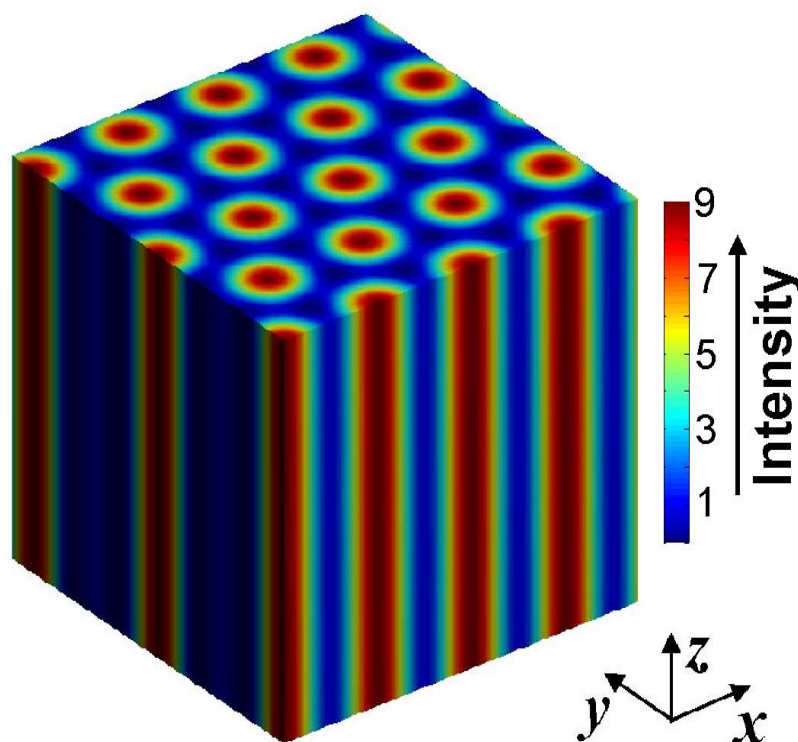
Figure 7.2 Simulated 3D interference pattern. The color bar shows the intensity distribution.

7.1.3 Results and Discussion

Figure 7.3(a) shows an AFM image of the surface, which was obtained after the liquid crystals were removed in ethanol. It reveals a clear hexagonal morphology with a lattice constant of about 2.5 μm, which is in good agreement with the simulation pattern (Figure 7.2), considering the general 5 - 10 % volume shrinkage for the acrylate monomer during the photo-induced polymerization.[19,89] It is interesting to note in Figure 7.3(a), in a hexagonal cell, the height of the central point is slightly different from its surrounding six points, which are almost the same in height. Figure 7.3(b) shows the surface morphologies of the 2D H-PDLC PhCs observed under a high resolution optical microscope (HiROX). The inset SEM image in Figure 7.3(b)

120

shows the cross section morphology of the sample, where columnar structure is clearly seen, which matches the simulation result in Figure 7.2.
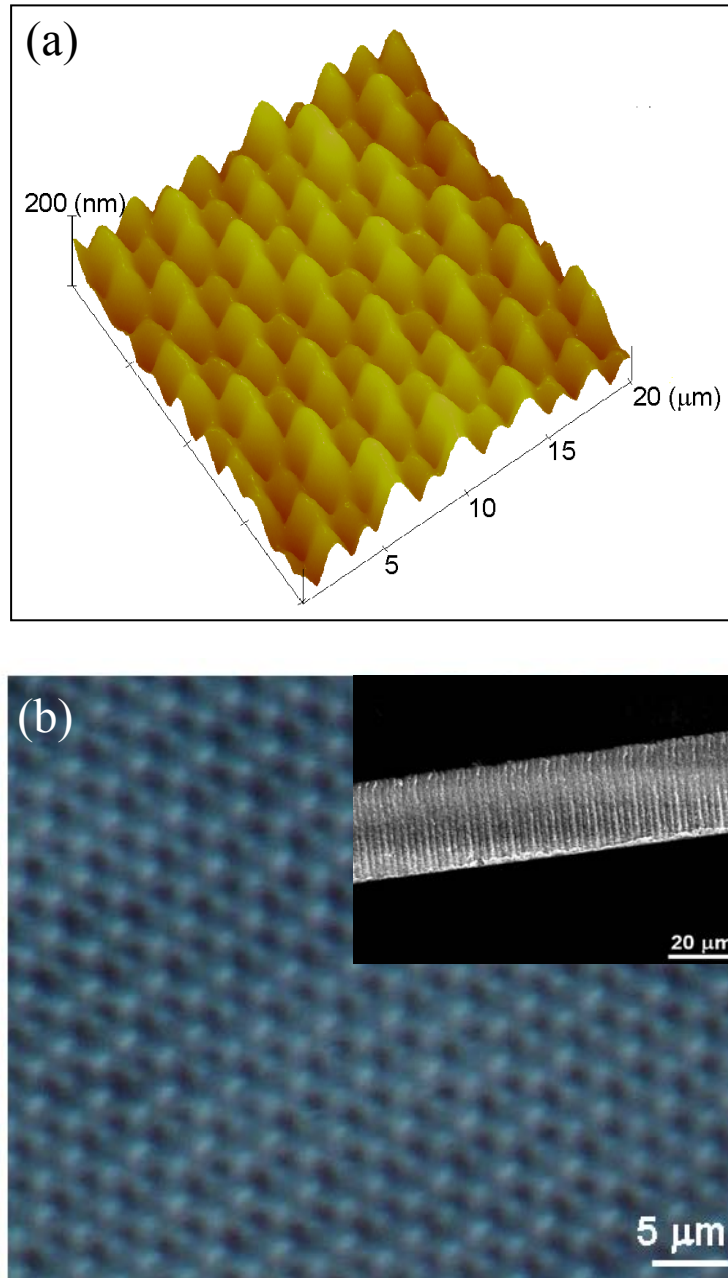
Figure 7.3 AFM (a) and optical microscopy (b) images showing the surface morphology of the 2D H-PDLC PhC and SEM image [the inset of (b)] showing the cross section morphology.

The diffraction patterns of the H-PDLC PhC were checked to confirm the quasi-crystal structure. Figure 7.4(a) and (b) show the visible diffraction pattern produced by a normally incident He-Ne laser beam operating at 543 nm and a collimated broadband white beam for our sample. From Figure 7.4(a), we can see clear hexagonal diffraction spots which match well with our AFM, optical, and SEM images of a 2D hexagonal lattice (Figure 7.3). The diffracted spots originating from ($0\ 1\ \bar{1}$) and ($1\ 1\ \bar{2}$) surfaces are labeled in Figure 7.4(a).[186] The images clearly reveal the presence of quasiperiodicity within the sample. The observed points are sharp and symmetrically distributed. As reported by Gorkhali *et al.*,[88] all diffraction points in the first and higher orders should show an *N*-fold symmetry and have 2*N* diffracted points, where *N* is the number of interference beams used to produce the PhC. For our case, *N* = 3, in good agreement with the prediction, we can clearly see a 3-fold symmetry and 6 diffracted points for the same order of diffracted beams.
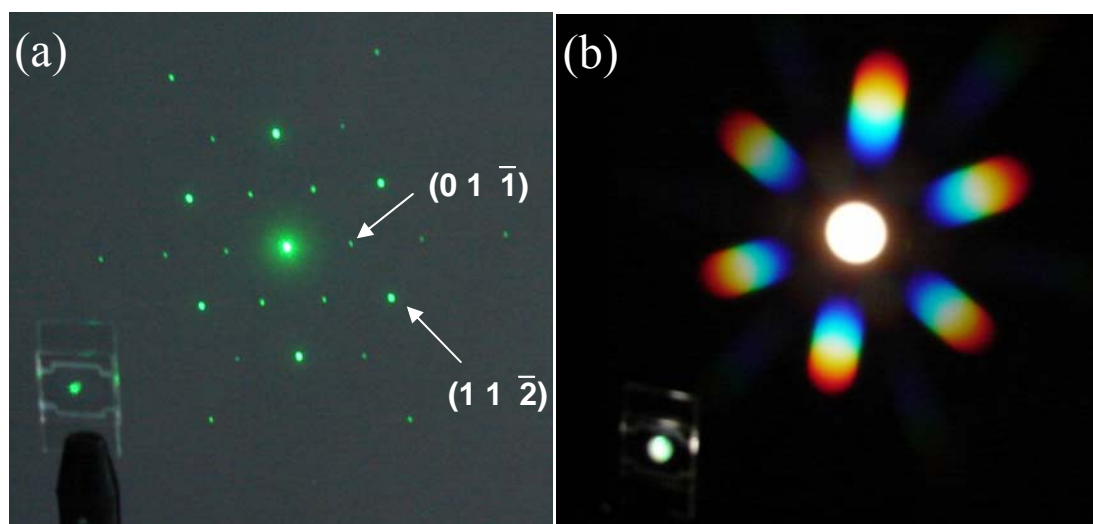
Figure 7.4 Visible diffraction patterns of the H-PDLC PhCs produced by a normally incident He-Ne laser beam (a) and a collimated broadband white beam (b).
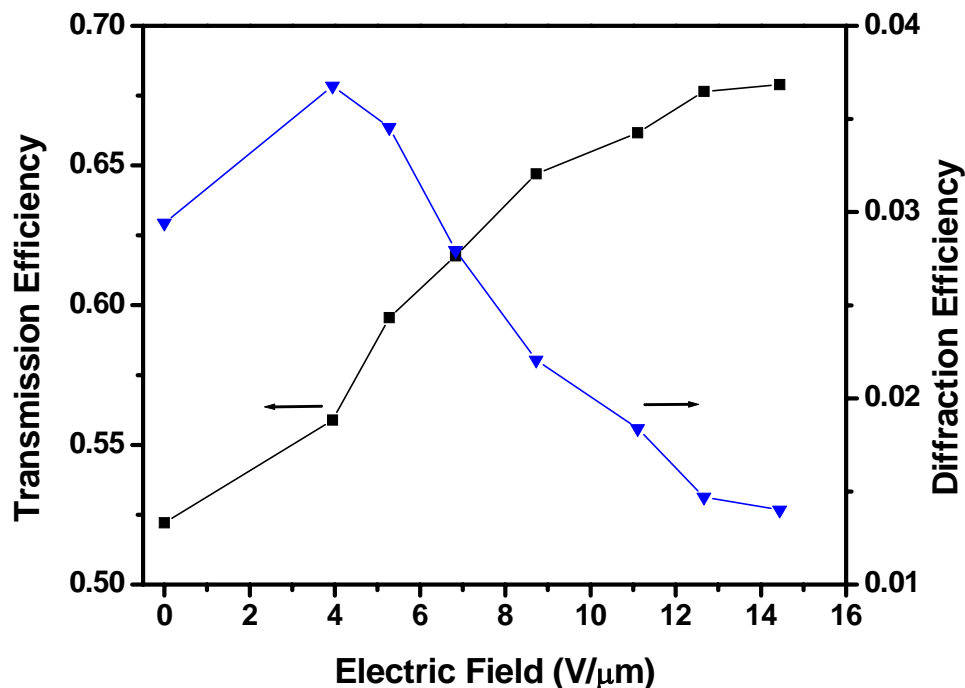
Figure 7.5 (1 1 $\overline{2}$) diffraction efficiency and nondiffracted center beam transmission efficiency changes as functions of the applied voltage.

For the H-PDLC PhCs, a distinct advantage is that they can be tuned by applying a voltage, i.e. the PBGs of H-PDLC PhCs can be changed dynamically. Figure 7.5 shows the changes of the (1 1 $\overline{2}$) diffraction efficiency and transmission efficiency (center beam without diffraction) as functions of the applied voltage. The definitions of diffraction and transmission efficiency can be found in Ref. 124. From Figure 7.5, we can see that, with the increase of applied voltage, the (1 1 $\overline{2}$) diffraction efficiency first increases and then decreases, while the transmission efficiency increases, due to the refractive indices matching between the LC and polymer matrix. Optical clearing, originating from droplet size distribution, may be the possible reason for the initial increase in diffraction efficiency. In H-PDLC PhCs, large liquid crystal droplets tend to scatter more light, producing a haze effect. When an electric field is applied on the sample, these large droplets will align first due to the

larger volume to surface area ratio, and the haze will disappear, thus, resulting in the diffraction efficiency increase initially. When the electric field continues to increase, the smaller droplets start to align, and the index modulation decreases. As a result, the diffraction efficiency will decrease. The $(1\ 1\ \bar{2})$ diffraction efficiency reduces to half its zero field value with an applied field of 14.5 V/μm (Figure 7.5). Obviously, energy transfer from the higher order diffraction to the lower order diffraction occurs as the higher order diffraction spots gradually disappear with the increase of applied voltage.

7.2   3D H-PDLC PhCs

In the above section, we have demonstrated 2D H-PDLC PhCs with the lattice constant of 2.5 μm using only a photomask. However, the resulting lattice constant (determined by the grating period on the photomask) in the PhC structures is relatively large, which greatly limits its applications, especially in the visible and NIR range. Due to the technical limitation, it is not easy to fabricate large area photomasks with small grating periods such as 1 μm or 2 μm. To make such PhCs applicable in visible or NIR range, PhC structures with submicron- and nano-size lattice constants are desired. In this section, we shall report a one-step fabrication of 3D H-PDLC PhCs with the smaller lattice constant of 420 nm using a specially designed prism, which creates a four-beam interference pattern.

7.2.1 Experimental

The starting LC/prepolymer mixture used was consisted of 34.8 wt% TMPTA, 8.5 wt% NVP, 0.7 wt% RB, 1.0 wt% NPG, 7.7 wt% OA, and 47.3 wt% LC E7. A droplet of the mixture was sandwiched between two pieces of ITO coated glass. The cell gap was about 30 μm. The exposure time was about 120 s. After exposure, the samples were further cured for 5 minutes using a UV lamp to ensure complete

polymerization of the prepolymer. For morphology observation, the tested sample was immersed in liquid nitrogen for easy cleaving and then soaked in ethanol for at least 12 h to remove LC. After drying, the morphology was examined by AFM and SEM, respectively. To measure the response time, a laser beam from a He-Ne laser operating at 543 nm was normally incident on the sample, and the diffraction was detected by a photodetector. A square waveform voltage from a high voltage amplifier/function generator was applied to the sample. During the measurement, the photodetector and voltage signals were fed into two different channels of an oscilloscope. From the waveforms captured by the oscilloscope, the rise and fall times were extracted.
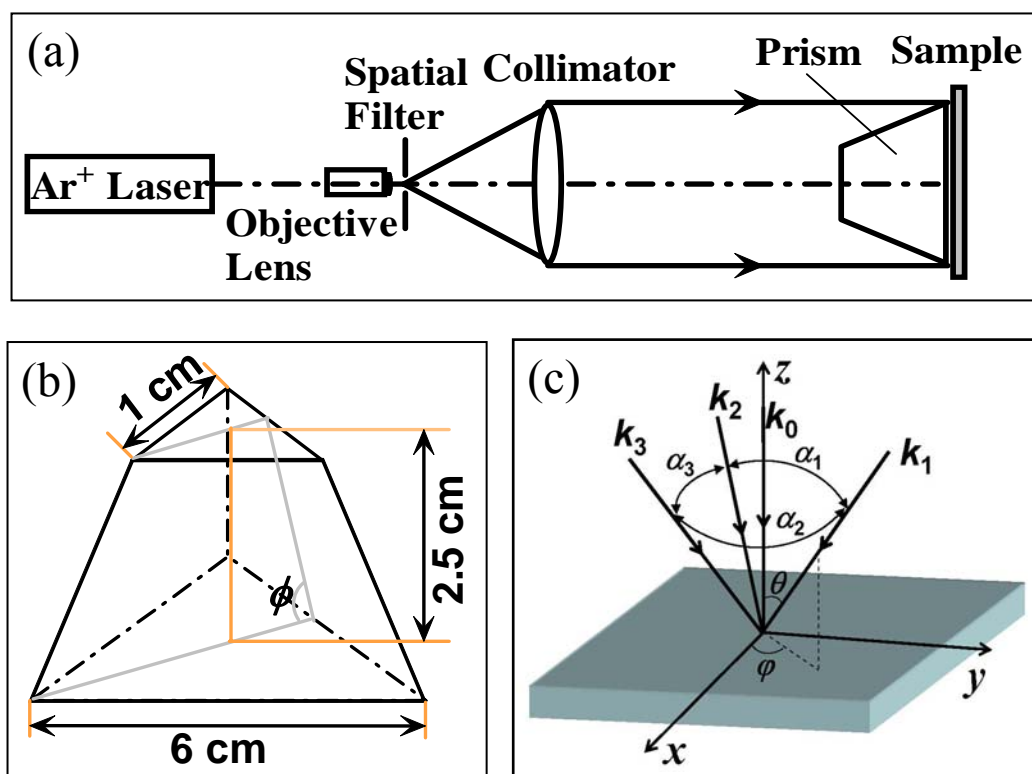
Figure 7.6 Schematic of the optical setup, (a), specially designed prism, (b), and four-beam interference configuration, (c).

The optical setup for the fabrication is schematically illustrated in Figure 7.6(a). A laser beam is collimated first and then impinges normally onto the specially designed prism [Figure 7.6(b)], which is made of BK7 glass. The side lengths of the top- and bottom-surfaces (isosceles triangle) are 1 and 6 cm, respectively, and the height is 2.5 cm. Emerging from the prism are one directly transmitted beam k_0 in the center and three side beams, k_1, k_2, and k_3, by the refraction from three tilted side surfaces of the prism, as shown in Figure 7.6(c). These four beams overlap at the bottom surface of the prism and interfere with each other. A cell filled with the LC/prepolymer mixture is attached onto the center of the bottom surface using an index-matched liquid to record the interference pattern. During the recording process, monomers polymerize first in the area with higher exposure intensity. As a result, spatial gradients in chemical potential are established, which produces a diffusion of monomers (and other reactants) into the high intensity regions, and a counter-diffusion of LCs into the low intensity regions. Finally, a 3D structure is formed inside the cell. The use of a single prism in the fabrication setups leads to multiple beam generation and interference at the same time, and thus decreases the complexity of the alignment of the optics. More importantly, the setup is self-adaptive, i.e. the effect of the external vibration during the fabrication process is minimized.

Similar to the description of the beam vectors in the above section, the beam vectors of the four beams generated by the prism can be written as:

$$\hat{k}_0 = \hat{e}_z \tag{7.6}$$

$$\hat{k}_1 = \sin\theta\cos\varphi_1\hat{e}_x + \sin\theta\sin\varphi_1\hat{e}_y + \cos\theta\hat{e}_z \tag{7.7}$$

$$\hat{k}_2 = \sin\theta\cos\varphi_2\hat{e}_x + \sin\theta\sin\varphi_2\hat{e}_y + \cos\theta\hat{e}_z \tag{7.8}$$

$$\hat{k}_3 = \sin\theta\cos\varphi_3\hat{e}_x + \sin\theta\sin\varphi_3\hat{e}_y + \cos\theta\hat{e}_z, \tag{7.9}$$

where, $\hat{k}$ is unit wave vector, $\hat{e}$ is unit coordinate vector, θ is the angle between the three refracted laser beams and z-axis, which is determined by the cutting angle of the prism, ϕ, and φ is the angle between the projection of laser beam on x-y plane and x-axis (Figure 7.6). The resulting spatial distribution of the interference pattern is determined by the angles: θ, α_1, α_2, and α_3. In this paper, α_1, α_2, and α_3 are fixed at 120° and the cutting angle ϕ for the prism is 60°. Substituting Eq. (7.6)-(7.9) into (7.1) with $\varphi_1 = 180°$, $\varphi_2 = -60°$, and $\varphi_3 = 60°$, we have

$$
\begin{aligned}
I &= (\boldsymbol{E}_0 + \boldsymbol{E}_1 + \boldsymbol{E}_2 + \boldsymbol{E}_3) \cdot (\boldsymbol{E}_0 + \boldsymbol{E}_1 + \boldsymbol{E}_2 + \boldsymbol{E}_3)^* \\
&= |\boldsymbol{E}_0|^2 + |\boldsymbol{E}_1|^2 + |\boldsymbol{E}_2|^2 + |\boldsymbol{E}_3|^2 \\
&\quad + 2\boldsymbol{E}_0 \cdot \boldsymbol{E}_1 \cos(kx\sin\theta + kz - kz\cos\theta) \\
&\quad + 2\boldsymbol{E}_0 \cdot \boldsymbol{E}_2 \cos(-\frac{1}{2}kx\sin\theta + \frac{\sqrt{3}}{2}ky\sin\theta + kz - kz\cos\theta) \\
&\quad + 2\boldsymbol{E}_0 \cdot \boldsymbol{E}_3 \cos(-\frac{1}{2}kx\sin\theta - \frac{\sqrt{3}}{2}ky\sin\theta + kz - kz\cos\theta) \\
&\quad + 2\boldsymbol{E}_1 \cdot \boldsymbol{E}_2 \cos(-\frac{3}{2}kx\sin\theta + \frac{\sqrt{3}}{2}ky\sin\theta) \\
&\quad + 2\boldsymbol{E}_1 \cdot \boldsymbol{E}_3 \cos(-\frac{3}{2}kx\sin\theta - \frac{\sqrt{3}}{2}ky\sin\theta) \\
&\quad + 2\boldsymbol{E}_2 \cdot \boldsymbol{E}_3 \cos(\sqrt{3}ky\sin\theta).
\end{aligned}
\tag{7.10}
$$

From Eq. (7.10), the periods a, b, and c along the x, y, and z directions depend on the angle θ

$$
a = \frac{\lambda_w}{\sqrt{3}n_{eff}\sin\theta}
\tag{7.11}
$$

$$
b = \frac{\lambda_w}{n_{eff}\sin\theta}
\tag{7.12}
$$

$$
c = \frac{\lambda_w}{2n_{eff}(1-\cos\theta)},
\tag{7.13}
$$

where λ_w is the writing wavelength, and n_{eff} is the effective refractive index of the recording materials. In our experiment, $\lambda_w = 514.5$ nm, assuming $n_{eff} = 1.59$ according

to the LC concentration in the homogeneous PDLCs, $\theta = 24.1°$, we can theoretically obtain $a = 458$ nm, $b = 792$ nm, and $c = 1856$ nm.

With the 4-beam intensity ratio of 3:1:1:1 estimated, Figure 7.7 shows the theoretically calculated 3D pattern of the spatial intensity distribution of the four-beam interference. Therefore, the PBGs can be easily engineered by changing the cutting angle of the prism.
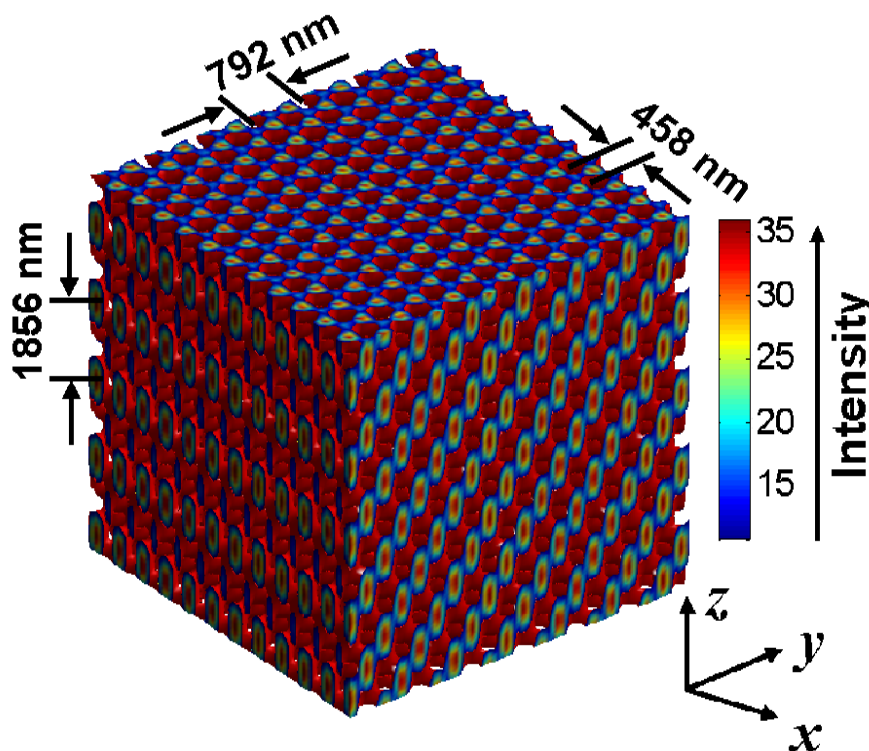
Figure 7.7 Simulated 3D interference pattern. The color bar shows the

light intensity distribution.

7.2.2 Results and Discussion

In our experiment, the intensities of the four beams k_0, k_1, k_2, and k_3 are 58, 21, 22, and 21 mW/cm^2, respectively, which is very close to the estimated ratio. Figure 7.8(a) and (b) show the AFM images of the surface morphologies with different scanning areas of 10×10 μm^2 and 4×4 μm^2 respectively. Figure 7.9(a) and

(b) show the SEM images of the surface and the cross section for the sample respectively, which are in good agreement with the simulation pattern. It can be seen from Figure 7.9 that the surface structure is a triangular lattice with a lattice constant of about 420 ±20 nm, which is in good agreement with the theoretical calculation according to the geometrical structure (Figure 7.6), considering the general 5 - 10% volume shrinkage for acrylate monomers during photopolymerization.[19,89]
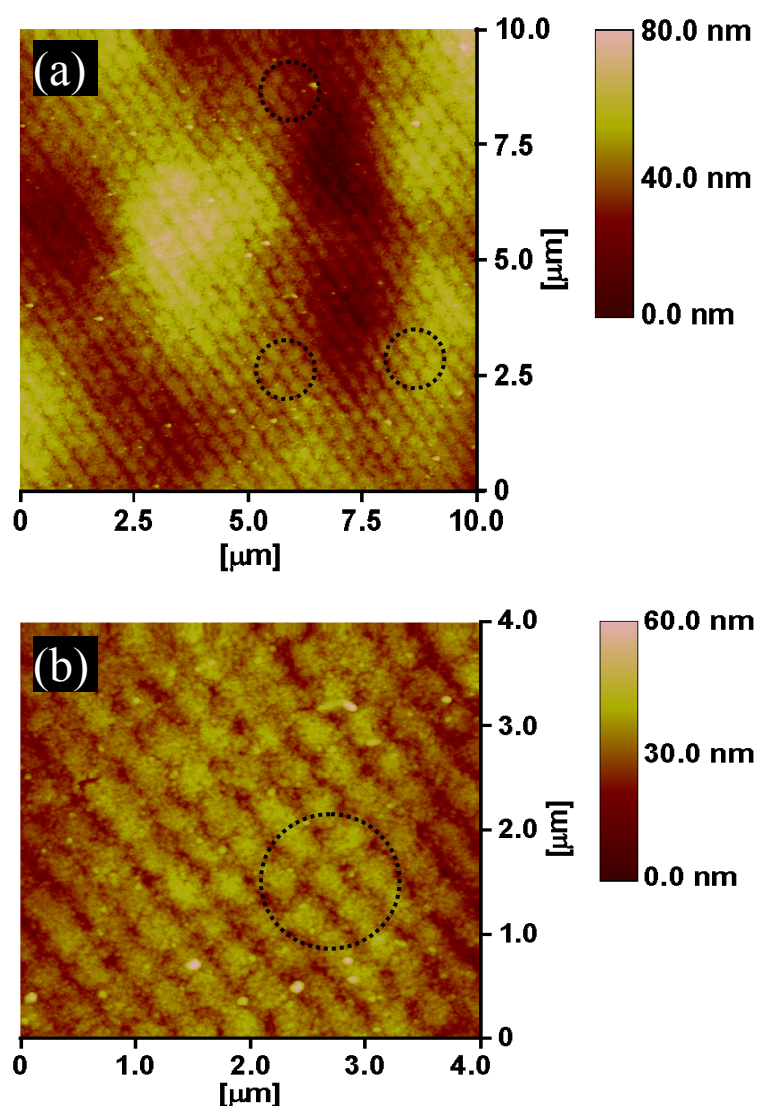
Figure 7.8 Surface AFM images of the 3D H-PDLC PhC sample in area of (a) 10 × 10 μm^2 and (b) 4 × 4 μm^2. The hexagonal structures are indicated in the dashed circles.
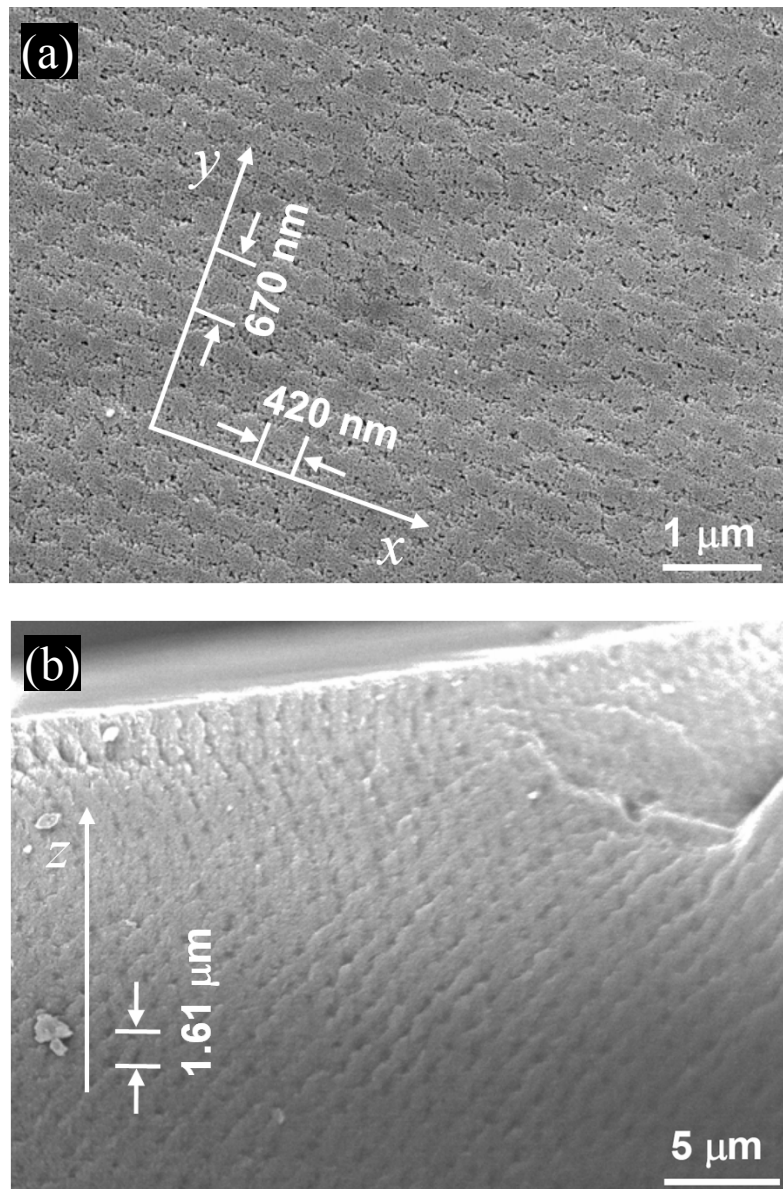
Figure 7.9 SEM images of the surface (a) and cross section (b) of 3D H-PDLC PhC sample.

Figure 7.10(a) and (b) show the visible diffraction pattern produced by a normally incident He-Ne laser beam operating at 543 nm and a broadband white beam for our H-PDLC PhC sample fabricated. From Figure 7.10(a), we can see that three diffracted points are reconstructed when a laser beam is normally incident on the sample. It is worth mentioning that the three ellipse light spots in Figure 7.10(a) are induced by the edges of the top surface of the prism. A Kossel ring is also observed in

the center of the diffraction pattern, which may be caused by the interference between the impinging four beams and the scattered light. Due to a decreased lattice constant, the white light diffraction exhibits a much larger dispersion [Figure 7.10(b)] compared to that of the 2D H-PDLC PhCs [Figure 7.4(b)].
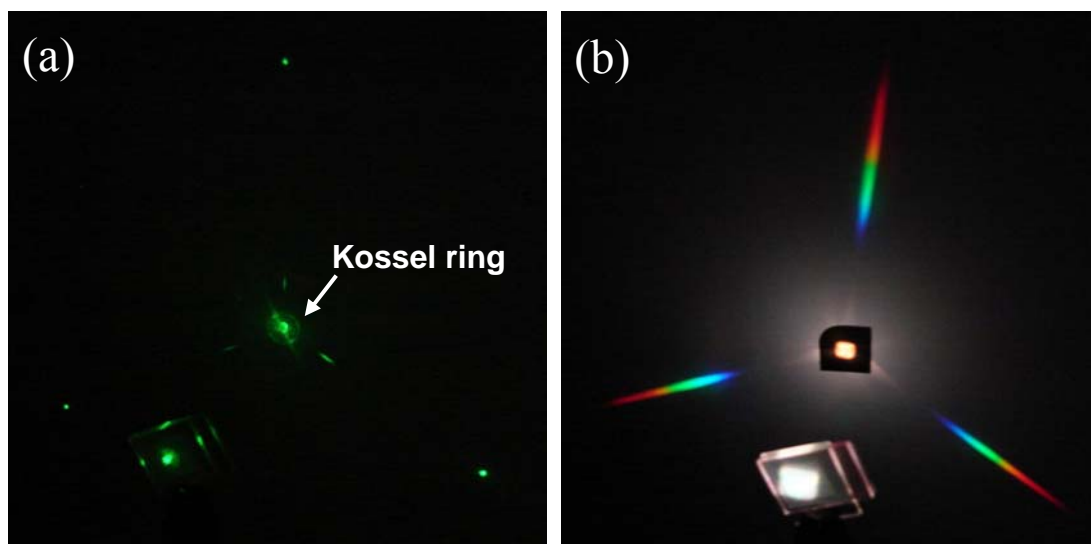
Figure 7.10 Diffraction patterns of the H-PDLC PhCs produced by (a) a normally incident He-Ne laser beam, and (b) a broadband white beam.
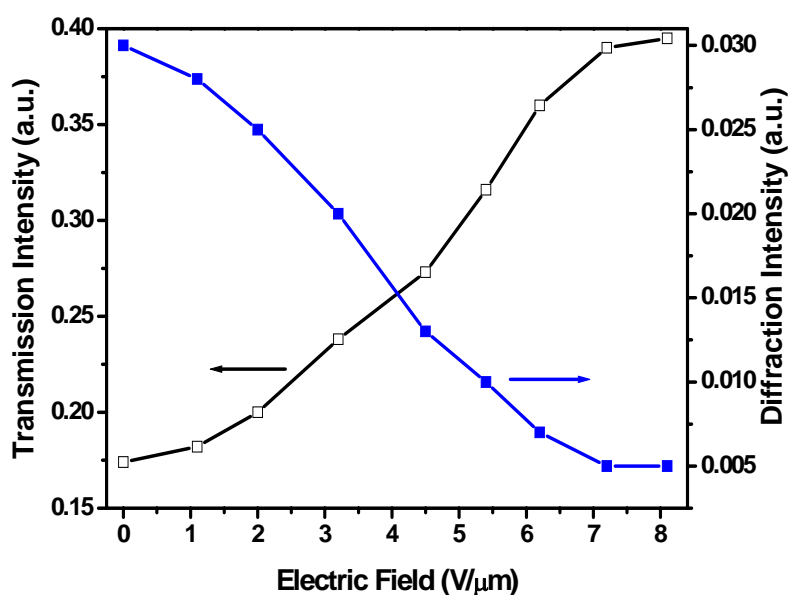
Figure 7.11 Diffraction and transmission intensities change as functions of applied voltage.

Figure 7.11 shows the changes of the diffraction and the transmission intensity as functions of applied voltage. From Figure 7.11, we can see that, with the increase of applied voltage, the diffraction intensity decreases, while the transmission intensity increases, due to the refractive indices matching between the liquid crystal and polymer matrix. The threshold electric field is about 1.0 V/μm and the switching electric field is about 7.2 V/μm. Due to the large LC concentration used in our experiment, the driving voltage decreases a great deal compared to the low LC concentration case reported previously.[124]

Figure 7.12 shows the measured electro-optical response time when the sample was driven by a square voltage of 185 V_{rms} (6.2 V/μm) with a frequency of 20 Hz. From Figure 7.12, the rise time (10%–90% intensity changed) and the fall time (90%–10% intensity changed), are about 1.75 and 1.09 ms, respectively. The response time is relatively slow due to the large LC concentration. With a decrease in the LC concentration, the response time can be expected to be smaller.
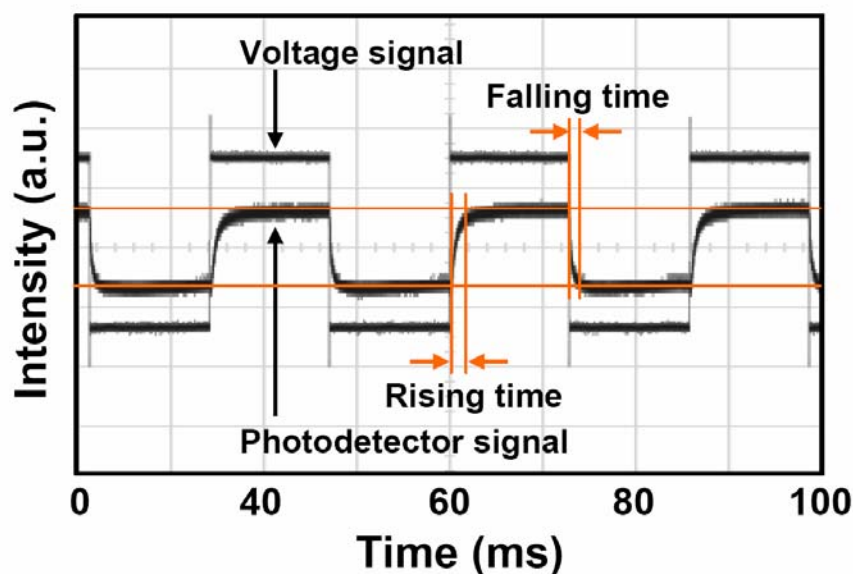
Figure 7.12 Electro-optical response time measurement of 3D H-PDLC PhC sample.

132

7.3 Summary

In summary, electrically switchable 2D and 3D H-PDLC PhCs were successfully fabricated using a specially designed photomask and prism, respectively. With these methods, the H-PDLC PhCs with different lattice constants can be realized. Such a method offers a single-step, easy fabrication and low cost method compared with conventional lithography. The PhC structures can be easily engineered by designing the grating period for the photomask or designing the cutting angle for the prism. However, due to the low refractive index contrast between the polymer and liquid crystal, such kinds of H-PDLC PhCs can not show complete PBGs, which limits the applications to some extent.

CHAPTER 8   Conclusions and Recommendations for Future Works

8.1   Conclusions

In this thesis, we have focused on developing some new devices based on H-PDLC and PDLC. In particular, a polarization insensitive 2×2 optical switch was demonstrated based on a H-PDLC Bragg transmission grating. Using a glass fly's-eye lens as a photomask, a PDLC fly's-eye lens was fabricated. A specially designed CGH was also recorded in PDLC. The major advantages of these devices are easy fabrication process, compactness, light weight, and low cost. Moreover, they are flat devices and electrically tunable. These properties make them potentially useful in many fields, such as optical communications, illumination systems, and information storage.

On the other hand, the 1D H-PDLC grating can be also considered as a 1D PhC. In this thesis, we demonstrated optically pumped and thermally switchable DFB lasers from a dye-doped H-PDLC transmission grating structure. Two different lasing dyes were used to investigate the lasing in detail. We also found that the LC concentration played an important role in both attaining the lasing and selecting the lasing wavelength, because different LC concentrations induced different PBGs in H-PDLC transmission gratings. By varying LC concentrations, different lasing wavelengths from 580 nm to 630 nm were achieved.

Besides 1D PhCs, 2D and 3D H-PDLC PhCs were also fabricated using a single diffractive element and a specially designed prism, respectively. These methods improve the alignment and stability of the optical setup, making it more robust than the multiple beam setups implemented previously.

8.2   Recommendations for Future Work

8.2.1 The Recipe Optimization

In this thesis, we have demonstrated various optical devices based on H-PDLC materials and experimentally optimized the material recipe. However, for specific applications of these optical devices, the performance of these devices can be further improved by changing the material recipe. Therefore, it is necessary to further optimize the material recipe.

8.2.2 PhC Lasers

By doping a lasing dye into the H-PDLC materials, lasing emission has already been demonstrated from a 1D structure. However, most of the research is focused on the 1D structure. Generally, 2D and 3D PhCs can create stronger coupled electromagnetic bands that lead to low group velocity dispersion and consequently local field enhancement compared to 1D case.[89] Therefore, it is easily anticipated that the lasing properties can be improved significantly if dye-doped 2D and 3D H-PDLC structures can be obtained. We have demonstrated the 2D and 3D H-PDLC PhC structures with different lattice constants in Chapter 7. Therefore, this opens an easy method to fabricate 2D and 3D PhC lasers based on H-PDLC.

8.2.3 Nanoparticle-doped H-PDLC

As we pointed out in this thesis, due to the low refractive index contrast between the polymer and liquid crystal, H-PDLC PhCs can not show complete PBGs, which limits the applications to some extent. On the other hand, the index contrast also influences the diffraction efficiency of H-PDLC gratings. To extend H-PDLC applications, it is desirable to obtain a higher index contrast. Doping nanoparticles with high refractive index into PDLC materials may be an easy and effective way to

realize higher index contrast. Some researchers have successfully demonstrated nanoparticle patterning, i.e. holographic gratings, in nanoparticle-dispersed photopolymers using a holography technique.[187-191] In the nanoparticle-doped PDLC materials, it is anticipated that the nanoparticles will diffuse into the LC-rich regions during the phase separation between the polymer and LC. Therefore, the index contrast can be increased by this way.

8.2.4 Polymer Structures as Templates

After removing the LC in the H-PDLC structures, we can obtain a perfect porous polymer structures. Such polymer structures have been shown to be useful in sensing applications.[92] On the other hand, researchers have successfully duplicated natural structures like butterfly wings, where the butterfly wings were used as a template.[192] With better periodic structures, it is promising to use the porous polymer structures as templates to grow some useful materials for photonic applications.

Author's Publications

Journal Paper

1. ***Y. J. Liu***, X. W. Sun, J. H. Liu, H. T. Dai, and K. S. Xu, "A polarization insensitive 2 × 2 optical switch fabricated by liquid crystal-polymer composites," *Appl. Phys. Lett.* **86**, 041115 (2005).

2. ***Y. J. Liu***, X. W. Sun, H. T. Dai, J. H. Liu, and K. S. Xu, "Effect of surfactant on electro-optical properties of holographic polymer dispersed liquid crystal Bragg gratings," *Opt. Mater.* **27**, 1451-1455 (2005).

3. ***Y. J. Liu***, X. W. Sun, and Q. Wang, "A focus-switchable lens made of polymer-liquid crystal composite," *J. Crys. Growth* **288**, 192-194 (2006).

4. ***Y. J. Liu***, X. W. Sun, P. Shum, H. P. Li, J. Mi, W. Ji, and X. H. Zhang, "Low-threshold and narrow-linewidth lasing from dye-doped holographic polymer-dispersed liquid crystal transmission gratings," *Appl. Phys. Lett.* **88**, 061107 (2006).

5. ***Y. J. Liu***, X. W. Sun, P. Shum, X. H. Zhang, H. P. Li, J. Mi, and W. Ji, "Lasing from a one-dimensional photonic crystal made of dye-doped holographic polymer-dispersed liquid crystal gratings," *Jpn. J. Appl. Phys.* **45**, L559 - L561 (2006).

6. ***Y. J. Liu***, X. W. Sun, H. I. Elim, and W. Ji, "Gain narrowing and random lasing from dye-doped polymer-dispersed liquid crystals with nanoscale liquid crystal droplets," *Appl. Phys. Lett.* **89**, 011111 (2006).

7. ***Y. J. Liu***, X. W. Sun, P. Shum, and X. J. Yin, "Tunable fly's-eye lens made of patterned polymer-dispersed liquid crystal," *Opt. Express* **14**, 5634-5640

(2006). Also selected in *The Virtual Journal for Biomedical Optics* **1**(7), (2006).

8. ***Y. J. Liu*** and X. W. Sun, "Electrically tunable two-dimensional holographic photonic crystal fabricated by a single diffractive element," *Appl. Phys. Lett.* **89**, 171101 (2006). Also selected in *Virtual Journal of Nanoscale Science & Technology* **14**(19), (2006).

9. ***Y. J. Liu***, X. W. Sun, H. I. Elim, and W. Ji, "Effect of liquid crystal concentration on the lasing properties of dye-doped holographic polymer-dispersed liquid crystal transmission gratings," *Appl. Phys. Lett.* **90**, 011109 (2007).

10. ***Y. J. Liu*** and X. W. Sun, "Electrically switchable computer-generated hologram recorded in polymer-dispersed liquid crystals," *Appl. Phys. Lett.* **90**, 191118 (2007).

11. ***Y. J. Liu*** and X. W. Sun, "Electrically tunable three-dimensional holographic photonic crystal made of polymer-dispersed liquid crystal," *Jpn. J. Appl. Phys.*, in press.

Conference Paper

12 ***Y. J. Liu***, X. W. Sun, H. T. Dai, and K. S. Xu, "Electro-optical characteristics of holographic polymer dispersed liquid crystal Bragg gratings," *SID Symposium Digest* **36**, 682-685 (2005).

13 ***Y. J. Liu***, X. W. Sun, and Q. Wang, "A Focus-switchable Lens made of Polymer-Liquid Crystal Composite," *3rd International Conference on Materials for Advanced Technologies (ICMAT 2005)*, Singapore, Jul 3-8, 2005.

14 ***Y. J. Liu*** and X. W. Sun, "Fabrication and Characterization of Holographic Polymer Dispersed Liquid Crystal Bragg Gratings," *NanoSingapore 2006:*

IEEE Conference on Emerging Technologies - Nanoelectronics, Singapore, Jan 10-13, 2006.

15   **_Y. J. Liu_** and X. W. Sun, "A fly's-eye lens fabricated using patterned polymer dispersed liquid crystal," *SID Symposium Digest* **37**, 776-779 (2006).

16   **_Y. J. Liu_** and X. W. Sun, "Electrically tunable square-zone Fresnel lens made of polymer-separated composite film," *Asia Display'07*, Shanghai, China, Mar 12-16, 2007.

Bibliography

[1] C. W. Oseen, "Theory of liquid crystals," *Trans. Faraday Soc.* **29**, 883-899 (1933).

[2] F. C. Fran, "On the theory of liquid crystals," *Disc. Faraday Soc.* **25**, 19-28 (1958).

[3] S. L. Rosen, "Fundamental principles of polymeric materials," John Wiley & Sons, New York, 1993.

[4] R. A. M. Hikmet, "Electrically induced light scattering from anisotropic gels," *J. Appl. Phys.* **68**, 4406-4412 (1990).

[5] D. -K. Yang, L. -C. Chien, and J. W. Doane, "Cholesteric liquid crystal/polymer dispersion for haze-free light shutters," *Appl. Phys. Lett.* **60**, 3102-3104 (1992).

[6] J. L. Fergason, "Polymer encapsulated nematic liquid crystals for display and light control applications," *SID Inter. Symp. Dig. Tech. Papers* **16**, 68-69 (1985).

[7] P. S. Drzaic, "Polymer dispersed nematic liquid crystal for large area displays and light valves," *J. Appl. Phys.* **60**, 2142-2148 (1986).

[8] J. W. Doane, N. A. Vaz, B. G. Wu, and S. Zumer, "Field controlled light scattering from nematic microdroplets," *Appl. Phys. Lett.* **48**, 269-271 (1986).

[9] N. A. Vaz, G. W. Smith, and G. P. Montgomery, "A light control film composed of liquid crystal droplets dispersed in a UV-curable polymer," *Mol. Cryst. Liq. Cryst.* **146**, 1-15 (1987).

[10] J. L. West, "Phase separation of liquid crystals in polymers," *Mol. Cryst. Liq. Cryst.* **157**, 427-441 (1988).

[11] F. G. Yamagishi, L. J. Miller, and C. I. Van Ast, "Morphological control in polymer-dispersed liquid crystal film matrices," *Proc. SPIE* **1080**, 24-31 (1989).

[12] G. W. Smith, "Cure parameters and phase behavior of an ultraviolet-cured polymer-dispersed liquid crystal," *Mol. Cryst. Liq. Cryst.* **196**, 89-102 (1991).

[13] S. Zumer and S. Kralj, "Influence of K_{24} on the structure of nematic liquid crystal droplets," *Liq. Cryst.* **12**, 613-624 (1992).

[14] S. Kralj and S. Zumer, "Freedericksz transitions in supra-μm nematic droplets," *Phys. Rev. A* **45**, 2461-2471 (1192).

[15] R. J. Ondris-Crawford, G. P. Crawford, S. Zumer, and J. W. Doane, "Curvature-induced configuration transition in confined nematic liquid crystals," *Phys. Rev. Lett.* **70**, 194-197 (1993).

[16] P. Drzaic, "A new director alignment for droplets of nematic liquid crystal with low bend-to-splay ratio," *Mol. Cryst. Liq. Cryst.* **154**, 289-306 (1988).

[17] D. Gabor, "A new microscope principle," *Nature* **161**, 777-778 (1948).

[18] D. Gabor, "Microscopy by reconstructed wavefronts," *Proc. Phys. Soc. Am.* **197**, 454-487 (1949).

[19] R. L. Sutherland, L. V. Natarajan, V. P. Tondiglia, and T. J. Bunning, "Bragg gratings in an acrylate polymer consisting of periodic polymer-dispersed liquid-crystal planes" *Chem. Mater.* **5**, 1533-1538 (1993).

[20] L. V. Natarajan, C. K. Shepherd, D. M. Brandelik, R. L. Sutherland, S. Chandra, V. P. Tondiglia, D. Tomlin, and T. J. Bunning, "Switchable holographic polymer-dispersed liquid crystal reflection gratings based on thiol-ene photopolymerization," *Chem. Mater.* **15**, 2477-2484 (2003).

[21] S. -T. Wu, and A. Y. -G. Fuh, "Lasing in photonic crystals based on dye-doped holographic polymer-dispersed liquid crystal reflection gratings," *Jpn. J. Appl. Phys.* **44**, 977-980 (2005).

[22] D. C. Neckers, "Rose Bengal," *J. Photochem. Photobiol. A*, **47**,1-29 (1989)

[23] R. A. Ramsey and S. C. Sharma, "Switchable holographic gratings formed in polymer-dispersed liquid-crytal cells by use of a He-Ne laser," *Opt. Lett.* **30**, 592-594 (2005).

[24] R. A. Ramsey, S. C. Sharma, and K. Vaghela, "Holographically formed Bragg reflection gratings recorded in polymer-dispersed liquid crystal cells using a He-Ne laser," *Appl. Phys. Lett.* **88**, 051121 (2006).

[25] P. Pilot, Y. Boiko, and T. V. Galstyan, "Near IR (800 - 850 nm) sensitive holographic photopolymer dispersed liquid crystal materials," *Proc. SPIE* **3635**, 143-150 (1999).

[26] H. Kogelnik, "Coupled wave theory for thick hologram gratings," *Bell Syst. Tech. J.* **48**, 2909-2947 (1969).

[27] R. L. Sutherland, "Polarization and switching properties of holographic polymer-dispersed liquid-crystal gratings. I. theoretical model," *J. Opt. Soc. Am. B* **19**, 2995-3003 (2002).

[28] A. K. Fontecchio, C. C. Bowley, and G. P. Crawford, "Improvement in holographically formed polymer-dispersed liquid crystal performance through acrylated monomer functionality studies," *Proc. SPIE* **3800**, 36-44 (1999).

[29] Y. J. Liu, B. Zhang, Y. Jia, and K. S. Xu, "Improvement of the diffraction properties in holographic polymer dispersed liquid crystal Bragg gratings," *Opt. Commun.* **218**, 27-32 (2003).

[30] P. Drazaic, "Liquid crystal dispersions," World Scientific, Singapore, 1995.

[31] A. Golemme, S. Zumer, D. W. Allender, and J. W. Doane, "Continuous nematic-isotropic transition in submicron-size liquid-crystal droplets," *Phys. Rev. Lett.* **61**, 2937-2940 (1988).

[32] S. Zumer and J. W. Doane, "Light scattering from a small nematic droplet," *Phys. Rev. A* **34**, 3373-3386 (1986).

[33] R. L. Sutherland, L. V. Natarajan, V. P. Tondiglia, and T. J. Bunning, "The physics of photopolymer-liquid crystal composite holographic gratings," *Proc. SPIE* **2689**, 158-169 (1996).

[34] B. -G. Wu, J. H. Erdmann, and J. W. Doane, "Response times and voltage for PDLC light shutters," *Liq. Cryst.* **5**, 1453-1465 (1989).

[35] Y. J. Liu, X. W. Sun, H. T. Dai, J. H. Liu, and K. S. Xu, "Effect of surfactant on the electro-optical properties of holographic polymer dispersed liquid crystal Bragg gratings," *Opt. Mater.* **27**, 1451-1455 (2005).

[36] C. C. Bowley, P. Kossyrev, S. Danworaphong, J. Colegrove, J. Kelly, T. Fiske, H. Yuan, and G. P. Crawford, "Improving the voltage response of holographically-formed polymer dispersed liquid crytals (H-PDLCs)," *Mol. Cryst. Liq. Cryst.* **359**, 327-339 (2001).

[37] T. J. Bunning, L. V. Natarajan, V. P. Tondiglia, and R. L. Sutherland, "Holographic polymer dispersed liquid crystals (H-PDLCs)," *Annu. Rev. Mater. Sci.* **30**, 83-115 (2000).

[38] J. Klosterman, L. V. Natarajan, V. P. Tondiglia, R. L. Sutherland, T. J. White, C. A. Guymon, and T. J. Bunning, "The influence of surfactant in reflective H-PDLC gratings," *Polymer* **45**, 7213-7218 (2004).

[39] M. De Sarkar, J. Qi, and G. P. Crawford, "Influence of partial matrix fluorination on morphology and performance of H-PDLC transmission gratings," *Polymer* **43**, 7335-7344 (2002).

[40] T. J. Bunning, L. V. Natarajan, V. P. Tondiglia, R. L. Sutherland, D. L. Vezie, W. W. Adams, "The morphology and performance of holographic transmission gratings recorded in polymer dispersed liquid crystals," *Polymer,* **36**, 2699-2708 (1995).

[41] A. K. Fontecchio, G. P. Crawford, C. He, and D. Content, "Performance improvement for switchable H-PDLC gratings using morphological studies," *Proc. SPIE* **4458**, 230-239 (2001).

[42] R. T. Pogue, L. V. Natarajan, V. P. Tondiglia, S. A. Siwecki, R. L. Sutherland, and T. J. Bunning, "Controlling nanaoscale morphology in switchable PDLC gratings," *Proc. SPIE* **3475**, 2-11 (1998).

[43] J. Colegrove, T. Fiske, A. Lewis, H. Yuan, C. Bowley, G. P. Crawford, J. Kelly, and L. Siverstein, "The effect of monomer functionality on H-PDLC performance and aging," *SID Inter. Symp. Dig. Tech. Papers* **32**, 962-965 (2001).

[44] M. De Sarkar, N. L. Gill, J. B. Whitehead, and G. P. Crawford, "Effect of monomer functionality on the morphology and performance of the holographic transmission gratings recorded on polymer dispersed liquid crystals," *Macromolecules* **36**, 630-638 (2003).

[45] R. T. Pogue, L. V. Natarajan, S. A. Siwecki, V. P. Tondiglia, R. L. Sutherland, and T. J. Bunning, "Monomer functionality effects in the anisotropic phase separation of liquid crystals," *Polymer* **41**, 733-741 (2000).

[46] J. Y. Woo, M. S. Park, B. K. Kim, J. C. Kim, and Y. S. Kang, "Reflective holographic polymer-dispersed liquid crystal films based on polyurethane acrylate," *J. Macromolecular Sci. Part B-Phys.* **B43**, 833-843 (2004).

[47] Y. H. Cho, B. K. Kim, and K. S. Park, "Optimization of holographic polymer dispersed liquid crystal for ternary monomers," *Polym. Int.* **48**, 1085-1090 (1999).

[48] M. S. Park, Y. H. Cho, B. K. Kim, and J. S. Jang, "Fabrication of reflective holographic gratings with polyurethane acrylate (PUA)," *Curr. Appl. Phys.* **2**, 249-252 (2002).

[49] M. S. Park, B. K. Kim, and J. C. Kim, "Reflective mode of H-PDLC with various structures of polyurethane acrylates," *Polymer* **44**, 1595-1602 (2003).

[50] Y. H. Cho, M. He, B. K. Kim, and Y. Kawakami, "Improvement of holographic performance by novel photopolymer systems with siloxane-containing epoxides," *Sci. & Techno. Advan. Mater.* **5**, 319-323 (2004).

[51] K. Tanaka, K. Kato, S. Tsuru, and S. Sakai, "Holographically formed liquid-crystal/polymer devices for reflective color display," *J. SID* **2**, 37-40 (1994).

[52] K. Tanaka, K. Kato, M. Date, and S. Sakai, "Optimization of holographic PDLC for reflective color display applications," *SID Inter. Symp. Dig. Tech. Papers* **26**, 267-270 (1995).

[53] M. Date, Y. Takeuchi, and K. Kato, "A memory-type holographic polymer dispersed liquid crystal (HPDLC) reflective display device," *J. Phys. D: Appl. Phys.* **31**, 2225-2230 (1998).

[54] M. Date, Y. Takeuchi, K. Tanaka, and K. Kato, "Full-color reflective display device using holographically fabricated polymer-dispersed liquid-crystal (H-PDLC)," *J. SID* **7**, 17-22 (1999).

[55] H. Yuan, J. Colegrove, G. Hu, T. Fiske, A. Lewis, J.Gunther, L. Silverstein, C. Bowley, G. Crawford, L. Chien, and J. Kelly, "H-PDLC color reflective displays," *Proc. SPIE* **3690**, 196-206 (1999).

[56] G. P. Crawford, T. G. Fiske, and L. D. Silverstein, "Reflective color LCDs based on H-PDLC and PSCT technologies," *SID Inter. Symp. Dig. Tech. Papers* **27**, 99-103 (1996).

[57] G. P. Crawford, "A bright new page in portable displays," *IEEE Spectrum* **37**, 40-46 (2000).

[58] R. L. Sutherland, L. V. Natarajan, V. P. Tondiglia, and T. J. Bunning, "Switchable holograms for displays and other applications," *Proc. SPIE* **3421**, 8-18 (1998).

[59] M. J. Escuti, P. Kossyrev, G. P. Crawford, T. G. Fiske, J. Colegrove, and L. D. Silverstein, "Expanded viewing-angle reflection from diffuse holographic-polymer dispersed liquid crystal films," *Appl. Phys. Lett.* **77**, 4262-4264 (2000).

[60] V. P. Tondiglia, L. V. Natarajan, R. L. Sutherland, T. J. Bunning, W. W. Adams, "Volume holographic image storage and electro-optical readout in a polymer-dispersed liquid-crystal film," *Opt. Lett.* **20**, 1325-1327 (1995)

[61] P. Pilot, Y. B. Boiko, T. V. Galstian, "Polarization-dependent broadening of angular selectivity of holograms recorded on near-IR sensitive PDLC," *Proc. SPIE* **3638**, 26-34 (1999).

[62] A. Tork, P. Pilot, T. V. Galstian, "New photopolymer materials for holographic data storage," Optical Data Storage 2000, Conference Digest, 138-140 (2000).

[63] M. Stalder and P. Ehbets, "Electrically switchable diffractive optical element for image processing," *Opt. Lett.* **19**, 1-3 (1994).

[64] P. B. Brinkley and S. T. Kowel, "Liquid crystal adaptive lens: operation and aberration," *Proc. SPIE* **1773**, 449-458 (1992).

[65] S. Hunter and S. C. Esener, "Dynamic focusing lens for volume optical memory applications," *Proc. SPIE* **1773**, 459-467 (1992).

[66] L. H. Domash, C. M. Gozewski, A. R. Nelson, J. R. Schwartz, "Programmable beambelt generator, dynamic lens, and optical memory using electrically switched holographic devices," *Proc. SPIE* **2026**, 642-652 (1993).

[67] B. Parker, "Switchable optical elements merge optics and electronics," *Laser focus world* **35**, 135-138 (1999).

[68] L. H. Domash, Y. -M. Chen, B. N. Gomatam, C. M. Gozewski, R. L. Sutherland, L. V. Natarajan, V. P. Tondiglia, T. J. Bunning, and W. W. Adams, "Switchable-focus lenses in holographic polymer-dispersed liquid crystal," *Proc. SPIE* **2689**, 188-194 (1996).

[69] L. Domash, G. Crawford, A. Ashmead, R. Smith, M. Popovich, J. Storey, "Holographic PDLC for photonic applications," *Proc. SPIE* **4107**, 46-58 (2000).

[70] A. Ashmead, "Electronically switchable Bragg gratings provide versatility," *Lightwave* **18**, 180-184 (2001).

[71] C. Gu, Y. Xu, Y. S. Liu, J. J. Pan, F. Q. Zhou, and H. He, "Applications of photorefractive materials in information storage, processing and communication," *Opt. Mater.* **23**, 219-227 (2003).

[72] R. Jakubiak, T. J. Bunning, R. A. Vaia, L. V. Natarajan, and V. P. Tondiglia, "Electrically switchable, one-dimensional polymeric resonators from holographic photopolymerization: a new approach for active photonic bandgap materials," *Adv. Mater.* **15**, 241-244 (2003).

[73] D. E. Lucchetta, L. Criante, O. Francescangeli, and F. Simoni, "Wavelength flipping in laser emission driven by a switchable holographic grating," *Appl. Phys. Lett.* **84**, 837-839 (2004).

[74] D. E. Lucchetta, L. Criante, O. Francescangeli, and F. Simoni, "Light amplification by dye-doped holographic polymer dispersed liquid crystals," *Appl. Phys. Lett.* **84**, 4893-4895 (2004).

[75] D. E. Lucchetta, L. Criante, O. Francescangeli, and F. Simoni, "Compact lasers based on HPDLC gratings," *Mol. Cryst. Liq. Cryst.* **441**, 97-109 (2005).

[76] S. J. Woltman, M. E. Sousa, H. L. Zhang, and G. P. Crawford, "Survey of switchable lasing configurations using structures of liquid crystal and polymer dispersions," *Proc. SPIE* **6135**, 61350B (2006).

[77] R. Jakubiak, L. V. Natarajan, V. Tondiglia, G. S. He, P. N. Prasad, T. J. Bunning, and R. A. Vaia, "Electrically switchable lasing from pyrromethene 597 embedded holographic-polymer dispersed liquid crystals," *Appl. Phys. Lett.* **85**, 6095-6097 (2004).

[78] G. S. He, T.-C. Lin, V. K. S. Hsiao, A. N. Cartwright, P. N. Prasad, L. V. Natarajan, V. P. Tondiglia, R. Jakubiak, R. A. Vaia, and T. J. Bunning, "Tunable two-photon pumped lasing using a holographic polymer-dispersed liquid-crystal grating as a distributed feedback element," *Appl. Phys. Lett.* **83**, 2733-2735 (2003).

[79] V. K. S. Hsiao, C. G. Lu, G. S. He, M. Pan, A. N. Cartwright, P. N. Prasad, R. Jakubiak, R. A. Vaia, and T. J. Bunning, "High contrast switching of distributed-feedback lasing in dye-doped H-PDLC transmission grating structures," *Opt. Express* **13**, 3787-3794 (2005).

[80] V. P. Tondiglia, L. V. Natarajan, R. L. Sutherland, D. Tomlin, and T. J. Bunning, "Holographic formation of electro-optical polymer-liquid crystal photonic crystals," *Adv. Mater.* **14**, 187-191 (2002).

[81] R. L. Sutherland, V. P. Tondiglia, L. V. Natarajan, and S. Chandra, "Switchable orthorhombic F photonic crystals formed by holographic polymerization-induced phase separation of liquid crystal," *Opt. Express* **10**, 1074-1082 (2002).

[82] M. J. Escuti, J. Qi, and G. P. Crawford, "Tunable face-centered-cubic photonic crystal formed in holographic polymer dispersed liquid crystals," *Opt. Lett.* **28**, 522-524 (2003).

[83] M. J. Escuti, J. Qi, and G. P. Crawford, "Two-dimensional tunable photonic crystal formed in a liquid-crystal/polymer composite: threshold behavior and morphology," *Appl. Phys. Lett.* **83**, 1331–1333 (2003).

[84] M. J. Escuti, and G. P. Crawford, "Mesoscale three dimensional lattices formed in polymer dispersed liquid crystals: a diamond-like face centered cubic," *Mol. Cryst. Liq. Cryst.* **421**, 23–36 (2004).

[85] S. P. Gorkhali, J. Qi, and G. P. Crawford, "Electrically switchable mesoscale Penrose quasicrystal structure," *Appl. Phys. Lett.* **86**, 011110 (2005).

[86] M. J. Escuti and G. P. Crawford, "Holographic photonic crystals," *Opt. Eng.* **43**, 1973-1987 (2004).

[87] J. Qi and G. P. Crawford, "Holographically formed polymer dispersed liquid crystal displays," *Displays* **25**, 177-186 (2004).

[88] S. P. Gorkhali, J. Qi, and G. P. Crawford, "Switchable quasi-crystal structures with five-, seven-, and ninefold symmetries," *J. Opt. Soc. Am. B* **23**, 149-158 (2006).

[89] R. Jakubiak, V. P. Tondiglia, L. V. Natarajan, R. L. Sutherland, P. Lloyd, T. J. Bunning, and R. A. Vaia, "Dynamic lasing from all-organic two-dimensional photonic crystals," *Adv. Mater.* **17**, 2807-2811 (2005).

[90] M. L. Ermold, K. Rai, and A. K. Fontecchio, "Hydrostatic pressure response of polymer-dispersed liquid crystal gratings," *J. Appl. Phys.* **97**, 104905 (2005).

[91] K. Rai and A. K. Fontecchio, "Optimization of pressure response in HPDLC gratings based on polymer composition," *Mol. Cryst. Liq. Cryst.* **450**, 183-190 (2006).

[92] V. K. S. Hsiao, W. D. Kirkey, F. Chen, A. N. Cartwright, P. N. Prasad, and T. J. Bunning, "Organic solvent vapor detection using holographic photopolymer reflection gratings," *Adv. Mater.* **17**, 2211-2214 (2005).

[93] J. Colegrove, H. Yuan, S. T. Wu, J. R. Kelly, C. C. Bowley, and G. P. Crawford, "Drive-voltage reduction for HPDLC displays," *SID Inter. Symp. Dig. Tech. Papers-International Display Workshop* **99**, 105-108 (1999).

[94] M. D. Schulte, S. J. Clarson, L. V. Natarajan, C. A. Guymon, and T. J. Bunning, "Holographic polymer dispersed liquid crystals: effect of partial matrix fluorination on electro-optical and morphological properties," *Mat. Res. Soc. Symp. Proc.* **709**, CC6.7 (2002).

[95] H. Yuan, G. Hu, T. Fiske, A. Lewis, J. E. Gunther, L. D. Silverstein, C. C. Bowley, G. P. Crawford, L. -C. Chien, and J. R. Kelly, "High efficiency color reflective displays with extended viewing angle," *Proceedings of the 18th International Display Research Conference*, 1135-1138 (1998).

[96] S. S. Patnaik and R. Pachter, "Anchoring characteristics and interfacial interactions in a polymer dispersed liquid crystal: a molecular dynamics study," *Polymer* **40**, 6507-6519 (1999).

97 G. P. Crawford, R. J. Ondris-Crawford, and J. W. Doane, "Systematic study of orientational wetting and anchoring at a liquid-crystal-surfactant interface," *Phys. Rev. E* **53**, 3647-3661 (1996).

98 M. L. Ermold and A. K. Fontecchio, "Viewing-angle enhancement in holographic reflective displays by nanoscale holographic patterning," *J. SID* **13**, 787-792 (2005).

99 K. Studer, C. Decker, E. Beck, and R. Schwalm, "Overcoming oxygen inhibition in UV-curing of acrylate coatings by carbon dioxide inerting, Part I," *Progress in Organic Coatings* **48**, 92-100 (2003).

100 K. Studer, C. Decker, E. Beck, and R. Schwalm, "Overcoming oxygen inhibition in UV-curing of acrylate coatings by carbon dioxide inerting, Part II," *Progress in Organic Coatings* **48**, 101-111 (2003).

101 C. C. Bowley and G. P. Crawford, "Diffusion kinetics of formation of holographic polymer-dispersed liquid crystal display materials," *Appl. Phys. Lett.* **76**, 2235-2237 (2000).

102 J. Qi, L. L. Li, M. De Sarkar, and G. P. Crawford, "Nonlocal photopolymerization effect in the formation of reflective holographic polymer-dispersed liquid crystals," *J. Appl. Phys.* **96**, 2443-2450 (2004).

103 T. Kyu, D. Nwabunma, and H.-W. Chiu, "Theoretical simulation of holographic polymer-dispersed liquid-crystal films via pattern photopolymerization-induced phase separation," *Phys. Rev. E* **63**, 061802 (2001).

104 R. L. Sutherland, L. V. Natarajan, T. J. Bunning, and V. P. Tondiglia, "Handbook of advanced electronic and photonic materials and devices," ed. H. S. Nalwa, Vol. 7, Chap. 2, Academic Press, San Diego, 2001.

105 M. S. Park and B. K. Kim, "Transmission holographic gratings produced using networked polyurethane acrylates with various functionalities," *Nanotechnology* **17**, 2012-2017 (2006).

106 T. J. Bunning, L. V. Natarajan, V. P. Tondiglia, G. Dougherty, R. L. Sutherland, "Morphology of anisotropic polymer-dispersed liquid crystals and the effect of monomer functionality," *J. Poly. Sci.: Part B-Poly. Phys.* **35**, 2825-2833 (1997).

107 T. J. White, W. B. Liechty, L. V. Natarajan, V. P. Tondiglia, T. J. Bunning, and C. A. Guymon, "The influence of N-vinyl-2-pyrrolidinone in polymerization of holographic polymer dispersed liquid crystals (HPDLCs)," *Polymer* **47**, 2289-2298 (2006).

[108] B. K. Kim, Y. C. Jeon, C. O. Yoon, K. J. Kim, and Y. H. Cho, "Optimization of holographic PDLC for green," *Mol. Cryst. Liq. Cryst.* **368**, 87-96 (2001).

[109] N. J. Crawford, M. D. Dadmun, T. J. Bunning, and L. V. Nararajan, "Time-resolved light scattering of the phase separation in polymer-dispersed liquid crystal formed by photo-polymerization induced phase separation," *Polymer* **47**, 6311-6321 (2006).

[110] R. Ulrich and R. Torge, "Measurement of thin film parameters with a prism coupler," *Appl. Opt.* **12**, 2901-2908 (1973).

[111] P. Mormile, P. Musto, L. Petti, G. Ragosta, and P. Villano, "Eletro-optical properties of a PDLC based on unsaturated polyester resin," *Appl. Phys. B* **70**, 249-252 (2000).

[112] X. J. Wang, L. Xu, D. X. Li, L. Y. Liu, and W. C. Wang, "Thermo-optic properties of sol-gel-fabricated organic-inorganic hybrid waveguides," *J. Appl. Phys.* **94,** 4228-4230 (2003).

[113] C. Z. van Doorn, "Dynamic behavior of twisted nematic liquid-crystal layers in switched fields," *J. Appl. Phys.* **46,** 3738-3745 (1975).

[114] D. W. Berreman, "Liquid-crystal twist cell dynamics with backflow," *J. Appl. Phys.* **46,** 3746-3751 (1975).

[115] G. T. Warren, M. Desarkar, J. Qi, and G. P. Crawford, "In-Situ Spectroscopy of Holographically formed Polymer Dispersed Liquid Crystal Materials for High Performance Reflective Display Applications," *SID Inter. Symp. Dig. Tech. Papers* **32**, 866-869 (2001).

[116] T. Karasawa and Y. Taketomi, "Effects of material systems on the polarization behavior of holographic polymer dispersed liquid crystal gratings," *Jpn. J. Appl. Phys.* **36**, 6388-6392 (1997).

[117] C. -M. Chang and H. -P. D. Shieh, "Design of illumination and projection optics for projectors with single digital micromirror devices," *Appl. Opt.* **39**, 3202-3208 (2000).

[118] B. G. Crowther, D. G. Koch, J. M. Kunick, J. P. McGuire, R. Harned, and R. Gotin, "A fly's eye condenser system for uniform illumination," *Proc. SPIE* **4832**, 302-310 (2002).

[119] A. H. J. van den Brandt and W. A. G. Timmers, US Patent 5, 098,184 (1990).

[120] Y. Masumoto, US Patent 5, 418, 583 (1993).

[121] H. Shimonura, Y. Manabe, T. Hattori, M. Kusano, and A. Sekine, US Patent 5, 959, 778 (1997).

[122] M. Foley and J. Munro, "Polymer fly's eye light integrator lens arrays for digital projectors," *SID Inter. Symp. Dig. Tech. Papers* **31**, 870-873 (2000).

[123] M. Foley, "Technical advances in microstructured plastic optics for display applications," *SID Inter. Symp. Dig. Tech. Papers* **30**, 1106-1109 (1999).

[124] Y. J. Liu, X. W. Sun, J. H. Liu, H. T. Dai, and K. S. Xu, "A polarization insensitive 2×2 optical switch fabricated by liquid crystal-polymer composite," *Appl. Phys. Lett.* **86**, 041115 (2005).

[125] R. L. Sutherland, L. V. Natarajan, V. P. Tondiglia, S. A. Siwecki, S. Chandra, and T. J. Bunning, "Switchable holograms for displays and telecommunications," *Proc. SPIE* **4463**, 1-10 (2001).

[126] C. C. Bowley, A. K. Fontecchio, G. P. Crawford, J.-J. Lin, L. Li, and S. Faris, "Multiple gratings simultaneously formed in holographic polymer-dispersed liquid-crystal displays," *Appl. Phys. Lett.* **76**, 523-525 (2000).

[127] J. R. Dorgan and D. Yan, "Kinetics of spinodal decomposition in liquid crystalline polymers: processing effects on the phase separation morphology," *Macromolecules* **31**, 193-200 (1998).

[128] D. Nwabunma and T. Kyu, "Phase behavior of mixtures of low molar mass nematic liquid crystal and in situ photo-cross-linked polymer network," *Macromolecules* **32**, 664-674 (1999).

[129] D. Nwabunma, H.-W. Chiu, and T. Kyu, "Theoretical investigation on dynamics of photopolymerization-induced phase separation and morphology development in nematic liquid crystal/polymer mixtures," *J. Chem. Phys.* **113**, 6429-6436 (2000).

[130] T. Kyu and D. Nwabunma, "Simulations of microlens arrays formed by pattern-photoplymerization-induced phase separation of liquid crystal/monomer mixtures," *Macromolecules* **34**, 9168-9172 (2001).

[131] A. J. MacGovern and J. C. Wyant, "Computer generated holograms for testing optical element," *Appl. Opt.* **10**, 619-624 (1971).

[132] A. W. Lohman and D. P. Paris, "Binary Fraunhofer holograms generated by computer," *Appl. Opt.* **6**, 1739-1748 (1967).

[133] O. Bryngdahl, "Optical map transformations," *Opt. Commun.* **10**, 164-168 (1974).

[134] D. Casasent and C. Szczutkowski, "Optical Mellin transforms using computer generated holograms," *Opt. Commun.* **19**, 217-222 (1976).

[135] J. Cederquist and A. Tai, "Computer generated holograms for geometric transformations," *Appl. Opt.* **23**, 3099-3104 (1984).

[136] D. Casasent, "Computer generated holograms in pattern recognition: a review," *Opt. Eng.* **24**, 724-730 (1985).

[137] K. Nakagawa, S. Iguchi, and T. Minemoto, "Computer-generated holograms in photorefractive LiNbO$_3$ crystal," *Proc. SPIE* **3470**, 77-83 (1998).

[138] L. Pugliese and G. M. Morris, "Computer-generated holography in photorefractive materials," *Opt. Lett.* **15**, 338-340 (1990).

[139] F. Guessous, T. Juchem, and N. Hampp, "Computer generated holograms recorded in bacteriorhodopsin," *Proc. SPIE* **5310**, 369-376 (2004).

[140] F. Mok, J. Diep, H. -K. Liu, and D. Psaltis, "Real-time computer-generated hologram by means of liquid-crystal television spatial light modulator," *Opt. Lett.* **11**, 748-750 (1986).

[141] V. Arrizon, L. A. Gonzalez, R. Ponce, and A. Serrano-Heredia, "Computer-generated holograms with optimum bandwidths obtained with twisted-nematic liquid-crystal displays," *Appl. Opt.* **44**, 1625-1634 (2005).

[142] Y. J. Liu, X. W. Sun, P. Shum, H. P. Li, J. Mi, W. Ji, and X. H. Zhang, "low-threshold and narrow-linewidth lasing from dye-doped holographic polymer-dispersed liquid crystal transmission gratings," *Appl. Phys. Lett.* **88**, 061107 (2006).

[143] A. Emoto, H. Ono, and N. Kawatsuki, "Spatial frequency selective reconstruction using Fourier transform holograms generated in functionalized mesogenic composites," *Liq. Cryst.* **30**, 1201-1206 (2003)

[144] A. Y. -G. Fuh, M. -S. Tsai, C. -Y. Huang, T. -C. Ko, and L. -C. Chien, "Polymer-dispersed liquid crystal films for storing optical holographic images," *Opt. Quant. Electron.* **28**, 1535-1541 (1996).

[145] R. W. Gerchber and W. O. Saxton, "A Practical algorithm for the determination of phase from image and diffraction plance pictures," *Optik* **35**, 237-246 (1972).

[146] H. Car, Y. G. Zhao, S. T. Ho, E. W. Seelig, Q. H. Wang, and R. P. H. Chang, "Random laser action in semiconductor power," *Phys. Rev. Lett.* **82**, 2278-2281 (1999).

[147] D. S. Wiersma and S. Cavalieri, "Light emission: A temperature-tunable random laser," *Nature* **414**, 708-709 (2001).

[148] Q. H. Song, L. Wang, S. M. Xiao, X. C. Zhou, L. Y. Liu, and L. Xu, "Random laser emission from a surface-corrugated waveguide," *Phys. Rev. B* **72**, 035424 (2005).

[149] H. Cao, J. Y. Xu, S. -H. Chang, and S. T. Ho, "Transition from amplified spontaneous emission to laser action in strongly scattering media," *Phys. Rev. E* **61**, 1985-1989 (2000).

[150] E. S. P. Leong, M. K. Chong, and S. F. Yu, "Sol-gel ZnO-SiO$_2$ composite waveguide ultraviolet lasers," *IEEE Photon. Technol. Lett.* **16**, 2418-2420 (2004).

[151] S. Gottardo, S. Cavalieri, O. Yaroshchuk, and D. S. Wiersma, "Quasi-two-dimensional diffusive random laser action," *Phys. Rev. Lett.* **93**, 263901 (2004).

[152] H. Harada, M. Nakatsu, and H. Naito, "Emission gain narrowing in dye-doped polymer dispersed liquid crystals," *Jpn. J. Appl. Phys.* **44**, L915-L917 (2005).

[153] B. E. A. Saleh and M. C. Teich, "Fundamentals of photonics," Chapter 7, (Wiley, New York, 1991).

[154] J. Qi, M. De Sarkar, G. T. Warren, and G. P. Crawford, "In situ shrinkage measurement of holographic polymer dispersed liquid crystals," *J. Appl. Phys.* **91**, 4795-4800 (2002).

[155] H. Kogelnik, T. P. Sosnowski, and H. P. Webber, "A ray-optical analysis of thin-film polarization converters," *IEEE J. Quantum Electron.* **9**, 795-800 (1973).

[156] L. S. Goldberg and J. M. Schnur, U. S. Patent 3, 771, 065 (1973).

[157] V. I. Kopp, B. Fan, H. K. M. Vithana, and A. Z. Genack, "Low-theshold lasing at the edge of a photonic stop band in cholesteric liquid crystals," *Opt. Lett.* **23**, 1707-1709 (1998).

[158] A. Chanishvili, G. Chilaya, G. Petriashvili, R. Barberi, R. Bartolino, G. Cipparrone, A. Mazzulla, and L. Oriol, "Lasing in dye-doped cholesteric liquid crystals: two new tuning strategies," *Adv. Mater.* **16**, 791-795 (2004).

[159] T. -H. Lin, Y. -J. Chen, C. -H. Wu, A. Y. -G. Fuh, J. -H. Liu, and P. -C. Yang, "Cholesteric liquid crystal laser with wide tuning capability," *Appl. Phys. Lett.* **86**, 161120 (2005).

[160] Y. H. Huang, Y. Zhou, and S. -T. Wu, "Spatially tunable laser emission in dye-doped photonic liquid crystals," *Appl. Phys. Lett.* **88**, 011107 (2006).

[161] Y. Zhou, Y. H. Huang, Z. B. Ge, L. –P. Chen, Q. Hong, T. X. Wu, and S. –T. Wu, "Enhanced photonic band edge laser emission in a cholesteric liquid crystal resonator," *Phys. Rev. E* **74**, 061705 (2006).

[162] S. Shibata, A. Araya, T. Yano, and M. Yamane, "Photostability of the laser emission from dye-doped spherical particles," *Proc. SPIE* **4804**, 44-51 (2002).

[163] G. Strangi, V. Barna, R. Caputo, A. D. Luca, C. Versace, N. Scaramuzza, C. Umeton, R. Bartolino, and G. N. Price, "Color-tunable organic microcavity laser array using distributed feedback," *Phys. Rev. Lett.* **94**, 063903 (2005).

[164] J. P. Dowling, M. Scalora, M. J. Bloemer, and C. M. Bowden, "The photonic band edge laser: a new approach to gain enhancement," *J. Appl. Phys.* **75**, 1896-1899 (1994).

[165] T. Ling, L. Y. Liu, Q. H. Song, L. Xu, and W. C. Wang, "Intense directional lasing from a deformed square-shaped organic-inorganic hybrid glass microring cavity," *Opt. Lett.* **28**, 1784-1786 (2003).

[166] B. Maune, M. Loncar, J. Witzens, M. Hochberg, T. Baehr-Jones, D. Psaltis, A. Scherer and Y. M. Qiu, "Liquid-crystal electric tuning of a photonic crystal laser," *Appl. Phys. Lett.* **85**, 360-362 (2004).

[167] S. -T. Wu, "Birefringence dispersions of liquid crystals," *Phys. Rev. A* **33**, 1270-1274 (1986).

[168] N. G. Sultanova, S. N. Kasarova, C. D. Ivanov, and I. D. Nikolov, "Refractive data of optical plastics for laser applications," *Proc. SPIE* **6252**, 62520H (2006).

[169] J. D. Joannopoulos, R. D. Meade, and J. N. Winn, "Photonic crystals - molding the flow of light," Princeton University Press, Princeton, 1995.

[170] A. Figotin, Y. A. Godin, and I. Vitebsky, "Two-dimensional tunable photonic crystals," *Phys. Rev. B* **57**, 2841-2848 (1998).

[171] K. Busch and S. John, "Liquid-crystal photonic-band-gap materials: The tunable electromagnetic vacuum," *Phys. Rev. Lett.* **83**, 967-970 (1999).

[172] E. Yablonovitch, "Inhibited spontaneous emission in solid state physics and electronics," *Phys. Rev. Lett.* **58**, 2059-2062 (1987).

[173] S. John, "Strong localization of photons in certain disordered dielectric superlattices," *Phys. Rev. Lett.* **58**, 2486-2489 (1987).

[174] Y. -J. Lee, S. -H. Kim, J. Huh, G. -H. Kim, Y. -H. Lee, S. -H. Cho, Y. -C. Kim, and Y. R. Do, "A high-extraction-efficiency nanopatterned organic light-emitting diode," *Appl. Phys. Lett.* **82**, 3779-3781 (2003).

[175] S. -Y. Lin, E. Chow, V. Hietala, P. R. Villeneuve, and J. D. Joannopoulos, "Experimental demonstration of guiding and bending of electromagnetic waves in a photonic crystal," *Science* **282**, 274-276 (1998).

[176] B. -K. Min, J. -E. Kim, and H. Y. Park, "High-efficiency surface-emitting channel drop filters in two-dimensional photonic crystal slabs," *Appl. Phys. Lett.* **86**, 011106 (2005).

[177] M. D. B. Charlton, S. W. Roberts, and G. J. Parker, "Guided mode analysis and fabrication of a 2-dimensional visible photonic band structure confined within a planar semiconductor waveguide," *Mater. Sci. Eng. B* **49**, 155-165 (1997).

[178] A. Y. Vlasov, X. Bo, and C. J. Sturm, "On-chip natural assembly of silicon photonic bandgap crystals," *Nature* **6861**, 289-293 (2001).

[179] E. Özbay, E. Michel, and G. Tuttle, "Micromachined millimeter-wave photonic band-gap crystals," *Appl. Phys. Lett.* **64**, 2059-2061 (1994).

[180] M. Campbell, N. D. Sharp, and T. M. Harrison, "Fabrication of photonic crystals for the visible spectrum by holography," *Nature* **6773**, 53-56 (2000).

[181] V. Y. Miklyaev, C. D. Meisel, and A. Blanco, "Three dimensional face-centered-cubic photonic crystal templates by laser holography: fabrication, optical characterization, and band-structure calculations," *Appl. Phys. Lett.* **82**, 1284-1286 (2003).

[182] D. N. Sharp, M. Campbell, and R. E. Dedman, "Photonic crystals for the visible spectrum by holographic lithography," *Opt. Quant. Electron.* **34**, 3-12 (2002).

[183] L. Z. Cai, X. L. Yang, and Y. R. Wang, "Formation of three-dimensional periodic microstructures by interference of four noncoplanar beams," *J. Opt. Soc. Am. A* **19**, 2238-2244 (2002).

[184] I. Divliansky, T. S. Mayer, K. S. Holliday, and V. H. Crespi, "Fabrication of three-dimensional polymer photonic crystal structures using single diffraction element interference lithography," *Appl. Phys. Lett.* **82**, 1667-1669 (2003).

[185] V. Berger, O. Gauthier-Lafaye, and E. Costard, "Fabrication of a 2D photonic bandgap by a holographic method," *Electron. Lett.* **33**, 425-426 (1997).

[186] A three-index system of (a b $\bar{c}$) was used to represent the 2-D hexagonal lattice, where $c = - (a + b)$.

[187] L. L. Brott, R. R. Naik, D. J. Pikas, S. M. Kirkpatrick, D. W. Tomlin, P. W. Whitlock, S. J. Clarson, and M. O. Stone, "Ultrafast holographic nanopatterning of biocatalytically formed silica," *Nature* **413**, 291-293 (2001).

[188] Y. Tomita, N. Suzuki, and K. Chikama, "Holographic manipulation of nanoparticle distribution morphology in nanoparticle-dispersed photopolymers," *Opt. Lett.* **30**, 839-841 (2005).

[189] Y. Tomita, K. Chikama, Y. Nohara, N. Suzuki, K. Furushima, and Y. Endoh, "Two-dimensional imaging of atomic distribution morphology created by holographically induced mass transfer of monomer molecules and nanoparticles in a silica-nanoparticle-dispersed photopolymer film," *Opt. Lett.* **31**, 1402-1404 (2006).

[190] N. Suzuki, Y. Tomita, K. Ohmori, M. Hidaka, and K. Chikama, "Highly transparent ZrO_2 nanoparticle-dispersed acrylate photopolymers for volume holographic recording," *Opt. Express* **14**, 12712-12719 (2006).

[191] W. S. Kim, Y. -C. Jeong, and J. -K. Park, "Nanoparticle-induced refractive index modulation of organic-inorganic hybrid photopolymer," *Opt. Express* **14**, 8967-8973 (2006).

[192] J. Y. Huang, X. D. Wang, and Z. L. Wang, "Controlled replication of butterfly wings for achieving tunable photonic properties," *Nano Lett.* **6**, 2325-2331 (2006).